UNIVERSITY OF CALIFORNIA
SANTA CRUZ

ACOUSTIC AND ELASTIC REVERSE-TIME MIGRATION: NOVEL ANGLE-DOMAIN IMAGING CONDITIONS AND APPLICATIONS

A dissertation submitted in partial satisfaction
of the requirements for the degree of

DOCTOR OF PHILOSOPHY

in

EARTH SCIENCES (GEOPHYSICS)

by

Rui Yan

June 2013

The Dissertation of Rui Yan is approved:

Dr. Ru-Shan Wu (Chair), UCSC

Professor Thorne Lay, UCSC

Dr. Xiao-Bi Xie, UCSC

Professor Susan Schwartz, UCSC

Dr. Lianjie Huang, Los Alamos National Lab

Tyrus Miller
Vice Provost and Dean of Graduate Studies

Table of Contents

ABSTRACT

ACOUSTIC AND ELASTIC REVERSE-TIME MIGRATION: NOVEL ANGLE-DOMAIN IMAGING CONDITIONS AND APPLICATIONS

Rui Yan

Reverse-time migration (RTM) has become a superior choice in seismic imaging due to its capability of handling of rapid spatial velocity variation and imaging without dip angle limitations. By adopting the full-wave propagator, RTM is very accurate to reconstruct the source and receiver wavefields. As the conventional zero-lag cross-correlation imaging condition is applied to the reconstructed wavefields, we can achieve the primary goal of the seismic imaging, which is, to produce a geometrical image of the subsurface structures. However, for further exploration of the subsurface information carried by the reconstructed wavefields, more sophisticated imaging conditions are demanded. For example, to remove RTM low-wavenumber artifacts, we need to incorporate the angle information in the imaging condition. To deal with multicomponent elastic data, we need to separate the wavefields into P- and S- modes before applying the imaging condition. To provide information for migration velocity updating, we need to expand the stacked image into various types of common image gathers, such as in angle, offset, shot, etc. To retrieve the properties of the interfaces, we need to recover amplitude versus angle (AVA) and account for the propagation and acquisition effects in the imaging condition.

Many of those advanced imaging conditions require working in the local angle domain. However, unlike in the ray-based methods, the angle information is not

explicitly given in RTM. In this thesis, great efforts are expended to extract the angle information from the migrated wavefields. The local slant stacking is employed to decompose the full acoustic and elastic wavefields into a superposition of localized plane waves and separate the vectorized waves into P- and S-waves. It serves as the fundamental technique in the following part of the thesis to develop angle-domain imaging condition.

In the included chapters, first, we construct local image matrix (LIM) by cross-correlating the decomposed plane-wave components from the source wavefield and those from the receiver wavefield. With the introduction of the angle-domain operators to local image matrix, we remove the strong artifacts existed in PP image and correct the polarization problem in PS image. Second, we generate gathers of various sorts from LIM, such as the common reflection-angle gather (generally called angle-domain common image gather) and common dip-angle gather. The angle-domain common image gather is a powerful tool for migration velocity analysis. Third, we derive the theory of true-amplitude imaging in local angle domain. We calculate the target illumination matrix with the plane wave components of background Green's function under the survey configuration and use it to correct LIM. Similarly, we output dip-angle-dependent illumination (generally called acquisition dip response) and reflection-angle-dependent illumination from target illumination matrix. Fourth, we retrieve the AVA responses by normalizing angle-domain common image gathers with the reflection-angle-dependent illuminations, and cross-

plot them to detect the reservoir characterization. Fifth, we compensate the common dip-angle gathers with acquisition dip responses and sum them up to form a true-amplitude image. Due to the tremendous computations involved in the true-amplitude problems, we develop efficient algorithms to make these calculations practical and affordable. Numerical examples demonstrate the applications of angle-domain imaging conditions to angle gather extraction, AVA analysis and true-amplitude imaging.

ACKNOWLEDGEMENTS

First and foremost, I would like to express my sincere gratitude towards my advisor Ru-Shan Wu for his vision, inspiration and the guidance throughout my thesis work. His insightful and broad knowledge of the geophysical fields enlightened me enormously. His attitude towards his work set a good example for me to follow during my PhD life and in the future.

At the same time, it is hard to overstate my gratitude to Dr. Xiao-Bi Xie, who is one of the best mentors and teachers. Without his guidance, it would take me much longer to know how to approach the solution in a scientific way. I benefit a lot from the numerous inspiring discussions with him. His physical intuition and critical thinking always give me directions in the research.

Other committee members Thorne Lay, Susan Schwartz, Lianjie Huang are acknowledged for their valuable comments and suggestions on my research projects and thesis.

I would like to thank Chuck Mosher (@ConocoPhillips) and Huimin Guan (@TOTAL) for providing me the opportunities to intern in the oil companies. I learned AVA analysis from the experts at ConocoPhillips. Huimin shared with me her insights on the angle decomposition and 3D acquisition.

In my daily work I have been blessed with an excellent and friendly group of fellow students. Yingcai Zheng and Zengxi Ge are the few persons who will first come to mind when I was confused by a problem and really need someone to talk with. I learn most of the computational skills, such as LINUX, SHELL script and MPI, from Hui Yang, Yaofeng He, Jian Mao, Yu Geng and Jingrui Luo. I do not have a car when I first came to Santa Cruz and when I interned in Conocophillips, and Jun Cao generously offer me lots of free rides. I cannot forget the time I spent with all the group members after work and their friendship bring a lot of fun to my life at Santa Cruz.

The thesis is made possible through continuous financial support from WTOPI consortium and facility support from modeling and imaging laboratory. The administrative staff in the Earth Sciences department has been so helpful, making my life in Santa Cruz smooth and easy.

I would like to thank Bangyu's companion. He witnessed me go through many difficulties and became my strong backing in the past five years.

In the end, I want to thank my mom who always supports me for no reason. All the good things that have happened to me are attributed to her.

1 THESIS INTRODUCTION

In the past few decades, migration algorithms have rapidly evolved from the post-stack time migration to the prestack depth migration. There are two main categories of prestack depth migration: ray-based methods such as Kirchhoff depth migration (KMIG) and beam migration (BMIG), and wave equation based methods such as one-way wave-equation migration (OWEM), and reverse-time migration (RTM). The same imaging principle underlies all these prestack depth migration methods. A reflection involves an incident wave and a scattered wave, commonly called the source and receiver wavefields (we shall use the terms "reflect" and "scatter" loosely and interchangeably). The imaging condition states that the reflector is located where the source and receiver waves are coincident at the same place and time. This is a consequence of the locality of interactions between waves and media. This principle poses migration as the adjoint problem to the linear single-scattering approximation to wave propagation in inhomogeneous media, thereby breaking the task down into two simple steps: one must model two wavefields — the source and the receiver wavefields — and evaluate their zero-lag time-correlation at each subsurface point.

1.1 MIGRATION PROPAGATOR

The ray-based migration methods are not the focus of the thesis. The wave equation based migration methods are the only concern. Wave-equation migrations are one way or full way.

1.1.1 One-way wave equation based migration

In one-way wave-equation migration (OWEM), the source and receiver waves are extrapolated using one-way propagator which expresses a wavefield at a particular depth in terms of the same wavefield existing at a shallower or greater depth. In other words, it admits wave propagation in either up or down going directions. OWEM downward-propagates the source wavefield D and the recorded wavefield U from the surface into the subsurface by solving the one-way wave equations:

$$\left(\frac{\partial}{\partial z}+i\frac{\omega}{V}\sqrt{1+\frac{V^2}{\omega^2}\left(\frac{\partial^2}{\partial x^2}+\frac{\partial^2}{\partial y^2}\right)}\right)U=0, \tag{1.1}$$

$$\left(\frac{\partial}{\partial z}-i\frac{\omega}{V}\sqrt{1+\frac{V^2}{\omega^2}\left(\frac{\partial^2}{\partial x^2}+\frac{\partial^2}{\partial y^2}\right)}\right)D=0. \tag{1.2}$$

The one-way wave equation involves a square root of a partial differential operator. A huge variety of numerical methods were developed to implement this operator. Among them, one approach is dual-domain space-wavenumber methods. These methods approximate the square-root operator by using separable functions in the space and wavenumber domains. Examples include split-step Fourier (SSF) migration (Stoffa et al., 1990); Fourier finite-difference (FFD) (Ristow and Ruhl, 1994), phase-screen, and generalized-screen methods (Huang and Wu, 1992; Le Rousseau and de Hoop, 2001); stable x-k extrapolation (Zhang et al., 2003); and separable approximation (Chen and Liu, 2006).

1.1.2 Reverse-time migration

Reverse-time migration (RTM) was introduced for depth migration from the late 1970s (Baysal et al., 1983; McMechan, 1983; Whitmore, 1983) but has become widely used in recent years due to the increasing imaging challenges posed by the complex geological structures and the affordable computational resources such as Linux clusters.

RTM directly solves the acoustic two-way wave equation

$$\left(\frac{1}{V^2}\frac{\partial^2}{\partial t^2}-\frac{\partial^2}{\partial x^2}-\frac{\partial^2}{\partial y^2}-\frac{\partial^2}{\partial z^2}\right)p\left(\mathbf{x},t\right)=0\,, \tag{1.3}$$

for wavefield propagation. The source wavefield is created from the shot location by propagating forward in time. The receiver wavefields is obtained by propagating the recorded wavefield from its boundary (the recording surface) into the earth with time running backward. Based on the full wave equation, RTM is very faithful in reproducing all kinds of wave propagation phenomena (reflections, refractions, diffractions, multiples, evanescent waves) (Etgen et al., 2009). Its advantages include the accurate handling of rapid spatial velocity variation and imaging without dip angle limitations.

1.1.3 Multi-component seismic data and migration technology

Conventional surface seismic surveys record only compressional or P-waves. The underlying assumption is that the Earth is a fluid medium which only transmits P-wave. However, the Earth allows for shear or S-waves as well. Multicomponent seismic surveys record both P- and S-waves. It is achieved by recording all components of the returning wavefield. Recording both wave modes captures more information related to rock properties so that allows output of important complementary seismic information for comparison with conventional P-wave images and amplitude versus offset (AVO) results. Combining all useful information gives more physical constrains on the estimation of reservoir characteristics.

It also has been observed that utilizing the multi-component seismic data can provide additional illumination to the subsurface, especially in the subsalt region. Due to the huge velocity contrast between the sediments and salt bodies, the P-wave path can only pass through the salt bodies within the range of critical incidence, and the waves beyond the critical angle are completely blocked, resulting in various shadow zones (or blind areas) for subsalt imaging. However, the mode conversion at the salt boundary is a significant factor so that converted waves can penetrate high-velocity salt structure with much less defocusing and reach the shadow zone of P-wave survey. Though acoustic assumption is in general a good approximation for imaging, in such strong-contrast media where the elastic properties are amplified, it is very beneficial to conduct elastic wave migration with multicomponent data.

1.1.4 My contributions on migration propagators

We investigate the possibility of using converted wave for subsalt imaging. Using a simple velocity model, we evaluate the survey efficiency of the converted wave and analyze the reason for the artifacts generated in the migration image. We demonstrate the potential of converted path imaging: it provides additional illumination to the subsalt region compared to acoustic wave migration, and it reduces the artifacts in elastic wave migration. The criteria of converted path selection are provided for subsalt imaging.

We develop a hybrid elastic one-way propagator for strong contrast medium with sharp boundary which treats weak volume scatterings with perturbation based approach and treats the boundary scattering with reflection/transmission operators. The propagator is implemented in dual domain: propagation in wavenumber domain and interaction with scatterings in space domain. It is computationally efficient and is capable to select wave path during migration by switching on/off wave mode at the sharp boundary. The application of the propagator to subsalt imaging is implemented.

1.2 THE IMAGING CONDITION

Although prestack depth migration has long become one of the most important data processing techniques for obtaining subsurface information, traditionally, the primary purpose of the depth migration is providing a geometrical image of the subsurface structures. In the last few decades, facing with more complicated exploration demands, it is expected that more information can be obtained from the depth image. As have been mentioned above, the RTM method based on the full-wave propagator is a preferred prestack depth migration. However, as the imaging condition which is the zero-time-zero-offset cross-correlation is applied to the reconstructed source and receiver wavefields, many useful features of the wavefields are lost. For example, this conventional imaging condition sums up waves from all the directions, thus the directional information of the seismic event is unknown. And it fails to preserve the dynamics of the reconstructed wavefields, so that we cannot directly recover the medium parameters from the image amplitude. If the reconstructed wavefields are vectorized wavefields, the imaging condition will produce a mixed-mode image which is hard to interpret. To retrieve useful information from the depth image, more advanced imaging conditions are required. The rest part of the thesis is focused on these problems.

1.2.1 RTM artifacts

RTM is well known for generating large-amplitude, low-wavenumber artifacts that contaminate the image. These artifacts have been one of the major concerns for RTM. In RTM the forward extrapolated source and backward extrapolated receiver wavefields have the same wavepaths. The correlation of these two wavefields occurs not only at a reflection point, but also at all nonreflection points along the entire wave path. The difference for the cross-correlation is that the two wavefields are propagating in opposite directions at the places other than the true reflection points. So it is important to take the angle information of the wavefields into consideration in order to distinguish the artifacts and true reflections.

1.2.2 Migration gathers

A migration velocity model is derived by evaluating the quality of the flatness or focusing of image gathers, which quantitatively links the image mismatch to velocity error, assuming that correct velocity model yields a flat common image gather or properly focused gathers. The image gathers can be broadly classified as offset gathers and angle gathers. However, a typical image gather in the offset domain shows contamination from artifacts in a complex region due to the nonuniqueness of the image when the imaging condition is applied in the common offset domain (Nolan and Symes, 1996). Angle-domain common image gathers (ADCIGs) do not suffer from this noise and provide the required information for carrying out a migration velocity and amplitude versus angle (AVA) analysis.

1.2.3 True-amplitude imaging

In addition to providing correct geometrical locations of subsurface structures, the true-reflection imaging strives to give correct image amplitudes, which reveal the reflection/scattering strength of the subsurface structures. In this context, the basic requirement is that the migration is "true amplitude". Various reasons justify the claim that the adjoint migration operator only undoes the kinematics of the seismic experiment, is not really amplitude preserving because of incomplete coverage of sources and receivers, incomplete subsurface illumination caused by velocity complexities in the overburden. An ambitious approach is to turn the migration into an inversion procedure. These methods are typically compute-intensive, and tend toward ill-posedness in areas of low illumination. An alternative approach to solve the true-amplitude problem is to modify the imaging condition to be dynamic. In dip angle domain, the image produced by adjoint migration operators can be considered as the true reflectivity filtered by a spatially varying function (Gelius et al., 2002; Lecomte et al., 2003). The function can be explicitly calculated with the background

Green's functions, given a target dip and acquisition configuration. It will lead to a true-amplitude image to filter out the function at the imaging stage.

1.2.4 Angle-domain imaging condition

Most of these imaging tasks require working in the angle domain, i.e., need to know the wave propagation directions in the vicinity of the image point. Unfortunately, the solutions from a full-wave propagator such as the finite-difference method do not explicitly give the angle information, as in the ray-based method. To build angle-domain imaging condition, a variety of techniques have been proposed for RTM and other wave equation migrations, depending on whether decomposition is performed on the wavefields or performed in the image domain. These techniques include 1) those involving plane-wave decomposition of the wavefields prior to application of imaging condition (Xie and Wu, 2002; Soubaras, 2003; Wu et al., 2004; Xu et al., 2010), 2) those involving polarization analysis of the wavefields prior to imaging condition (Yoon et al., 2004; Zhang and McMechan, 2011), and 3) those employing extended imaging conditions (Rickett and Sava, 2002; Sava and Fomel, 2003; Sava and Fomel, 2005; Sava and Vasconcelos, 2011) to generate subsurface offset and/or time-shift gathers that are converted to angle gathers after migration.

1.2.5 My contributions on migration image conditions

A new image condition is proposed to eliminate the large-amplitude, low-frequency artifacts in acoustic RTM. we employ local slant stacking to decompose the source and receiver wavefields into plane wave components and build angle-domain partial images by cross-correlating the plane-wave components from the source wavefield with those from the receive wavefield. A specially designed filter is applied to the angle-domain partial images and successfully suppresses the artifacts.

We extend the angle decomposition technique from acoustic RTM to multicomponent elastic RTM, in which the mixed-mode wavefields are separated into P- and S- modes and each mode is decomposed into a superposition of plane waves. We construct angle-domain imaging conditions for P-P and P-S reflections and extract the corresponding angle gathers. Unlike in the acoustic case, based on Snell's law, the P- and S- wave reflection angles are different. Special care is taken in designing the angle domain operators. With the introduction of different angle-domain operators, we eliminate the low-wavenumber artifacts in P-P image and correct the polarization reversal of the P-S image.

The ADCIG derived from RTM can be used for migration velocity analysis (MVA), but cannot be directly used for AVA analysis even if the gather is flat. To turn the ADCIG into the true-reflectivity, we formulate the target illumination with the plane wave components of Green's functions under the survey configuration and use it to normalize the ADCIG. The resulted AVA responses are analyzed in cross-plot domain and compared to the reservoir parameters. To speed up the calculations of ADCIG and target illumination, we adopt several techniques which make the resulting approach very efficient.

To make the image amplitude represent the true reflectivity, we derive the theory of true-reflection RTM by compensating the migration image with target illumination in the dip angle domain. We provide efficient methods to calculate the common dip image (dip-angle-dependent migration image) and acquisition dip response (dip-angle–dependent target illumination) and demonstrate that the amplitude correction in the dip angle domain can lead to the true-reflection image consistent with the target impedance contrast.

1.3 THESIS CHAPTER SUMMARY

Chapter 1 is this introduction.

Chapter 2 introduces angle domain imaging condition to remove the low-wavenumber artifacts that appear in acoustic RTM image.

Chapter 3 extends the angle decomposition technique from acoustic RTM to elastic RTM. The resulting image conditions can generate the PP and PS ADCIGs and depth images. This method expands the image into matrixes composed of angle-domain partial images, where the specially designed operators can effectively eliminate the low-wavenumber artifacts in PP image and correct the polarization reversal in PS image.

Chapter 4 deals with the AVA (amplitude versus angle) analysis under the RTM framework. The proposed method allows the AVA analysis being conducted on the migrated wavefield right at the target reflector. The effects from complex overburden structures carried by the downward propagated wavefield can be readily eliminated.

Chapter 5 develops a true-reflection RTM method. Both the migration image and the illumination are decomposed into the dip angle domain and the correction in dip angle domain leads to an image consistent with the target impedance contrast.

Chapter 6 provides some physical bases for converted path imaging using a simple elastic model and compares the converted-path imaging with acoustic and elastic wave imaging.

Chapter 7 develops a hybrid elastic one-way propagator for modeling and migration. Compared to the conventional one-way propagator based on the perturbation theory, the new propagator divides the model into multiple domains separated by boundaries with strong impedance contrast. The new propagator is suitable for extrapolate elastic wave through models with large velocity perturbations.

1.4 REFERENCES

Baysal, E., D. D. Kosloff, and J. W.C. Sherwood, 1983, Reverse time migration: Geophysics, 48, 1514–1524.

Chen, J., and H. Liu, 2006, Two kinds of separable approximations for the one-way wave operator: Geophysics, 71, no. 1, T1–T5.

Etgen, J., S. H. Gray, and Y. Zhang, 2009, An overview of depth imaging in exploration geophysics: Geophysics, WCA5-WCA17.

Gelius, L. J., I. Lecomte, and H. Tabti, 2002, Analysis of the resolution function in seismic prestack depth imaging: Geophysical Prospecting, 50, 505–515.

Lecomte, I., I. H. Gjoystdal, and A. Drottning, 2003, Simulated Prestack Local Imaging: a robust and efficient interpretation tool to control illumination, resolution, and time-lapse properties of reservoirs: 73rd Annual International Meeting, SEG, Expanded Abstracts, 1525-1528.

Le Rousseau, J. H., and M.V. de Hoop, 2001, Modeling and imaging with the scalar generalized-screen algorithms in isotropic media: Geophysics, 66, 1551–1568.

Huang, L. J., and R. S. Wu, 1996, Prestack depth migration with acoustic screen propagators: 66th Annual International Meeting, SEG, Expanded Abstracts, 415–418.

McMechan, G. A., 1983, Migration by extrapolation of time-dependent boundary values: Geophysical Prospecting, 31, 413–420.

Nolan, C., and W. Symes, 1996, Imaging in complex velocities with general acquisition geometry: Trip, The Rice Inversion Project, Rice University.

Rickett, J. E., and P. C. Sava, 2002, Offset and angle-domain common image-point gathers for shot-profile migration: Geophysics, 67, 883-889.

Ristow, D., and T. Ruhl, 1994, Fourier finite-difference migration: Geophysics, 59, 1882–1893.

Sava, P., and S. Fomel, 2003, Angle-domain common image gathers by wavefield continuation methods: Geophysics, 68, 1065-1074.

Sava, P., and S. Fomel, 2005, Time-shift imaging condition: 75th Annual International Meeting, SEG, Expanded Abstracts, 1850-1853.

Sava, P., and I. Vasconcelos, 2011, Extended imaging condition for wave-equation migration: Geophysical Prospecting, 59, 35–55.

Soubaras, R., 2003, Angle gathers for shot-record migration by local harmonic decomposition: 73th Annual International Meeting, SEG, Expanded Abstracts, 889-892.

Stoffa, P. L., J. T. Fokkema, R. M. de Luna Freire, and W. P. Kessinger, 1990, Split-step Fourier migration: Geophysics, 55, 410–421.

Whitmore, N. D., 1983, Iterative depth migration by backward time propagation: 53rd Annual International Meeting, SEG, Expanded Abstracts, Session: S10.1.

Xie, X. B., and R. S. Wu, 2002, Extracting angle domain information from migrated wavefields: 72nd Annual International Meeting, SEG, Expanded Abstracts, 1360-1363.

Xu, S., Y. Zhang, and B. Tang, 2011, 3D common image gathers from reverse time migration: Geophysics, 76, S77–S92.

Yoon, K., K. Marfurt, and E. W. Starr, 2004, Challenges in reverse-time migration: 74th Annual International Meeting, SEG, Expanded Abstracts, 1057–1060.

Zhang, Q., and G. A. McMechan, 2011a, Direct vector-field method to obtain angle-domain common-image gathers for isotropic acoustic and elastic reverse-time migration: Geophysics, 76, WB135-WB149.

Zhang, Y., C. Notfors, and Y. Xie, 2003, Stable x-k wavefield extrapolation in a medium: 73rd Annual International Meeting, SEG, Expanded Abstracts, 1083–1086.

2 A NEW ANGLE-DOMAIN IMAGING CONDITION FOR ACOUSTIC REVERSE-TIME MIGRATION

2.1 SUMMARY

Based on the full-wave equation, reverse-time migration (RTM) can handle wave propagation in all directions without angle limitation. However, the wide-angle capability of full-wave propagator creates artifacts in migrated image if the conventional imaging condition (zero-lag cross-correlation) is applied. In this chapter, we propose a new imaging condition to attenuate these artifacts. We first decompose the source and receiver wavefields into local plane waves (or beams) in different propagation directions, followed by constructing partial images from individual source and receiver plane waves. Then, an angle-domain filter is applied to these partial images to separate the image from the artifact. Synthetic examples demonstrate that this imaging condition can effectively remove the undesired artifacts in both simple and complex models.

2.2 INTRODUCTION

Reverse-time migration (RTM) has become increasingly attractive in the oil and gas industry because of its robustness in imaging subsurface structures in complex geological models. The RTM reconstructs forward propagated source wavefield and back propagated receiver wavefield by full-wave propagator. It then applies an imaging condition to extract reflectivity information from the reconstructed wavefields (Baysal et al., 1983; McMechan, 1983; Whitmore, 1983). The RTM is highly flexible in handling complicated velocity models and reproduces realistic wave phenomena (e.g., reflections, refractions, diffractions, and evanescent waves). The full-wave equation based RTM can propagate waves in all directions without any angle limitation and image steep structures with dip angles up to 180°, giving it advantages over other migration methods (Etgen et al., 2009). However, the wide-angle capability of full-wave propagator creates strong artifacts in the migrated image if conventional imaging condition is applied. The migration imaging condition can be expressed as a zero-lag cross-correlation between source and receiver wavefields. The artifacts result from the spurious cross-correlation of head waves, diving waves and backscattered waves at the imaging step (Yoon et al., 2004). These events are particularly serious where high velocity contrasts or high velocity gradient exists.

Several approaches have been proposed to solve this imaging problem. For post-stack RTM, these artifacts can be effectively suppressed by matching the impedance of the media, i.e., utilizing the non-reflecting wave equation (Baysal et. al, 1984) or by smoothing the velocity model to reduce the reflections (Loewenthal, et. al, 1987). In the case of prestack RTM, several filters have been proposed to remove these artifacts at the post-image stage (e.g., Youn and Zhou, 2001; Mulder and Plessix, 2004; Guitton et al., 2006). Fletcher et al. (2005) suppressed the image artifacts by introducing a directional damping term to the non-reflecting wave equation.

Angle-related imaging conditions have been explored by several authors to only keep the true reflection energy in the final image. Under this category, Yoon et al. (2004)

suggested putting a weighting function to the imaging condition in terms of the reflection angle, which is calculated from Poynting vectors of source and receiver waves. Xie and Wu (2006) decomposed the full wavefields into their one-way components along horizontal and vertical directions by Rayleigh integral and applied the imaging condition to the appropriate combinations of the wave components. Liu et al. (2007) tested the vertical wave imaging condition, but they used Fourier transform to get one-way component. Denli and Huang (2008) separated the wavefields into one-way components with an f-k filter. Suh and Cai (2009) explored the vertical and horizontal wave imaging condition and also applied an fan filter to remove the residual artifacts in space domain.

In the above mentioned angle-domain imaging conditions, the wave propagation direction is extracted by the differential method. In a complex velocity model, due to the reflection, scattering, multi-pathing, etc., the source or receiver waves may come to a given location from various directions at the same time. The differential method sometimes fails to give the right propagation direction.

In this chapter, we propose an angle domain method to eliminate the migration artifacts. We first decompose the reconstructed wavefields into plane waves along different propagating directions using local slant stacking, which is an integration method. Second, we construct the local image matrix (LIM) which is composed of partial images from angle-domain source and receiver waves. Based on the energy distributions in LIM, we introduce an angle-domain filter to separate the true reflections from the artifacts. Finally, we apply the new angle-domain imaging condition to a salt dome model and a portion of BP model to demonstrate its validity.

2.3 CONVENTIONAL IMAGING CONDITION

The implementation of acoustic RTM consists of two steps: wave reconstruction and application of imaging condition. The first step is to reconstruct both source and receiver wavefields in the subsurface using finite difference scheme. On the source-side, the wavefields are reconstructed by solving acoustic wave equation with an explosion source (Aki and Richards, 1980):

$$\rho \frac{\partial^2 u_s(\mathbf{x},t)}{\partial t^2} - \kappa \nabla^2 u_s(\mathbf{x},t) = \delta(\mathbf{x}-\mathbf{x}_s) s(t), \tag{2.1}$$

where $s(t)$ is the source time function, $\mathbf{x}_s$ is the source location; $u_s(\mathbf{x},t)$ is the source wavefield, ρ is the density and κ is the bulk modulus. On the receiver-side, the recorded seismic data is set to be the boundary condition of the acoustic wave equation:

$$\begin{cases} \rho \dfrac{\partial^2 u_g(\mathbf{x},t)}{\partial t^2} - \kappa \nabla^2 u_g(\mathbf{x},t) = 0, \\ u_g(\mathbf{x},t)\big|_B = u_0(\mathbf{x},t), \end{cases} \tag{2.2}$$

where $u_0(\mathbf{x},t)$ is the seismic data recorded at the receiving surface and $u_g(\mathbf{x},t)$ is the receiver wavefield.

The second step is to apply the imaging condition to the reconstructed wavefields. Conventionally, it can be expressed as zero-lag cross-correlation between source and receiver wavefields (Claerbout, 1985):

$$I(\mathbf{x})=\int_0^T u_s(\mathbf{x},t)\,u_g(\mathbf{x},T-t)\,dt, \tag{2.3}$$

where $I(\mathbf{x})$ is the image at location $\mathbf{x}$, T is the total recording time, $u_s(\mathbf{x},t)$ and $u_g(\mathbf{x},t)$ are the reconstructed source and receiver wavefields, respectively. This correlation represents the "same time same place" physical requirement, however, produces significant amounts of large-amplitude, low frequency artifacts. Figure 2.1 illustrates the reason for the generation of artifacts. The full wave equation used in RTM properly simulates wave propagation in all directions including both reflections and transmissions, and consequently the forward extrapolated source and backward extrapolated receiver wavefields have the same wavepaths. The cross-correlation of these two wavefields then produces an amplitude not only at a reflection point (Figure 2.1a), but also at all nonreflection points (Figure 2.1b) along the entire wave path. But the difference for the cross-correlation is that the two wavefields are propagating in opposite directions at the places other than the true reflection points. So it is important to take the angle information of the wavefields into consideration in order to distinguish the artifacts and true reflections.

2.4 PLANE WAVE DECOMPOSITION

To build an angle-domain imaging condition, both source and receiver wavefields need to be decomposed into superposition of local plane waves (or beams) propagating in different directions. Techniques such as local slant stacking (Xie and Wu, 2002) and beamlet decomposition (Wu and Chen, 2002, 2003; Soubaras, 2003; Chen et al. 2006; Wu and Mao, 2007; Wu et al., 2008) have been developed for one-way wave equation based migration methods. However, they may not lead to good results when applied to RTM. To handle the full wavefield, calculations need be performed in both horizontal and vertical directions (Cao and Wu, 2009). Time-domain local slant stacking (Xie and Lay, 1994; Xie et al., 2005; Xie and Yang, 2008; Yan and Xie, 2009; 2010) and windowed FFT (Zhang et al., 2010; Xu et al., 2011) have been proposed for this purpose. Here by combining the method for one-way migration (slant stack in frequency domain) and the time domain method (slant stack in multi-dimensional space), we present a slowness-based decomposition. We first use Fourier transform to convert the reconstructed wavefields from time domain to frequency domain. In the frequency domain, the wavefield $u(\mathbf{x},\omega)$ is decomposed into slowness domain

$$u(\mathbf{p},\mathbf{x},\omega)=\int W(\mathbf{x}'-\mathbf{x})u(\mathbf{x}',\omega)\cdot e^{-i\omega(\mathbf{x}'-\mathbf{x})\cdot\mathbf{p}}d\mathbf{x}', \tag{2.4}$$

where $\mathbf{u}(\mathbf{p},\mathbf{x},\omega)$ is the decomposed wave in local slowness domain, $W(\mathbf{x}'-\mathbf{x})$ is a window function centered at $\mathbf{x}$, $\mathbf{p}$ is the slowness vector and $\hat{\mathbf{e}}=\mathbf{p}/p$ is a unit vector towards the propagation direction, p is the absolute value of $\mathbf{p}$.

Illustrated in Figure 2.2 is a flow chart of slowness analysis at an image point $\mathbf{x}$ in 2D geometry. The frequency-domain source and receiver wavefields are sampled by a spatial window and shown as data volumes 2.2a and 2.2b. Using equation 2.4, they can be transformed to slowness-frequency data volumes 2.2c and 2.2d. Shown in Figure 2.2e and 2.2f are the cross-sections of data volumes 2.2c and 2.2d at the dominant frequency. As an example, we demonstrate the results of slowness analysis in a salt dome model (Figure 2.3) which is composed of a background with a vertical velocity gradient and a salt dome with steep flanks. Overlapped on the salt model is a snapshot generated from the labeled source location. On the top and bottom of the figure are samples of slowness analyses at selected locations indicated in the wavefield. The slowness vectors, i.e., the vectors from the origin of the polar coordinate to these energy peaks, reveal the wave propagation directions and their slowness. At the location simultaneously swept by multiple wave fronts, multiple energy peaks are shown in slowness domain, but without exception all the energy peaks fall on a circle with a radius of $1/\bar{v}$, where $\bar{v}$ is the average velocity within the sampling window W. That's where the dispersion relation is satisfied. With the increase of depth, the radii of these circles become smaller due to the increase of velocities. These results demonstrate that in the slowness domain the wave energy is distributed around the dispersion circles and each energy peak denotes a local plane wave. This indicates that to decompose the wavefield into local plane waves, we do not need to compute every component in the slowness domain by converting 2.2a and

2.2b into 2.2c and 2.2d. Rather, we only calculate 2.2g and 2.2h along dispersion circles and end up with 2.2g and 2.2h. In this way, the computational cost will be tremendously reduced. In 2D case, the decomposition process can be written as (see Appendix 2A)

$$u(\mathbf{x},\omega)=\sum_{\theta}u(\theta,\mathbf{x},\omega), \tag{2.5}$$

where

$$u(\theta,\mathbf{x},\omega)=\frac{\omega}{\overline{v}}\cdot u\left(\mathbf{p}=\frac{1}{\overline{v}}\hat{\mathbf{e}}_{\theta},\mathbf{x},\omega\right), \tag{2.6}$$

where $u(\theta,\mathbf{x},\omega)$ is the local plane wave; $\hat{\mathbf{e}}_{\theta}$ is the unit vector specifying the propagation direction of the local plane wave θ; $\overline{v}$ is the average velocity in the sampling window W; $\omega/\overline{v}$ is the Jacobian coefficient from the slowness domain to angle domain.

2.5 ANGLE-DOMAIN IMAGING CONDITION

In the frequency domain, the conventional imaging condition can be expressed as the convolution between the incident (source side) and scattered (receiver side) waves, i.e.,

$$I(\mathbf{x})=\sum_{\omega}u_s(\mathbf{x},\omega)\cdot u_g^*(\mathbf{x},\omega), \tag{2.7}$$

where I is the depth image; $*$ denotes complex conjugate. To obtain the angle-domain imaging condition, we substitute equation 2.5 into equation 2.7 and obtain

$$I(\mathbf{x})=\sum_{\theta_s}\sum_{\theta_g}I(\theta_s,\theta_g,\mathbf{x}), \tag{2.8}$$

where

$$I\left(\theta_s,\theta_g,\mathbf{x}\right)=\sum_{\omega}u_s\left(\theta_s,\mathbf{x},\omega\right)\cdot u_g^*\left(\theta_g,\mathbf{x},\omega\right), \tag{2.9}$$

is the angle-domain partial image; θ_s and θ_g are incident and scattering angles, respectively.

2.6 LOCAL IMAGE MATRIX

Equation 2.8 expands the scalar image into a matrix as a function of incident and scattering angles. We call the matrix Local Image Matrix (LIM). For convenience, we convert the acquisition coordinate $\left(\theta_s,\theta_g\right)$ into target coordinate $\left(\theta_r,\theta_d\right)$, where θ_d is the target dipping angle and θ_r is the reflection angle defined as the incident angle relative to the reflector normal. The sketch in Figure 2.4a gives the relationship between the two angle pairs.

For the P-P reflection, the coordinate transform can be expressed as (e.g., Xie and Wu, 2002)

$$\theta_d=\left(\theta_s+\theta_g\right)/2, \tag{2.10}$$

and

$$\theta_r=\left(\theta_s-\theta_g\right)/2. \tag{2.11}$$

Illustrated in Figure 2.4b is the structure of a 2D LIM, where the horizontal and vertical coordinates are axes of incident and scattering angles, the main and secondary diagonals are axes of the reflection and dip angles. Note that for a one-way propagator, the maximum incident, scattering, dip and reflection angles in the LIM can only reach to $\pm\pi/2$. In contrast, in RTM, the full-wave propagator can make the incident, scattering, dip and reflection angles in the LIM all the way to $\pm\pi$.

Location A and B are not related to any real targets but dominated by strong artifacts generated from turning waves. The LIMs calculated for these locations show that the energy is concentrated at reflection angle $\theta_r = \pm\pi/2$. These artifacts are generated by incident turning wave and back-propagated turning waves from both source and receiver sides. They reach to the image location nearly parallel but with opposite directions. In a long range, these signals will correlated and generate strong image artifacts. The energy distributed at reflection angle $\pm\pi/2$ correctly describes their property. Location C is on the horizontal interface and the energy distribution reveals it is properly imaged by near vertical incident and scattered waves. The dipping angle is zero (refer to Figure 2.6). At location E and F, the energy distribution shows that the target dipping angle is nearly $-\pi/2$ and the image is generated by near normal incident waves, i.e., their reflection angles are nearly zero. Location D is located on the target. There are two clusters of energy in its image matrix. One is generated by reflection energy located at zero dipping angle and near 40 degree reflection angle. The other is generated by artifacts which have a near $\pi/2$ reflection angle. These results show that the reflection signals and artifacts behave differently in the LIM. The artifacts in RTM are usually generated by correlations between turning or back-scattered waves and their time-reversed counterparts along wave paths. These events appear as very wide angle "reflections" with reflection angles near $\pi/2$. Note that for a one-way propagator, the maximum incident, scattering, dipping and reflection angles in the LIM can only reach to $\pm\pi/2$. In contrast, the full-wave propagator in RTM can extend them all the way to $\pm\pi$. That is why the RTM causes serious artifacts but a one-way migration does not.

2.7 ANGLE-DOMAIN FILTER

The conventional image contains the energy from all possible directions. It can be obtained by summing up all the elements in the LIM:

$$I(\mathbf{x}) = \sum_{\theta_r}\sum_{\theta_d} I(\theta_r, \theta_d, \mathbf{x}). \tag{2.12}$$

In this way, the wide-angle events will enter the image and cause artifacts. Thus, we can eliminate the artifacts by blocking the very wide-angle energy from entering the image. Based on this consideration, our angle-domain imaging condition can be expressed as

$$I(\mathbf{x}) = \sum_{\theta_r}\sum_{\theta_d} M(\theta_r, \theta_d) I(\theta_r, \theta_d, \mathbf{x}), \tag{2.13}$$

where the angle domain filter $M(\theta_r, \theta_d)$ is designed to attenuate events with very wide reflection angles. For example, we can choose to eliminate all the energy with reflection angles larger than certain values from the LIM.

2.8 NUMERICAL EXAMPLES

We use two velocity models to demonstrate the validity of the new imaging condition. The first numerical experiment is conducted in the salt model (Figure 2.7a) used in the previous section. The acquisition system contains 21 shots with double-side receivers and the maximum number of receivers for one shot is 300. A 2D fourth-order full-wave finite-difference code is used to generate the seismic data as well as to reconstruct the source and receiver wavefields. Figure 2.7b is the migrated image using the conventional imaging condition. Both the horizontal interface and the vertical flank of the salt dome are properly imaged. However, there are strong long-wavelength artifacts on the top and both sides of the salt body. These artifacts prevent us from obtaining detailed structures in these areas. In Figure 2.7c, the new imaging condition proposed in this paper has been applied and the result shows improved image. Most of those long wavelength migration artifacts disappear, while the image of reflector is well preserved.

We then test this imaging condition on the 2D BP dataset (Billette et al., 2005). Figure 2.8a shows the conventional image for part of the BP model. Although the boundary of the salt body can be seen in the figure, the region above the salt is strongly contaminated by the migration artifacts. The shallow structures are nearly invisible due to large-amplitude artifacts. Figure 2.8b is the result obtained by using the new imaging condition. The shallow part, especially the structures in the sediment, becomes identifiable.

2.9 CONCLUSIONS

The chapter intends to suppress the artifacts appearing in acoustic RTM by taking account of the wave propagation directions of the reconstructed wavefields. We decompose the source and receiver wavefields into local plane waves along different directions using local slant stacking and construct LIM (a collection of partial images) by cross-correlating any combination of these plane waves. And then we formulate an imaging condition as a product of an angle-domain operator and the partial images. The introduction of the angle-domain operators substantially reduces the artifacts in the migration image.

2.10 APPENDIX 2A: JACOBIAN COEFFICENT FROM WAVENUMBER DOMAIN TO ANGLE DOMAIN

Wave decomposition and reconstruction can be expressed as

$$u(\mathbf{k},\mathbf{x},\omega)=\frac{1}{2\pi}\int W\left(\mathbf{x}'-\mathbf{x}\right)u\left(\mathbf{x}',\omega\right)\cdot e^{-i\mathbf{k}\cdot(\mathbf{x}'-\mathbf{x})}d\mathbf{x}', \tag{2.A1}$$

and

$$u(\mathbf{x},\omega)=\int u(\mathbf{k},\mathbf{x},\omega)d\mathbf{k}, \tag{2.A2}$$

where $\mathbf{u}\left(\mathbf{x},\omega\right)$ is the original wavefield; $\mathbf{u}\left(\mathbf{k},\mathbf{x},\omega\right)$ is its wavenumber component, $W\left(\mathbf{x}'-\mathbf{x}\right)$ is a window function centered at $\mathbf{x}$.

Equation 2.A2 can be written in 2D polar coordinate as

$$u(\mathbf{x},\omega)=\int u(k,\theta,\mathbf{x},\omega)kdkd\theta, \tag{2.A3}$$

where θ is the polar angle and k is the absolute value of $\mathbf{k}$. Equation 2.A3 means that the original wave can be reconstructed with all the angle components

$$u(\mathbf{x},\omega)=\int u(\theta,\mathbf{x},\omega)d\theta, \tag{2.A4}$$

with the angle component as

$$u(\theta, \mathbf{x}, \omega) = \int u(k, \theta, \mathbf{x}, \omega) k dk \ . \tag{2.A5}$$

Since the wave energy satisfies the dispersion relation, it is proposed to conduct the wavefields along the dispersion circle $k = \omega/v$. This can be achieved by introducing a delta function to equation 2.A5

$$u(\theta, \mathbf{x}, \omega) = \int \delta\left(k - \omega/v\right) u(k, \theta, \mathbf{x}, \omega) k dk \ , \tag{2.A6}$$

and it yields the equation for local slant stacking

$$u(\theta, \mathbf{x}, \omega) = \frac{\omega}{v} u(\mathbf{k} = \frac{\omega}{v} \hat{e}_\theta, \mathbf{x}, \omega) \ , \tag{2.A7}$$

where $\hat{\mathbf{e}}_\theta$ the unit vector with polar angle θ, and ω/v is the Jacobian coefficient from the 2D wavenumber domain to angle domain and equation 2. A1 gives

$$u(\mathbf{k} = \frac{\omega}{v} \hat{e}_\theta, \mathbf{x}, \omega) = \frac{1}{2\pi} \int W\left(\mathbf{x}' - \mathbf{x}\right) u\left(\mathbf{x}', \omega\right) \cdot e^{-i \frac{\omega}{v} \hat{\mathbf{e}}_\theta \cdot (\mathbf{x}' - \mathbf{x})} d\mathbf{x}' \ . \tag{2.A8}$$

2.11 REFERENCES

Aki, K., and P.G. Richards, 1980, Quantitative seismology: Theory and methods, W. H. Freeman and Co.

Baysal, E., D. D. Kosloff, and J. W.C. Sherwood, 1983, Reverse time migration: Geophysics, 48, 1514–1524.

———, 1984, A two-way nonreflecting wave equation: Geophysics, 49, 132–141.

Billette, F., and S. Brandsberg-Dahl, 2005, The 2004 BP velocity benchmark: 67th Annual Conference and Exhibition, EAGE, Extended Abstracts, B035.

Cao, J., and R. S. Wu, 2009, Full-wave directional illumination analysis in the frequency domain: Geophysics, 74, S85-S93.

Chen, L., R.S. Wu, and Y. Chen, 2006, Target-oriented beamlet migration based on Gabor-Daubechies frame decomposition: Geophysics, 71, S37–S52.

Claerbout, J., 1985, Imaging the earth's interior: Blackwell Scientific Publications, Inc.

Denli H., and L. Huang, 2008, Elastic-wave reverse-time migration with a wavefield-seperation imaging condition: 78th Annual International Meeting, SEG, Expanded Abstracts, 2346–2350.

Fletcher, R. P., P. J. Fowler, and P. Kitchenside, 2005, Suppressing artifacts in prestack reverse time migration: 75th Annual International Meeting, SEG, Expanded Abstracts, 2049–2051.

Guitton, A., B. Kaelin, and B. Biondi, 2006, Least-square attenuation of reverse-time migration artifacts: 76th Annual International Meeting, SEG, Expanded Abstracts, 2348–2352.

Liu, F., G. Zhang, S. A. Morton, and J. P. Leveille, 2007, Reverse-time migration using one-way wavefield imaging condition: 77th Annual International Meeting, SEG, Expanded Abstracts, 2170-2174.

Loewenthal, D., P. A. Stoffa, and E. L. Faria, 1987, Suppressing the unwanted reflections of the full wave equation: Geophysics, 52, 1007-1012.

McMechan, G. A., 1983, Migration by extrapolation of time-dependent boundary values: Geophysical Prospecting, 31, 413–420.

Mulder, W.A., and R.E. Plessix, 2004, A comparison between one-way and two-way wave-equation migration: Geophysics, 69, 1491-1504.

Soubaras, R., 2003, Angle gathers for shot-record migration by local harmonic decomposition: 73th Annual International Meeting, SEG, Expanded Abstracts, 889-892.

Suh, S. Y., and J. Cai, 2009, Reverse-time migration by fan filtering plus wavefield decomposition: 79th Annual International Meeting, SEG, Expanded Abstracts, 2804-2807.

Whitmore, N. D., 1983, Iterative depth migration by backward time propagation: 53rd Annual International Meeting, SEG, Expanded Abstracts, Session: S10.1.

Wu, R. S., and L. Chen, 2002, Mapping directional illumination and acquisition aperture efficacy by beamlet propagators: 72nd Annual International Meeting, SEG, Expanded Abstracts, 1352-1355.

———, 2003, Prestack depth migration in angle-domain using beamlet decomposition: Local image matrix and local AVA: 73rd Annual International Meeting, SEG, Expanded Abstracts, 973–976.

Wu, R. S., and J. Mao, 2007, Beamlet migration using local harmonic bases: 77th Annual International Meeting, SEG, Expanded Abstracts, 2230-2234.

Wu, R. S., Y. Wang, and M. Luo, 2008, Beamlet migration using local cosine basis: Geophysics, 73, 207-217.

Xie, X. B., and T. Lay, 1994. The excitation of explosion Lg, a finite-difference investigation. Bull. Seis. Soc. Am. 84, 324-342.

Xie, X. B., Z. Ge, and T. Lay, 2005, Investigating explosion source energy partitioning and Lg-wave excitation using a finite-difference plus slowness analysis method: Bull. Seism. Soc. Am. 95, 2412-2427.

Xie, X. B., and R. S. Wu, 2002, Extracting angle domain information from migrated wavefields: 72nd Annual International Meeting, SEG, Expanded Abstracts, 1360-1363.

Xie, X. B., and R. S. Wu, 2006, A depth migration method based on the full-wave reverse-time calculation and local one-way propagation: 76th Annual International Meeting, SEG, Expanded Abstracts, 2333-2337.

Xie, X. B., and H. Yang, 2008, A full-wave equation based seismic illumination analysis methods: 70th Conference and Exhibition, EAGE, Extended Abstract, P284.

Xu, S., Y. Zhang, and B. Tang, 2011, 3D common image gathers from reverse time migration: Geophysics, 76, S77–S92.

Yan, R., and X. B. Xie, 2009, A new angle-domain imaging condition for reverse time migration: 79th Annual International Meeting, SEG, Expanded Abstracts, 2784-2788.

Yan, R., and X. B. Xie, 2010, A new angle-domain imaging condition for elastic reverse time migration: 80th Annual International Meeting, SEG, Expanded Abstracts, 3181-3186.

Yoon, K., K. Marfurt, and E. W. Starr, 2004, Challenges in reverse-time migration: 74th Annual International Meeting, SEG, Expanded Abstracts, 1057–1060.

Youn, O., and H. W. Zhou, 2001, Depth imaging with multiples: Geophysics, 66, 246-255.

Zhang, Y., S. Xu, B. Tang, B. Bai, Y. Huang and T. Huang, 2010, Angle gathers from reverse time migration: The Leading Edge, 29, 1364 – 1371.

2.12 FIGURES AND TABLES

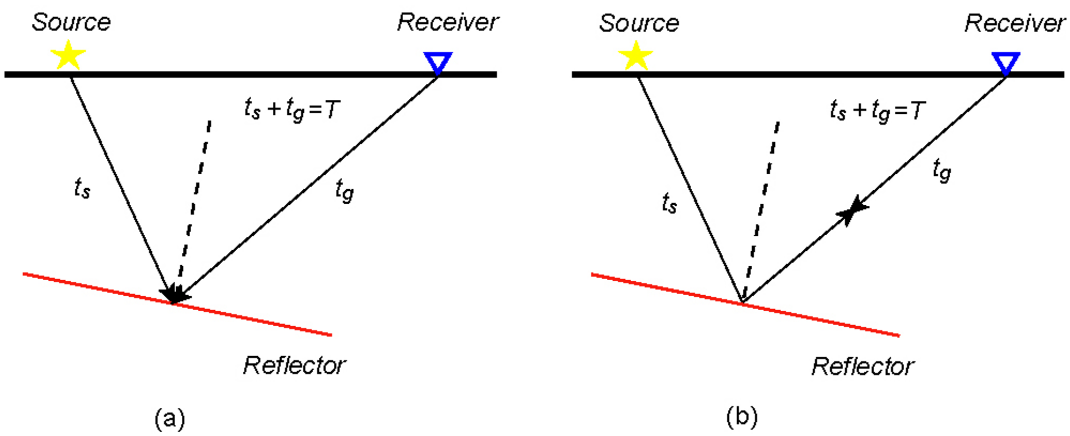

Figure 2.1 The sketch illustrates the creation of the true image and low-wavenumber artifacts. The source and receiver wavefields satisfy the imaging condition at the true reflector (a) and along the ray path (b). t_s is the travel time from the source to the image point and t_g is the travel time from the receiver to the image point. T is the total recording time.

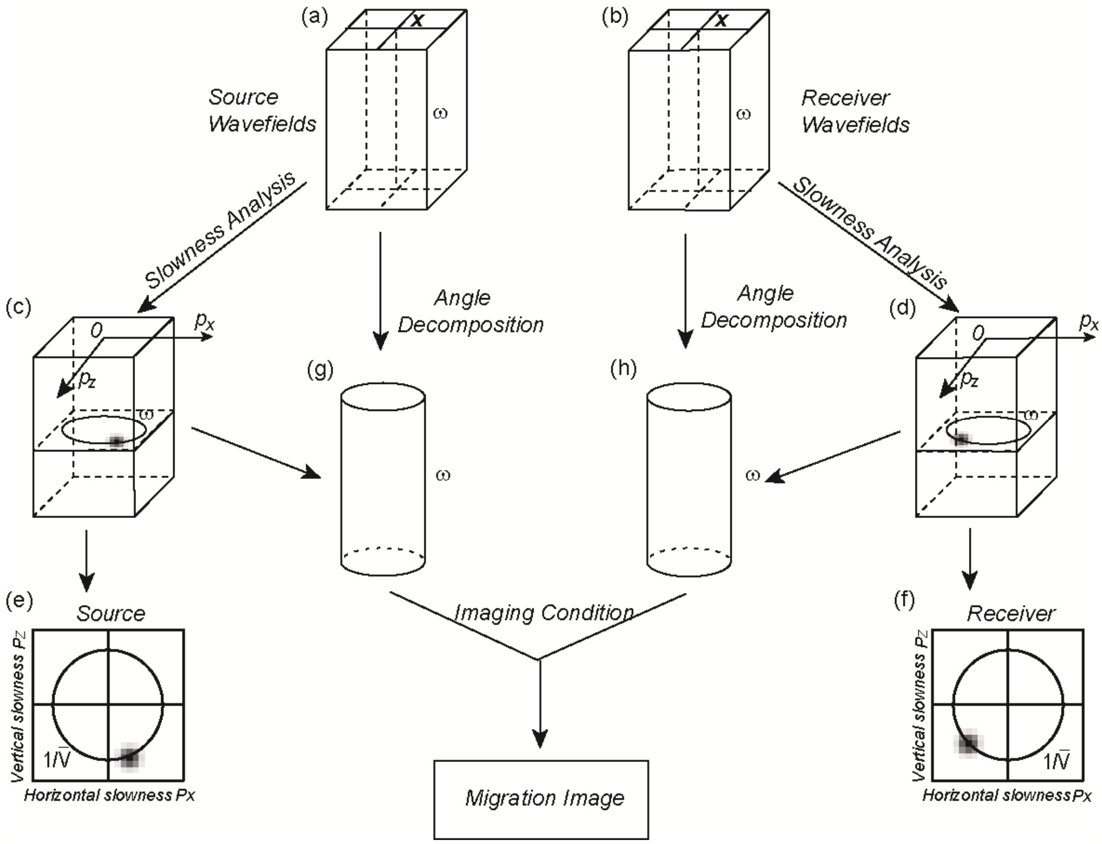

Figure 2.2 The workflow of slowness analysis. The space-frequency domain source and receiver wavefields (a) and (b) are transformed to slowness domain data (c) and (d). (e) and (f) are cross-sections of (c) and (d) at dominant frequency . Note, in the slowness domain, local plane waves appear as energy peaks fall on the dispersion circle. Thus, the slowness analyses only need be calculated for cylindrical regions in (g) and (h). Details see the text.

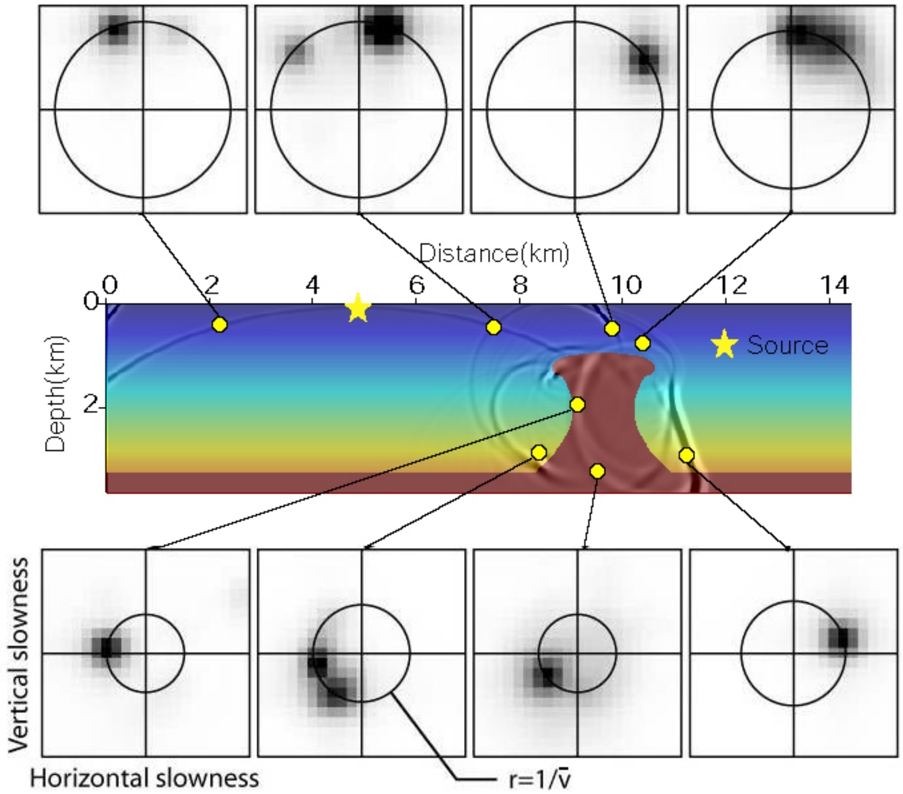

Figure 2.3 Slowness analyses performed for forward propagated wavefield in a five-layer model. In the center is the velocity model superimposed by the snapshot.

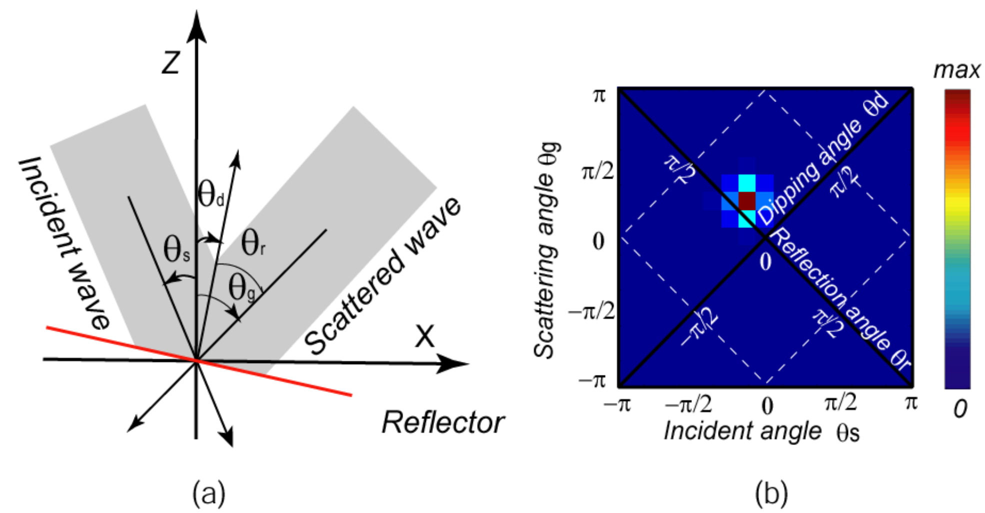

Figure 2.4 Sketch showing the calculation of LIM (a) Coordinate system used in local angle-domain analysis (b) LIM. The horizontal and vertical coordinates are incidence and scattering angles, respectively, while the two diagonals are dipping angle and reflection angle, respectively.

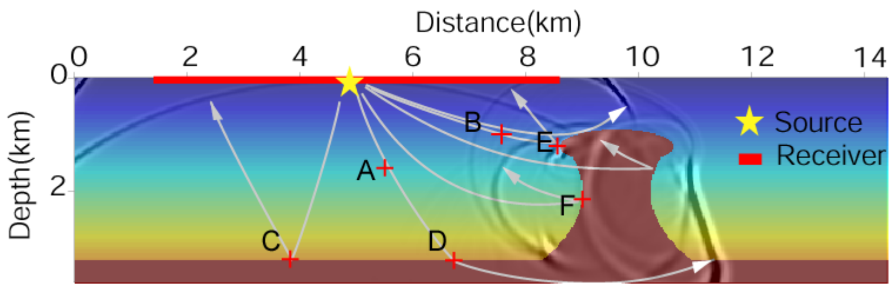

Figure 2.5 Velocity model used to demonstrate the new imaging condition. Superimposed in the figure is the snapshot from a single shot. The rays explain different waves generated in the model.

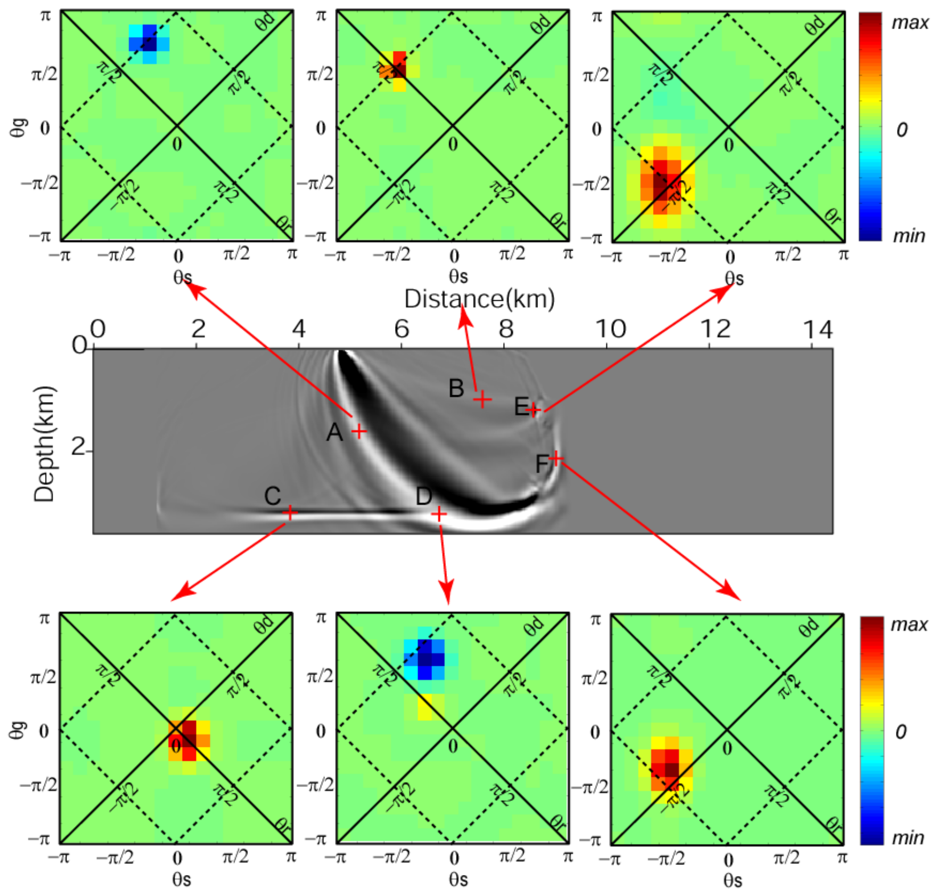

Figure 2.6 The RTM image for the salt dome model generated using a single shot and conventional imaging condition. The image matrices for selected locations in the figure are calculated. The energy for true reflections and artifacts show different behavior in LIM.

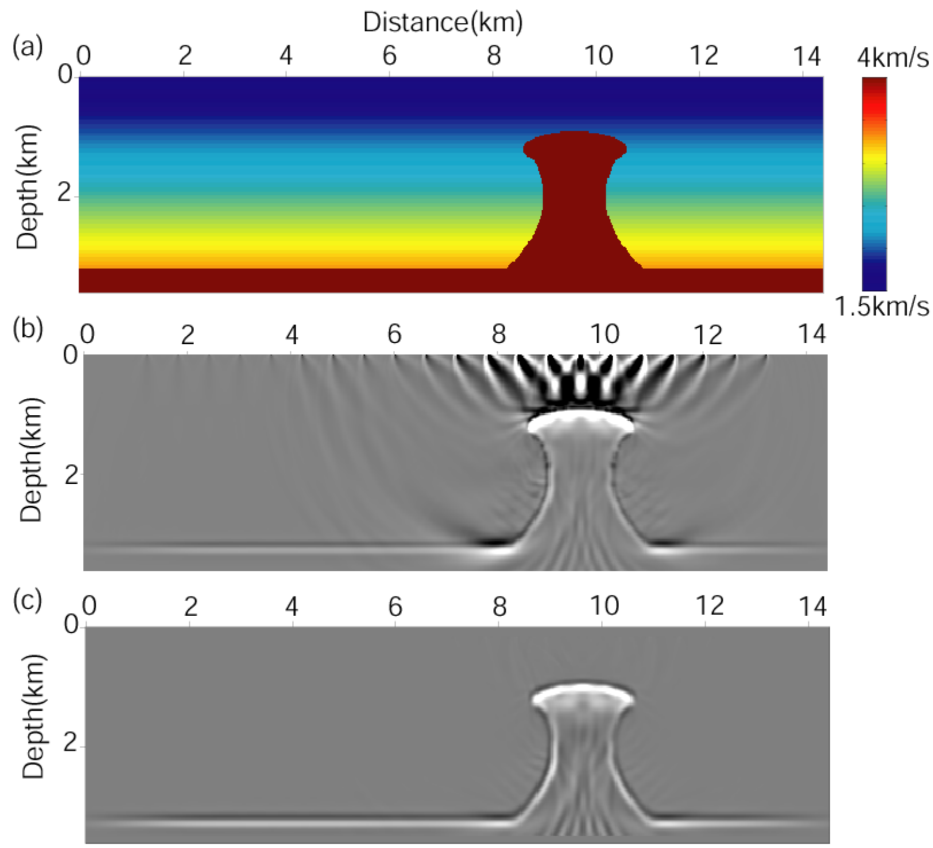

Figure 2.7 Comparison between the prestack depth image using different imaging conditions, with a) the velocity model, b) the multi-shot image using the conventional imaging condition, and c) the image using the new imaging condition. Note the migration artifacts are mostly removed.

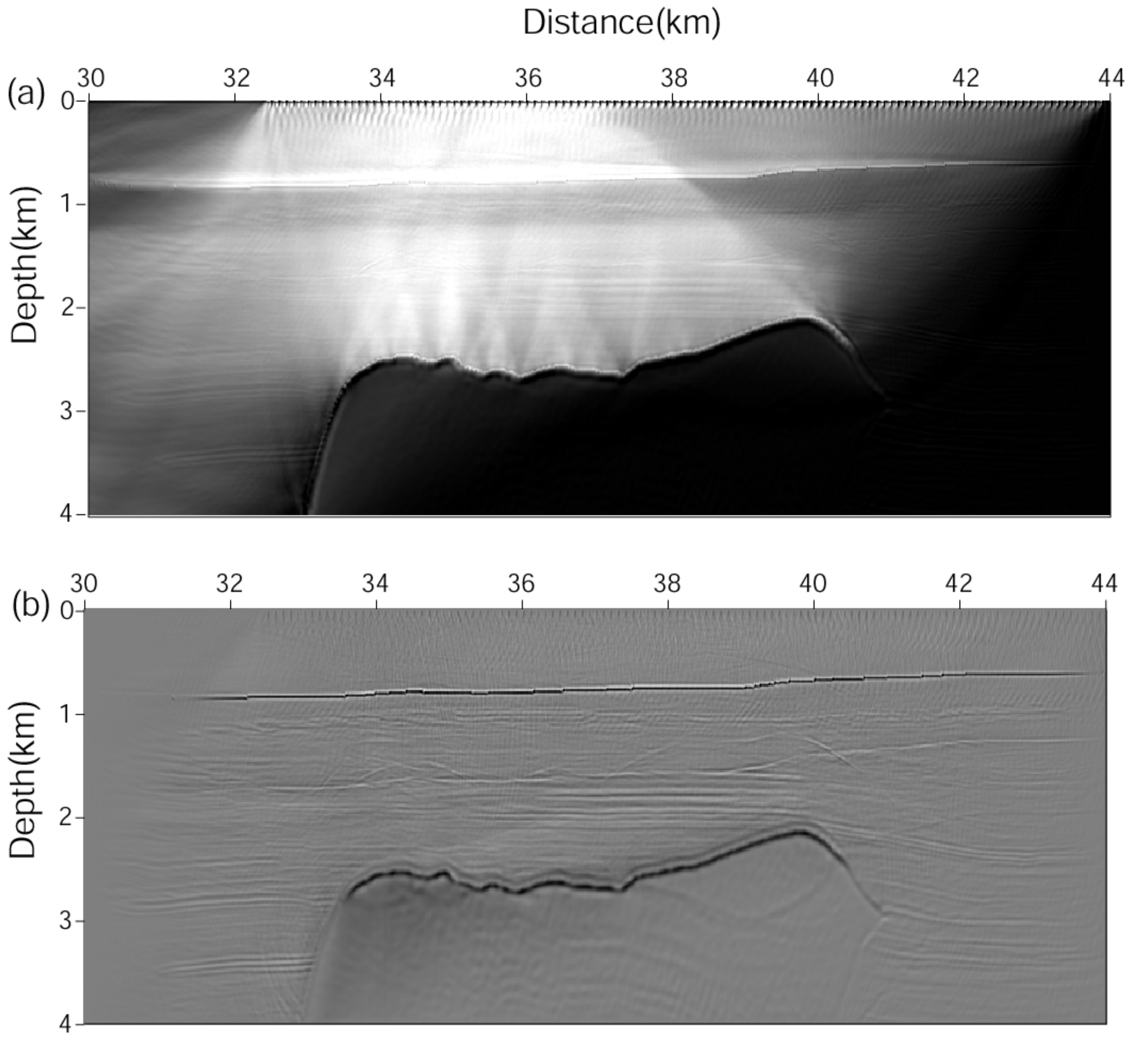

Figure 2.8 Prestack depth image for part of the BP data set, with a) the image using the conventional imaging condition, and b) using the new angle-domain imaging condition.

3 A NEW ANGLE-DOMAIN IMAGING CONDITION FOR ELASTIC REVERSE-TIME MIGRATION[1]

3.1 SUMMARY

An angle-domain imaging condition is proposed for multicomponent elastic reverse-time migration. The local slant stacking method is used to separate source and receiver waves into P- and S-waves and simultaneously decompose them into local plane waves along different propagation directions. We calculate the partial images by cross-correlating the incident and scattered plane P- and S-waves, and then organize all the partial images into P-P and P-S local image matrices. These partial images preserve all the angle-related information. Thus, by working in the image matrix, it is convenient to perform different angle-related operations (e.g., filtering artifacts, correcting polarity or conducting illumination and acquisition aperture compensations) or extract a variety of angle-domain information (e.g., calculating different angle-domain common image gathers or amplitude versus angle). Because the image matrix is localized, these operations can be designed to be highly flexible, e.g., target-oriented, dip-angle-dependent or reflection-angle-dependent. After performing angle-related operations, we can stack the partial images in the local image matrix to generate the depth image, or partially sum them up to produce different image gathers. Several numerical examples are included to demonstrate the applications of this angle-domain image condition.

[1] This Chapter has been published as a journal paper in Geophysics

3.2 INTRODUCTION

Up to present, most seismic processing methods have been based on acoustic-wave migration, which assumes that the Earth is a fluid body and only allows for P-wave propagation. However, the recent progress in multicomponent seismic acquisition and computation power are quickly shifting the seismic practice to process vectorized waves in near-realistic isotropic and anisotropic elastic models. From multicomponent seismic data, both P-P and P-S images can be obtained. P- and S-waves carry different information about the targets, and they may provide estimates of physical properties that cannot be obtained with P-wave data alone. However, more sophisticated imaging techniques are required in order to extract the new information. By neglecting P- and S-wave couplings during migration, some approaches separated the multicomponent data into P- and S-modes and extrapolate them independently with scalar propagators (e.g., Zhe and Greenhalgh, 1997; Sun and McMechan, 2001; Hou and Marfurt, 2002) or elastic propagators (e.g., Xie and Wu, 2005). Other approaches do not separate P- and S-modes on the surface, but extrapolate the entire multicomponent data at once. These techniques include Kirchhoff migration (e.g., Kuo and Dai, 1984; Dai and Kuo, 1986; Hokstad, 2000) and elastic reverse-time migration (RTM) (e.g., Sun and McMechan, 1986; Chang and McMechan, 1987, 1994). Recently, elastic RTM was further explored by some authors (e.g., Yan and Sava, 2008; Lu et al., 2009; Yan and Xie, 2010). Among the existing migration methods, elastic RTM can better preserve both kinematic and dynamic features of elastic waves in complex models, resulting in images that more accurately characterize the subsurface.

One of the important issues in the elastic RTM is the imaging condition. The conventional zero-time-zero-offset cross-correlation imaging condition (Claerbout, 1985) stacks waves coming from all directions. This can effectively suppress the noise but also loses the directional information in the data. In contrast, expanding the image in angle domain, i.e., generating angle-domain partial images, can add an extra dimension to the conventional image. For example, the moveout of the ADCIG carries the phase or travel time errors for waves propagating with different angles through the velocity model. They can be used for migration velocity analysis (MVA). Dynamic information such as amplitude versus angle (AVA) is crucial in reservoir interpretation. However, complex overburden structures often obscure the signals from the reservoir. Extracting AVA from the ADCIG provides an effective way to remove the propagation effect. Imaging in the local angle domain and imaging using elastic waves are essential elements in obtaining high-fidelity subsurface images and reliable petro-physical parameters.

ADCIGs have been extracted in Kirchhoff prestack depth migration (Xu et al., 2001; Brandsberg-Dahl et al., 2003). For wave equation based migration, several techniques have been adopted to extract the ADCIGs. In the source-receiver migration based on double square root equation (e.g., Mosher et al., 1997; Prucha et al., 1999; Mosher and Foster, 2000; Jin et al., 2002), the angle information can be obtained from the wavefield in local wavenumber domain.

For shot profile wave-equation migration, available methods fall into three categories. In the first category, ADCIGs are obtained by first decomposing both source and receiver wavefields into localized beams with different directions, followed by an imaging condition applying to these localized beams around the image point. The ADCIGs can be extracted for either one-way wave equation based methods (Xie and Wu, 2002; Wu and Chen, 2003; Chen et al., 2006) or full-wave equation based RTM (Zhang et al., 2010; and Xu et al., 2011). With this method, the angle decomposition is independent of the image process. The resulted method can be applied to angle-related analyses other than generating ADCIGs, e.g., directional illumination (e.g., Wu et al., 2003; Luo et al., 2004; Wu and Chen, 2002, 2006; Xie et al., 2006; Xie and Yang, 2008; Cao and Wu, 2009b; Mao and Wu, 2010), or resolution and image amplitude compensation (e.g., Xie et al., 2005b; Wu et al., 2006; Cao and Wu, 2009a).

In the second category, ADCIGs are extracted during the imaging stage, where the extended images with space and/or time lags are first calculated. For image with space-shift, the ADCIG can be calculated from offset-CIGs through a slant stack (e.g., Rickett and Sava, 2002; Sava and Fomel, 2003; Biondi and Symes, 2004; Sava and Vasconcelos, 2011; Sava and Vlad, 2011) or a simple radial-trace transform in Fourier domain (Sava and Fomel, 2005a, c). The similar procedure can be applied to time-shift image (Sava and Fomel, 2005b) but for 3-D case a priori information on dip angle is required.

Under the third category, the Poynting vector or the polarization vector of the P-wave is calculated and used to determine the wave propagation direction. Some authors (e.g., Zhang and McMechan, 2011a, b; Yoon et al., 2011) chose to calculate the source wave direction only and focused on the contributions of one or a few most energetic phases. Then, with known reflector dipping angle and assuming mirror reflection (i.e., the reflector is locally planar), the ADCIG is calculated. Others (e.g., Dickens and Winbow, 2011) computed the energy flux directions for both the source and receiver wavefields and extracted angle dependent reflectivity at the imaging point. These methods are computationally efficient and the resulting ADCIGs have good angle resolution.

In this chapter, an angle decomposition method under the first category is developed and applied to the elastic RTM for calculating ADCIG. We first decompose the reconstructed elastic wavefields into local plane waves and use them to calculate the angle-domain partial images. Secondly, we construct the local image matrix (LIM) which is composed of all the angle-domain partial images. LIMs for point scatters and planar reflectors are analyzed. Thirdly, we demonstrate how to apply angle-domain operations in the LIM and convert it into ADCIGs and the depth image. Finally, a five-layer model and the Marmousi2 model are used as examples to demonstrate the feasibility of the approach for generating ADCIGs and depth images.

3.3 WAVEFIELD RECONSTRUCTION

The algorithm of elastic RTM includes the computation of source and receiver wavefields and construction of the image by applying a proper imaging condition. The source wavefields are reconstructed by solving the elastic wave equation with a driving source (Aki and Richards, 1980):

$$\rho \frac{\partial^2 \mathbf{u}(\mathbf{x},t)}{\partial t^2} - \nabla \cdot \sigma(\mathbf{x},t) = \delta(\mathbf{x} - \mathbf{x}_S)\mathbf{s}(t), \tag{3.1}$$

where $\mathbf{s}(t)$ is the source time function, $\mathbf{x}_S$ the source location; $\mathbf{u}(\mathbf{x},t)$ the displacement wavefield, $\sigma(\mathbf{x},t)$ the stress tensor wavefield. In an isotropic medium, the relationship between stress and displacement is

$$\sigma = \lambda \mathbf{I} \nabla \cdot \mathbf{u} + \mu(\nabla \mathbf{u} + \mathbf{u} \nabla), \tag{3.2}$$

where ρ is the density, λ and μ are the Lame's constants, $\mathbf{I}$ is the identity matrix. The receiver wavefields is reconstructed by treating the recorded multicomponent data the boundary condition of the elastic wave equation:

$$\begin{cases} \rho \dfrac{\partial^2 \mathbf{u}(\mathbf{x},t)}{\partial t^2} - \nabla \cdot \sigma(\mathbf{x},t) = 0, \\ \mathbf{u}(\mathbf{x},t)\big|_B = \mathbf{u}_0(\mathbf{x},t), \end{cases} \tag{3.3}$$

where $\mathbf{u}_0(\mathbf{x},t)$ is the multicomponent seismic data recorded at the receiving surface B. Note that the above boundary condition is valid only for a plane surface.

Otherwise, a complete boundary condition including both displacement and stress may be required.

3.4 MODE SEPARATION AND ANGLE DECOMPOSITION

In the elastic RTM scenario, the reconstructed wavefields are vectorized and P- and S-modes are coupled. The image formed by direct cross-correlation of source and receiver wavefields mixes the contributions from both P- and S-waves and is difficult to interpret. To get images with clear physical meaning, it is preferred to separate P- and S-modes, and implement the imaging condition as cross-correlation of pure wave modes. In an isotropic medium, mode separation can be achieved in space domain (Sun et al., 2001; Yan and Sava, 2008) or wavenumber domain (Dellinger and Etgen, 1990; Zhang and McMechan, 2010). The space-domain divergence and curl can separate a mixed-mode wavefield into P- and S-waves but introduce distortions to the separated wavefields (Sun et al., 2001). On the contrary, the wavenumber- or slowness-domain separation preserves the waveforms of the original wavefield. Given a propagation direction θ at an image location, P-wave polarization is parallel to it while S-wave polarization is perpendicular to it; P- and S-waves can be separated by projecting the displacement to the two polarization directions. To build an angle-domain imaging condition, both P- and S-modes need to be decomposed into superposition of local plane waves (or beams) propagating in different directions. Local slant stacking (Xie and Lay, 1994; Xie et al., 2005a, Xie and Yang; Yan and Xie, 2009; 2010) is adopted to extract local plane P- and S-waves propagating along direction θ in frequency domain:

$$\mathbf{u}^P(\theta,\mathbf{x},\omega)=\omega p_P\int W\left(\mathbf{x}'-\mathbf{x}\right)\hat{\mathbf{e}}\cdot\left[\mathbf{u}\left(\mathbf{x}',\omega\right)\cdot\hat{\mathbf{e}}\right]\cdot e^{-i\omega\left(\mathbf{x}'-\mathbf{x}\right)\cdot\mathbf{p}_P}d\mathbf{x}', \tag{3.4}$$

$$\mathbf{u}^S(\theta,\mathbf{x},\omega)=\omega p_S\int W\left(\mathbf{x}'-\mathbf{x}\right)\hat{\mathbf{e}}\times\left[\mathbf{u}\left(\mathbf{x}',\omega\right)\times\hat{\mathbf{e}}\right]\cdot e^{-i\omega\left(\mathbf{x}'-\mathbf{x}\right)\cdot\mathbf{p}_S}d\mathbf{x}', \tag{3.5}$$

where $W\left(\mathbf{x}'-\mathbf{x}\right)$ is a window function centered at $\mathbf{x}$; $\mathbf{u}^P\left(\theta,\mathbf{x},\omega\right)$ and $\mathbf{u}^S\left(\theta,\mathbf{x},\omega\right)$ are the local plane P- and S-waves. $\mathbf{p}_P=\hat{\mathbf{e}}/\overline{v}_P$ and $\mathbf{p}_S=\hat{\mathbf{e}}/\overline{v}_S$ are the P- and S-wave slowness vectors which satisfy the dispersion relations; where $\overline{v}_P$ and $\overline{v}_S$ are average P and S wave velocities in the sampling window W; and $\hat{\mathbf{e}}$ is the unit vector specifying the propagation direction of the plane wave. ωp_P and ωp_S are the Jacobian coefficients from slowness domain to angle domain.

As an example, we demonstrate the results of slowness analysis in an elastic model. Shown in Figure 3.1 is a snapshot of the receiver-side wavefield overlapped on a five-layer velocity model with its parameters listed in Table 3.2. On the top and bottom of the figure are samples of slowness analyses at selected locations indicated in the wavefield. For this convergent wavefield, the slowness vectors, i.e., the vectors from the origin of the polar coordinate to these energy peaks, reveal the wave propagation directions and their slowness. Following the dispersion relations within the sampling window W, all P-wave peaks fall on the inner circle with a radius of $1/\overline{v}_P$ and all S-wave peaks fall on the outer circle with a radius of $1/\overline{v}_S$. These results demonstrate that the directional information can be fully extracted by the angle decomposition along the dispersion circles.

3.5 ANGLE-DOMAIN IMAGING CONDITION

Similar to acoustic imaging condition, the image for elastic waves can be expressed as the convolution between the incident (source side) and scattered (receiver side) P- and S-waves, i.e.,

$$I^{PP}(\mathbf{x}) = \sum_{\omega} u_s^P(\mathbf{x},\omega) \cdot \left[u_g^P(\mathbf{x},\omega) \right]^*, \tag{3.6}$$

and

$$I^{PS}(\mathbf{x}) = \sum_{\omega} u_s^P(\mathbf{x},\omega) \cdot \left[u_g^S(\mathbf{x},\omega) \right]^*, \tag{3.7}$$

where I is the depth image; scalar u is the complex amplitudes of the wavefields; superscripts P and S denote the wave types and subscripts s and g denote the source and receiver waves. To obtain the angle-domain imaging condition, we substitute equations 3.4-3.5 into equations 3.6-3.7 and obtain

$$I^{PP}(\mathbf{x}) = \sum_{\theta_s} \sum_{\theta_g} I^{PP}(\theta_s, \theta_g, \mathbf{x}), \tag{3.8}$$

and

$$I^{PS}(\mathbf{x}) = \sum_{\theta_s} \sum_{\theta_g} I^{PS}(\theta_s, \theta_g, \mathbf{x}), \tag{3.9}$$

where

$$I^{PP}(\theta_s, \theta_g, \mathbf{x}) = \sum_{\omega} \left[\hat{\mathbf{e}}_s^P \cdot \mathbf{u}_s^P(\theta_s, \mathbf{x}, \omega) \right] \left[\hat{\mathbf{e}}_g^P \cdot \mathbf{u}_g^P(\theta_g, \mathbf{x}, \omega) \right]^*, \tag{3.10}$$

$$I^{PS}(\theta_s, \theta_g, \mathbf{x}) = \sum_{\omega} \left[\hat{\mathbf{e}}_s^P \cdot \mathbf{u}_s^P(\theta_s, \mathbf{x}, \omega) \right] \left[\hat{\mathbf{e}}_g^S \times \mathbf{u}_g^S(\theta_g, \mathbf{x}, \omega) \cdot \hat{\mathbf{e}}_n \right]^*, \tag{3.11}$$

are angle-domain partial images for P-P and P-S scatterings, $\mathbf{u}_s^P$, $\mathbf{u}_g^P$ and $\mathbf{u}_g^S$ are all local plane P- and S-waves. $\hat{\mathbf{e}}_s^P$, $\hat{\mathbf{e}}_g^P$ and $\hat{\mathbf{e}}_g^S$ are unit vectors indicating their propagation directions; θ_s and θ_g are incident and scattering angles, respectively. $\hat{\mathbf{e}}_n$ is the normal vector perpendicular to the propagation plane in which $\hat{\mathbf{e}}_s^P$ and $\hat{\mathbf{e}}_g^S$ are lying.

3.6 LOCAL IMAGE MATRIX

Given the image point $\mathbf{x}$, we can organize all the partial images in equation 3.8 or 3.9 into a matrix according to their incident and scattering angles. This matrix is called local image matrix (LIM) (e.g., Xie and Wu, 2002; Wu and Chen, 2003). Many important features regarding the velocity models, reflector properties and acquisition geometry can be revealed by investigating the LIM. We will explore some of these features using numerical examples.

3.6.1 Local image matrix for point scatterers

We investigate LIMs for point scatterers having perturbations of different elastic parameters. Without losing generality, consider a z-direction P-wave incident on scatters with three different types of perturbations: density ρ, and Lame's constants λ and μ. The interaction of incident wave and perturbation generate scattered waves which are illustrated in Figures 3.2a to 3.2c. Different perturbations lead to different radiation patterns which are listed in Table 3.1 (Wu, 1985). The perturbation $\delta\lambda$ generates only scattered P-wave, while the perturbation $\delta\rho$ or $\delta\mu$ generate both scattered P- and S-waves. We record scattered P- and S-waves from all directions and back propagate them to calculate the LIMs of these scatters. The related P-P LIMs are shown in Figures 3.2d to 3.2f, and P-S LIMs are shown in Figures 3.2g to 3.2i. In each LIM, the partial images of these scatterers form a common incident angle strip in the LIM at zero degree (i.e., z-direction). The patterns of the image vividly reveal the radiation patterns from different types of perturbations. For a scatterer composed of perturbations $\delta\rho$, $\delta\lambda$ and $\delta\mu$, its radiation pattern will be the combination of three basic patterns, and the resultant LIM will be the linear combination of the basic LIMs shown in Figure 3.2. This will be useful in investigating diffraction points (Zhu and Wu, 2010) or detecting scattering properties of a fractured reservoir (Zheng et al., 2011).

3.6.2 Local image matrix for planar reflectors

A planar reflector can be considered as a line of continuous scatterers. The scattered waves from all scatterers interfere with each other, forming a reflected wave propagating in a direction dictated by Snell's law. The sketch in Figure 3.3a illustrates the process by which an incident wave along θ_s generates a scattered wave along θ_g at a locally planar reflector. Figure 3.3b and 3.3c are the corresponding P-P and P-S LIMs, where the horizontal and vertical axes are incident and scattering angles, and the main (from upper left to lower right) and secondary (from upper right to lower left) diagonals are reflection and dipping angle axes. For the P-P reflection, the coordinate transform can be expressed as (e.g., Xie and Wu, 2002)

$$\theta_d = \left(\theta_s + \theta_g\right)/2\,, \tag{3.12}$$

and

$$\theta_r = \left(\theta_s - \theta_g\right)/2 \, . \tag{3.13}$$

For the P-S reflection, the coordinate transform is (e.g., Yan and Xie, 2010)

$$\theta_d = \tan^{-1}\frac{\overline{v}_S \sin\theta_s + \overline{v}_P \sin\theta_g}{\overline{v}_S \cos\theta_s + \overline{v}_P \cos\theta_g}, \tag{3.14}$$

and

$$\theta_r = \theta_s - \theta_d \, . \tag{3.15}$$

where θ_d is the target dipping angle and θ_r is the reflection angle defined as the incident angle relative to the reflector normal. Due to different reflection angles for P- and S-waves, the reflection angle axis in the P-S LIM is curved with the curvature depends on $\overline{v}_P$ to $\overline{v}_S$ ratio. In the P-S LIM, there are two shadow zones in which the incident P-wave and scattered S-wave cannot satisfy Snell's law. With these transforms, the LIM can be written as a function of dipping and reflection angles instead of incident and scattering angles.

We use the same five-layer model as used in the previous section to demonstrate the relationship between the local reflector geometries and the energy distributions in the LIMs. Shown in the middle of Figure 3.4 is the velocity model, in which locations A to D are selected to calculate the LIMs. The model is illuminated by 24 sources and 300 fixed receivers, both covering the entire surface of the model. The LIMs in the top row are for P-P image. At point A, the shape of the reflector is severely away from a planar interface and the image is largely generated by diffracted waves from broad directions. In this context it is similar to a point scatter. In the related LIM, the energy is distributed over a broad area. Point B is located on a dipping planar interface. To satisfy Snell′s law, the energy is distributed along a strip. Its intersection with the dipping axis gives a dipping angle of approximately 15°, which agrees well with the reflector geometry. The extension of the strip along the reflection axis reveals the illumination coverage at the target. Point C is located on a dipping reflector with slight curvature. The energy distribution in the LIM indicates that the local dip is about 30°. Because of the steep dip angle, the local acquisition aperture is relatively small. Thus, the energy distribution has limited extension along reflection axis and the illumination to this point is relatively poor. Point D is located on a horizontal interface. The energy is distributed at zero dip and, due to being located at a great depth, spans a relatively narrow reflection angle compared to that for point B. The bottom row shows LIMs for P-S image. The energy distributions in these LIMs follow the curvature of reflection angle axis. They reveal the same dip information as in P-P LIMs but have slightly different reflection-angle coverage. Note, in P-S LIMs, the P-S conversion is zero at normal incidence, where the sign of images reverses.

3.7 ANGLE-DOMAIN OPERATIONS ON LOCAL IMAGE MATRIX

LIM keeps all angle-related information and is localized in space. It is convenient to apply various angle domain operations in the LIM. For example, we can conduct acquisition aperture compensation, illumination correction, or eliminate unwanted signals in the LIM (Yan and Xie, 2009, 2010). We can also extract useful angle-related information, e.g., the local AVA or migration residual moveout, from the LIM. These operations can be designed to be highly flexible, e.g., target oriented, dip angle dependent or reflection angle dependent. Here, as examples, we introduce some operations in the LIM to improve the P-P and P-S depth images.

3.7.1 Extracting angle-domain common image gathers

For a planar reflector, energy is located along a strip in LIM where Snell's law is satisfied (see, e.g., b1-d1 and b2-d2 in Figure 3.4). Summing up the energy along the common reflection-angle direction will produce the angle-domain common image gathers (ADCIGs).

$$I^{PP}\left(\theta_r, \mathbf{x}\right) = \sum_{\theta_d} I^{PP}\left(\theta_r, \theta_d, \mathbf{x}\right), \tag{3.16}$$

$$I^{PS}\left(\theta_r, \mathbf{x}\right) = \sum_{\theta_d} I^{PS}\left(\theta_r, \theta_d, \mathbf{x}\right). \tag{3.17}$$

If the local dip of the reflector can be acquired from some prior information, e.g., from the migrated image, ADCIG can be directly picked from the LIM at θ_d = reflector dip angle.

3.7.2 Eliminating spurious artifacts in P-P image

In Figure 3.4, some weak energy appears along reflection angles $\pm\pi/2$ for P-P LIM at point A. They are generated by forward-propagated and back-propagated head waves, diving waves and backscattered waves (Yoon et al., 2004). At the image location, these waves meet at nearly parallel but opposite directions. In a long range, these signals will spuriously correlate and appear as low-wavenumber artifacts in RTM image.

Here we introduce an angle-domain filter in the LIM to block the very wide-angle energy from entering the image. The resulted angle-domain imaging condition can be expressed as

$$I^{PP}(\mathbf{x}) = \sum_{\theta_r}\sum_{\theta_d} M^{PP}(\theta_r,\theta_d) I^{PP}(\theta_r,\theta_d,\mathbf{x}), \tag{3.18}$$

where $M^{PP}(\theta_r,\theta_d)$ is designed to attenuate events with very wide reflection angles. For example, we can choose to eliminate all the energy with reflection angles larger than certain values from the LIM.

3.7.3 Correcting polarity reversal in P-S image

The P-S image usually does not involve artifacts as those appear in the P-P image. However, polarity reversals occur because S-wave changes its polarity when crossing the normal incidence (Balch and Erdemir, 1994) (see, e.g., a2-d2 in Figure 3.4). The polarities must be corrected, otherwise destructive interference will occur when summing up the partial images into the final image (Lu et al., 2010; Yan and Xie, 2010). Because the polarity of P-S image is controlled by the reflection angles, it is natural to conduct this correction in the LIM. Thus we apply an angle-domain operator to the P-S partial images

$$I^{PS}(\mathbf{x}) = \sum_{\theta_r}\sum_{\theta_d} M^{PS}(\theta_r,\theta_d) I^{PS}(\theta_r,\theta_d,\mathbf{x}), \tag{3.19}$$

where

$$M^{PS}(\theta_r,\theta_d) = \begin{cases} 1 & \theta_r > 0 \\ 0 & \theta_r = 0 \\ -1 & \theta_r < 0 \end{cases} \tag{3.20}$$

is an reflection-angle dependent operator for correcting the polarity.

3.8 NUMERICAL EXAMPLES

We use two examples to demonstrate the calculations of angle gathers and migration images. The first example is the five-layer model used in the previous section. The synthetic dataset is generated using 26 explosion sources and 300 receivers both covering the entire surface of the model. The space between the sources is 0.24 km and the interval between the receivers is 0.024 km. The source time function is a 15 Hz Ricker wavelet. A fourth-order elastic finite difference code is used to extrapolate the source and receiver wavefields. Figures 3.5, 3.6 and 3.7 are P-P and P-S ADCIGs obtained from the true velocity model, and models with +10% and -10% velocity errors. These ADCIGs are calculated at nine horizontal locations from 0.6 km to 5.4 km at an interval of 0.6 km and range between -60° and 60°. The polarity of P-S gathers has been corrected. The flat gathers in Figure 3.5 are from the true velocity model. The gathers that curve down are from the fast model, while the gathers that curve up are from the slow model. The actual angular span depends on the effective acquisition aperture and, in general, decreases with increasing depth. For the sections of reflectors where steep dip angles are involved, the angular span is smaller because of the reduced effective acquisition aperture. Given the acquisition geometry, P-S gathers usually have wider angle coverage compared to the P-P image. Figure 3.8a and 3.8b are the corresponding P-P and P-S images after applying the angle-domain operators, i.e., equation 3.18 and 3.19, respectively. The two images are quite clean and consistent. Due to its shorter wavelength, the P-S image has higher resolution than the P-P image.

Next we test our techniques on the Marmousi2 model (Martin et al., 2002). The P- and S-wave velocities and the density are illustrated in Figure 3.9. The synthetic dataset is modeled using 111 surface sources which are located between distances 3.0 km and 14.0 km at an interval of 0.1 km. The source time function is a 30 Hz Ricker wavelet. Receivers are located on the seafloor and spaced 0.0125 km apart. For each shot, 361 bilateral receivers are switched on to record the reflection signals. Shown in Figure 3.10 and 3.11 are P-P and P-S angle gathers extracted from the dataset. These angle gathers are calculated at 17 vertical lines starting from distance 4.5 km with an interval of 0.5 km. The angle range is -68°-68°. The P-S gathers appear sharper than the P-P gathers because they involve shorter wavelength. Since the correct velocity model is used, the common image gathers are generally flat, except at some steep reflectors where the P-S gathers are a little twisted. Due to limited acquisition aperture and existing velocity gradient, the steep reflectors are mostly illuminated by near normal incident P-waves. Because the P-S conversion is inefficient at small reflection angles, the P-S gathers are usually weaker for steep dip reflectors. Figure 3.12a and 3.12b compare the P-P images before and after applying the angle-domain filter. Due to wide angle reflections, the P-P image without angle filter is masked by strong artifacts, especially at the shallow regions. With angle-domain imaging condition, the artifacts are effectively removed, while the images of the interfaces are well kept. Shown in Figure 3.13a is the P-S image without applying the angle-domain operator, where some partial images from different shots cancel each other out, causing the blurring of the image. After polarization correction, the image in Figure 3.13b is greatly enhanced.

3.9 DISCUSSIONS

To extract the angle related information from the wavefield, both the integral method (e.g., slant stack or windowed FFT) and differential method (e.g., calculate the Poynting vector or displacement vector) can be used. The former is more stable but relatively time consuming and the latter is more efficient but may encounter unstable result in a complicated wavefield.

To properly conduct angle decomposition, choosing correct window size, shape and sampling rate are crucial. According to uncertainty principle, there is always a tradeoff between the space and angle resolution. A larger sampling window improves the angle accuracy but makes the result less localized in space, and vice versa. We choose the window size that is one to two wavelengths at the dominant frequency. Within this range, a complex wave front can be decomposed into a superposition of local plane waves and their propagation directions can be properly determined. Different window sizes are used for P- and S-modes due to their different wavelengths. To avoid the numerical aliasing caused by coarse sampling, we choose a sampling rate about twice per minimum wavelength. In all examples presented here, we use simple rectangular windows. Though quite simple, it yields better angle resolution compared to window functions with edge tapers, such as the Gaussian window.

We compare the efficiency of our method with conventional local slant stacking and windowed FFT method. Conventional local slant stacking is implemented in the entire slowness/wavenumber space. The slant stack along the dispersion circles can save tremendous computations and it is usually one to two orders of magnitude faster. In addition, the proposed method directly generates angle components while windowed FFT outputs wavenumber components, followed by a conversion from wavenumber to angle. To output finely sampled angle components, zero padding around the spatial window is usually required by the windowed FFT but not required by the local slant stacking. Even though FFT is a fast algorithm, enlarging the window size will considerably raise its computational cost. On the other hand, increase the number of directions will lower the efficiency of our method, but will not affect the windowed FFT method. In general, the efficiencies of the local slant stacking along the dispersion circle and the windowed FFT methods are comparable and are dependent on the detailed treatments. Zhang et al. (2010) and Xu et al. (2011) extensively discussed methods to improve the efficiency of the windowed FFT method.

3.10 CONCLUSIONS

For elastic RTM, we present a slowness-based method to decompose the P- and S-waves into angle components and formulate the angle-domain partial image as the cross-correlation of the decomposed local plane waves. Collecting all the angle-domain partial images, we construct the LIMs for both P-P and P-S images. LIM is a convenient tool for investigating the angle related problems in wave propagation and imaging. Sorting the energy in LIM can generate different ADCIGs which can be used for velocity, amplitude and illumination analyses. The target is not necessarily locally planar as required by other methods. For point scatters, their radiation patterns in the LIM are related to the material properties of elastic perturbations. For a locally planar reflector, the incident and scattered waves are controlled by Snell's law. In the P-P LIM, the energy forms a strip, and for the P-S image the energy forms a curved strip because reflection angles are different for incident and scattered waves. Summing up energy in the LIM produces the depth image. Angle-related operations, e.g., eliminating the unwanted artifacts, correcting for acquisition aperture effect or polarization effect, can be conveniently performed in LIM and lead to ADCIGs or migration images with improved quality. To validate our method, both P-P and P-S angle gathers and images are computed for the synthetic datasets generated from a five-layer elastic model and the elastic Marmousi2 model. The current technique can be extended to 3D isotropic and anisotropic cases.

3.11 REFRENCES

Aki, K., and P.G. Richards, 1980, Quantitative seismology: Theory and methods, W. H. Freeman and Co.

Balch, A., and C. Erdemir, 1994, Sign-change correction for prestack migration of p-s converted wave reflections: Geophysical Prospecting, 42, 637–663.

Biondi, B., and W. Symes, 2004, Angle-domain common-image gathers for migration velocity analysis by wavefield continuation imaging: Geophysics, 69, 1283-1298.

Brandsberg-Dahl, S., M. V. De Hoop, and B. Ursin, 2003, Focusing in dip and AVA compensation on scattering-angle/azimuth common image gathers: Geophysics, 68, 232–254.

Cao, J., and R.S. Wu, 2009a, Fast acquisition aperture correction in prestack depth migration using beamlet decomposition: Geophysics, 74, S67-S74.

———, 2009b, Full-wave directional illumination analysis in the frequency domain: Geophysics, 74, S85-S93.

Chang, W. F, and G. A. McMechan, 1987, Elastic reverse-time migration: Geophysics, 52, 1365-1375.

Chang, W. F, and G. A. McMechan, 1994, 3D elastic prestack, reverse-time depth migration: Geophysics, 59, 597-609.

Claerbout, J. F., 1985, Imaging the Earth's Interior: Blackwell Scientific Publications.

Dai, T. F., and J. T. Kuo, 1986, Real data results of Kirchhoff elastic wave migration: Geophysics, 51, 1006–1011.

Dellinger, J., and J. Etgen, 1990, Wave-field separation in two-dimensional anisotropic media: Geophysics, 55, 914-919.

Dickens, A., and Winbow G. A., 2011, RTM angle gathers using Poynting vectors: 81st Annual International Meeting, SEG, Expanded Abstracts.

Hokstad, K., 2000, Multicomponent Kirchhoff migration: Geophysics, 65, 861–873.

Hou, A., and K. Marfurt, 2002, Multicomponent prestack depth migration by scalar wavefield extrapolation: Geophysics, 67, 1886–1894.

Kuo, J. T., and T. F. Dai, 1984, Kirchhoff elastic wave migration for the case of noncoincident source and receiver: Geophysics, 49, 1223–1238.

Lu, R., P. Traynin, and J. E. Anderson, 2009, Comparison of elastic and acoustic reverse-time migration on the synthetic elastic Marmousi-II OBC dataset: 79th Annual International Meeting, SEG, Expanded Abstracts, 28, 2799-2803.

Lu, R., J. Yan, J. E. Anderson, and T, Dickens, 2010, Elastic RTM: anisotropic wave-mode separation and converted-wave polarization correction: 80th Annual International Meeting, SEG, Expanded Abstracts, 3171-3175.

Luo, M. Q., J. Cao, X. B. Xie, and R. S. Wu, 2004, Comparison of illumination analysis using one-way and full-wave propagators: 74th Annual International Meeting, SEG, Expanded Abstracts, 67–70.

Jin. S. W., C. Mosher and R. S. Wu, 2002, Offset-domain pseudoscreen prestack depth migration: Geophysics, 67, 1895–1902.

Martin, G. S., K. J. Marfurt, and S. Larsen, 2002, Marmousi-2: An updated model for the investigation of AVO in structurally complex areas: 72nd Annual International Meeting, SEG, Expanded Abstracts, 1979-1982.

Mao, J., R. S. Wu and J. H. Gao, 2010, Directional illumination analysis using the local exponential beamlet, Geophysics, 75, S163-S174.

Mosher, C. C., D. J. Foster, and S. Hassanzadeh, 1997, Common angle imaging with offset plane waves: 67th Annual International Meeting, SEG, Expanded Abstracts, 1379–1382.

Mosher, C. C., and D. Foster, 2000, Common angle imaging conditions for prestack depth migration: 70th Annual International Meeting, SEG, Expanded Abstracts, 830–833.

Prucha, M., B. Biondi, B., and W. Symes, 1999, Angle-domain common image gathers by wave-equation migration: 69th Annual International Meeting, SEG, Expanded Abstract, 824-827.

Rickett, J. E., and P. C. Sava, 2002, Offset and angle-domain common image-point gathers for shot-profile migration: Geophysics, 67, 883-889.

Sava, P., and S. Fomel, 2003, Angle-domain common image gathers by wavefield continuation methods: Geophysics, 68, 1065-1074.

Sava, P., and S. Fomel, 2005a, Coordinate-independent angle-gathers for wave equation migration: 75th Annual International Meeting, SEG, Expanded Abstracts, 2052-2055.

———, 2005b, Time-shift imaging condition: 75th Annual International Meeting, SEG, Expanded Abstracts, 1850-1853.

———, 2005c, Wave-equation common angle gathers for converted waves: 75th Annual International Meeting, SEG, Expanded Abstracts, 947-950.

Sava, P., and I. Vasconcelos, 2011, Extended imaging condition for wave-equation migration: Geophysical Prospecting, 59, 35–55.

Sava, P., and I. Vlad, 2011, Wide-azimuth angle gathers for wave-equation migration: Geophysics, 76, S131–S141.

Sun, R., and G. A. McMechan, 1986, Pre-stack reverse-time migration for elastic waves with application to synthetic offset vertical seismic profiles: Proceedings of the IEEE, 74, no. 3, 457-465.

———, 2001, Scalar reverse-time depth migration of prestack elastic seismic data: Geophysics, 66, 1519–1527.

Sun, R., J. Chow, and K. J. Chen, 2001, Phase correction in separating P- and S-waves in elastic data: Geophysics, 66, 1515-1518.

Wu, R..S., and K. Aki, 1985, Scattering characteristics of elastic waves by an elastic heterogeneity: Geophysics, 50, 582-595.

Wu, R. S., and L. Chen, 2002, Mapping directional illumination and acquisition aperture efficacy by beamlet propagators: 72nd Annual International Meeting, SEG, Expanded Abstracts, 1352-1355.

———, 2003, Prestack depth migration in angle-domain using beamlet decomposition: Local image matrix and local AVA: 73rd Annual International Meeting, SEG, Expanded Abstracts, 973–976.

———, 2006, Directional illumination analysis using beamlet decomposition and propagation: Geophysics, 71, S147–S159.

Wu, R. S., L. Chen, and X. B. Xie, 2003, Directional illumination and acquisition dip-response: 65th Conference and Exhibition, EAGE, Extended Abstracts, P147.

Wu, R. S., X. B. Xie, M. Fehler and L.J. Huang, 2006, Resolution analysis of seismic imaging: 68th Annual International Meeting, EAGE, Expanded Abstracts, G048.

Xie, X. B., and T. Lay, 1994, The excitation of explosion Lg, a finite-difference investigation: Bull. Seism. Soc. Am., 84, 324-342.

Xie, X. B., and R. S. Wu, 2002, Extracting angle domain information from migrated wavefields: 72nd Annual International Meeting, SEG, Expanded Abstracts, 1360-1363.

Xie, X. B., and R. S. Wu, 2005, Multicomponent prestack depth migration using elastic screen method: Geophysics, 70, S30-S37.

Xie, X. B., Z. Ge, and T. Lay, 2005a, Investigating explosion source energy partitioning and Lg-wave excitation using a finite-difference plus slowness analysis method: Bull. Seism. Soc. Am., 95, 2412-2427.

Xie, X. B., R. S. Wu, M. Fehler and L. Huang, 2005b, Seismic resolution and illumination: A wave-equation-based analysis, 75th Annual International Meeting, SEG, Expanded Abstracts, 1862-1865.

Xie, X. B., S. W. Jin, and R. S. Wu, 2006, Wave-equation-based seismic illumination analysis: Geophysics, 71, S169–S177.

Xie, X. B., and H. Yang, 2008, A full-wave equation based seismic illumination analysis methods: 70th Conference and Exhibition, EAGE, Extended Abstract, P284.

Xu, S., H. Chauris, G. Lambare, and M. Noble, 2001, Common-angle migration: A strategy for imaging complex media: Geophysics, 66, 1877–1894.

Xu, S., Y. Zhang, and B. Tang, 2011, 3D common image gathers from reverse time migration: Geophysics, 76, S77–S92.

Yan, J., and P. Sava, 2008, Isotropic angle-domain elastic reverse-time migration: Geophysics, 73, S229-S239.

Yan, R., and X. B. Xie, 2009, A new angle-domain imaging condition for reverse time migration: 79th Annual International Meeting, SEG, Expanded Abstracts, 2784-2788.

Yan, R., and X. B. Xie, 2010, A new angle-domain imaging condition for elastic reverse time migration: 80th Annual International Meeting, SEG, Expanded Abstracts, 3181-3186.

Yoon, K., K. Marfurt, and E. W. Starr, 2004, Challenges in reverse-time migration: 74th Annual International Meeting, SEG, Expanded Abstracts, 1057–1060.

Yoon, K., M. Guo, J. Cai, and B. Wang, 2011, 3D RTM angle gathers from source wave propagation direction and dip of reflector: 81th Annual International Meeting, SEG, Expanded Abstracts, 3136-3139.

Zhang, Q. and G. A. McMechan, 2010, 2D and 3D elastic wavefield vector decomposition in the wavenumber-domain for VTI media: Geophysics, 75, D13-D26.

Zhang, Q. and G. A. McMechan, 2011a, Direct vector-field method to obtain angle-domain common-image gathers for isotropic acoustic and elastic reverse-time migration: Geophysics, 76, WB135-WB149.

Zhang, Q. and G. A. McMechan, 2011b, Common-image gathers in the incident phase-angle domain from reverse time migration in 2D elastic VTI media: Geophysics, 76, S197-S206.

Zhang, Y., S. Xu, B. Tang, B. Bai, Y. Huang and T. Huang, 2010, Angle gathers from reverse time migration: The Leading Edge, 29, 1364 – 1371.

Zhe, J., and S. A. Greenhalgh, 1997, Prestack multicomponent migration: Geophysics, 62, 598–613.

Zheng, Y., X. Fang, M. Fehler and D. Burns, 2011, Double-beam stacking to infer seismic properties of fractured reservoirs: 81th Annual International Meeting, SEG, Expanded Abstracts, 1809-1813.

Zhu, X., and R.S. Wu, 2010, Imaging diffraction points using the local image matrices generated in prestack migration: Geophysics, 75, S1-S9.

3.12 FIGURES AND TABLES

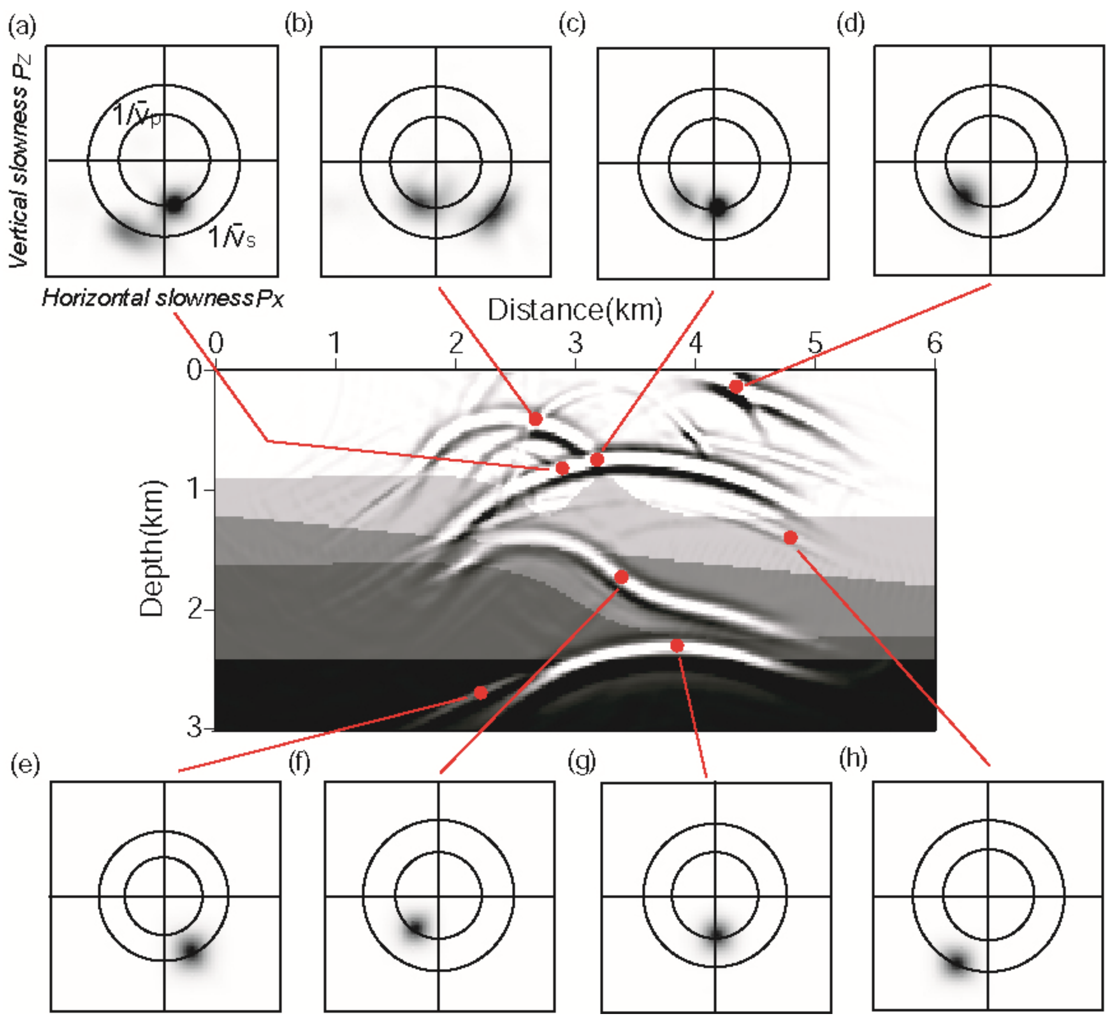

Figure 3.1 Slowness analyses performed for the receiver side wavefield in a five-layer model. In the center is the velocity model superimposed by the vertical-component wavefield at $t = T - 0.85s$, where T is the total recording time. (a)- (h) are slowness domain energy distributions at selected locations indicated in the model.

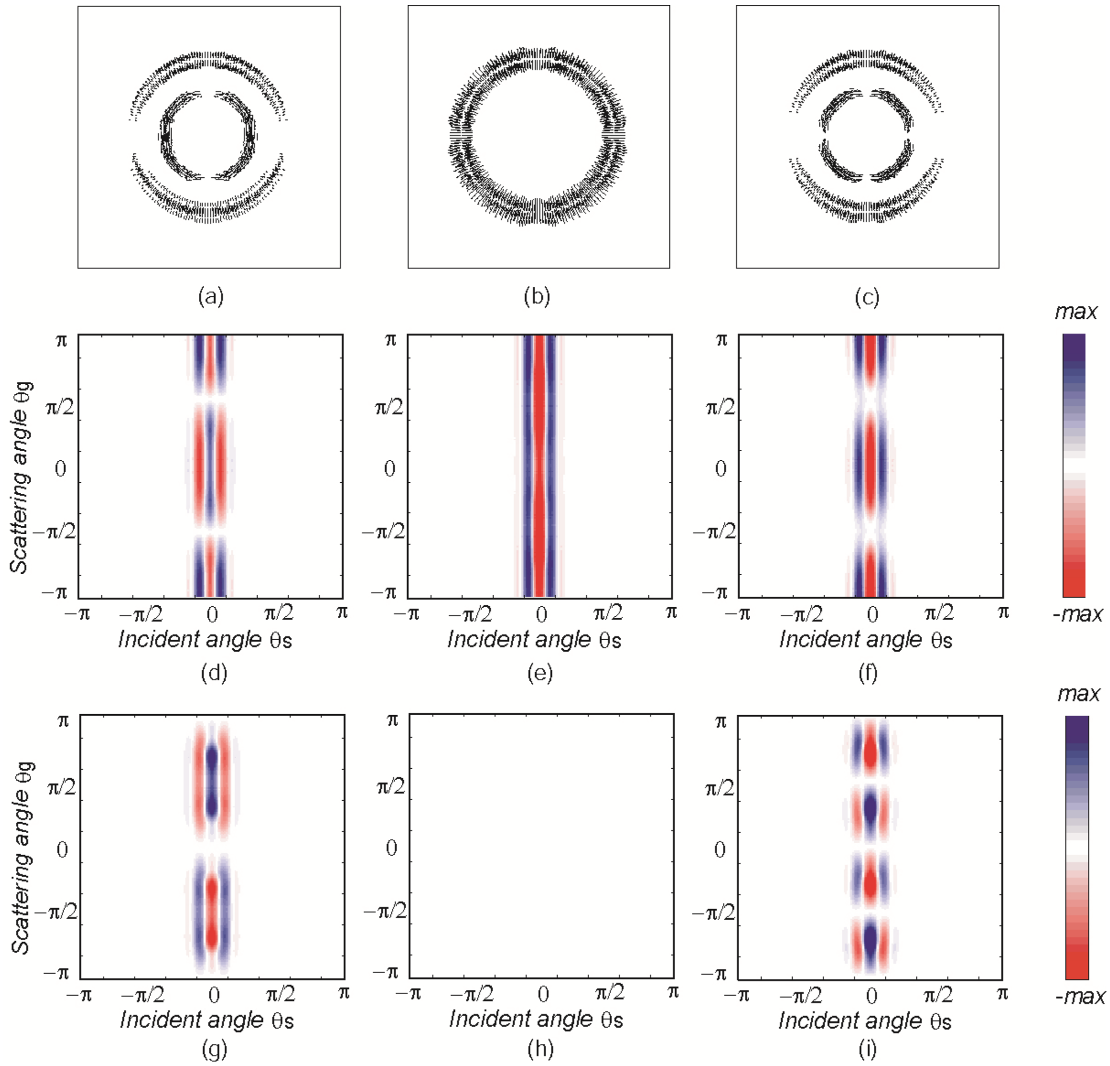

Figure 3.2 Local image matrices for point scatters with different elastic parameter perturbations, left column: density ρ, middle column: Lame's constant λ, and right column: shear modulus μ. (a), (b) and (c) are their vectorized displacements of the scattered waves. (d), (e) and (f) are P-P LIMs, and (g), (h) and (i) are P-S LIMs.

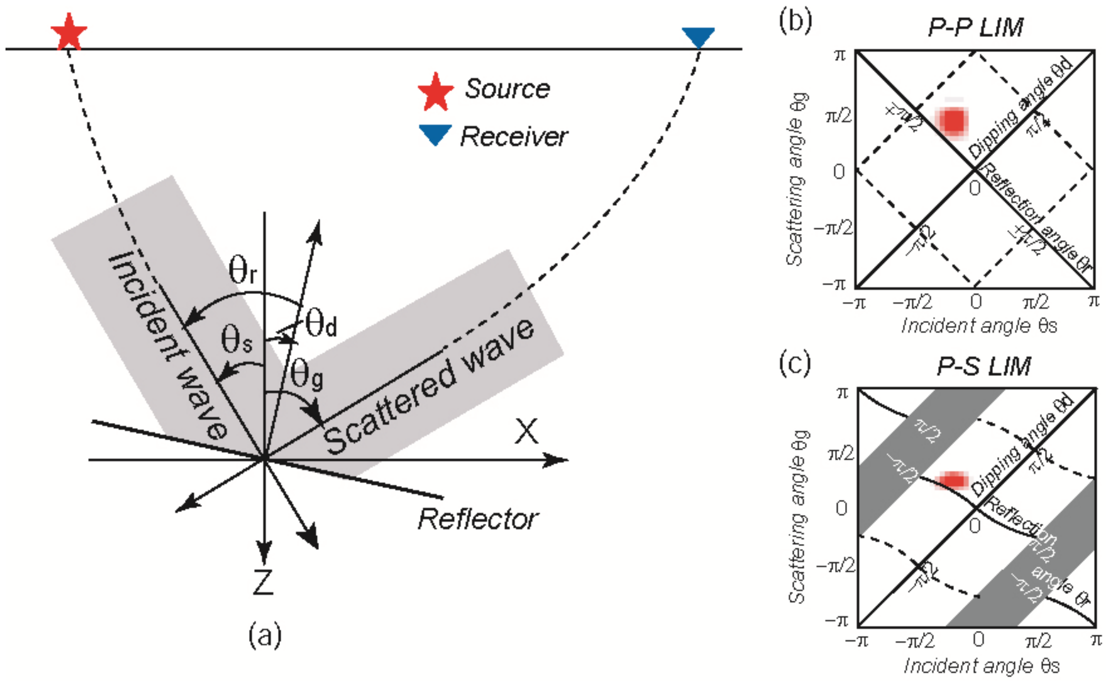

Figure 3.3 Sketches showing the structure of LIMs. (a) Coordinate system used in local angle-domain analysis, where θ_s and θ_g are incident and scattering angles and θ_r and θ_d are reflection and target dipping angles. (b) and (c) are structures of the P-P and P-S LIMs. Note that the red dots are energy distributions of the related reflection events.

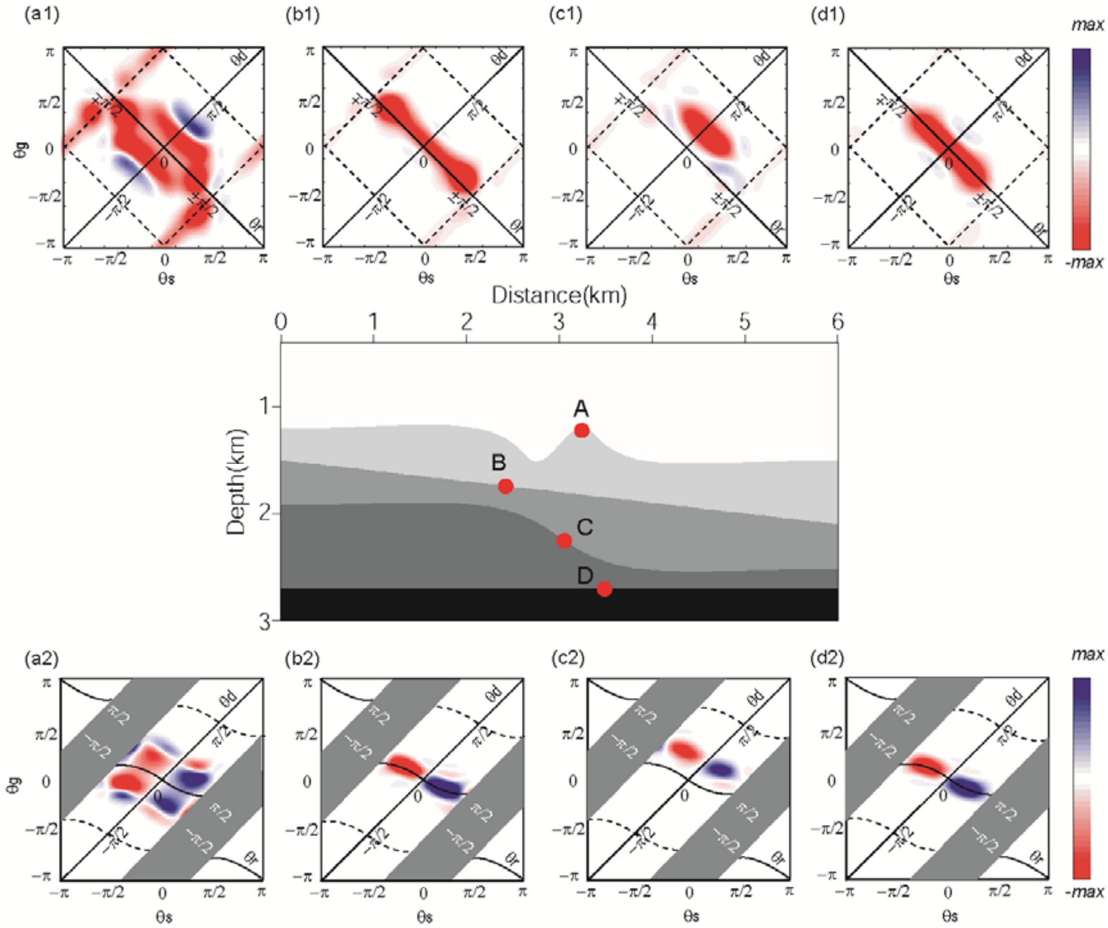

Figure 3.4 Samples of LIMs at selected locations in a five-layer model. The center is the velocity model. (a1) - (d1) are P-P LIMs and (a2) - (d2) are corresponding P-S LIMs. For coordinate systems in the LIM, refer to Figure 3.2.

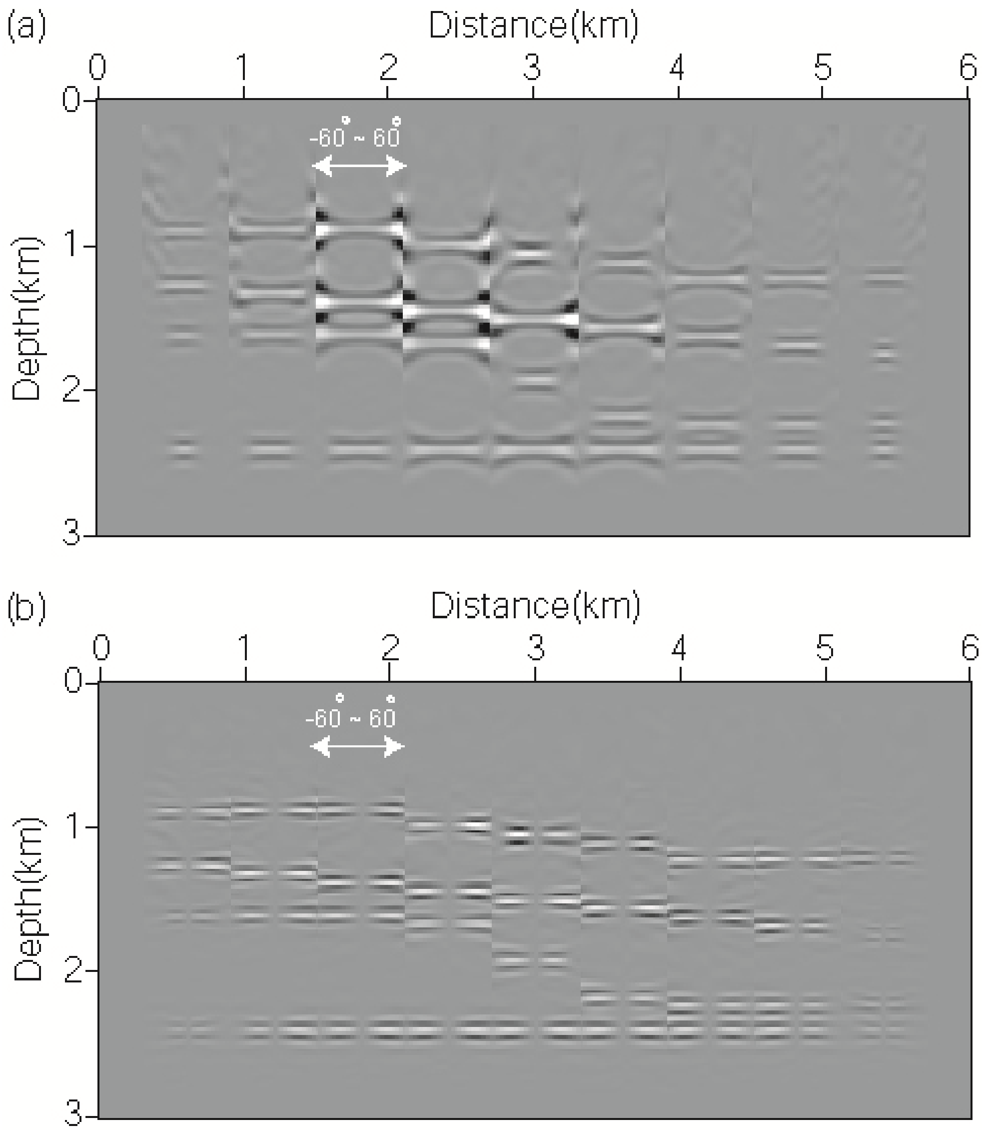

Figure 3.5 The ADCIGs for (a) P-P and (b) P-S reflections from the true velocity model. The angle range is -60°-60°.

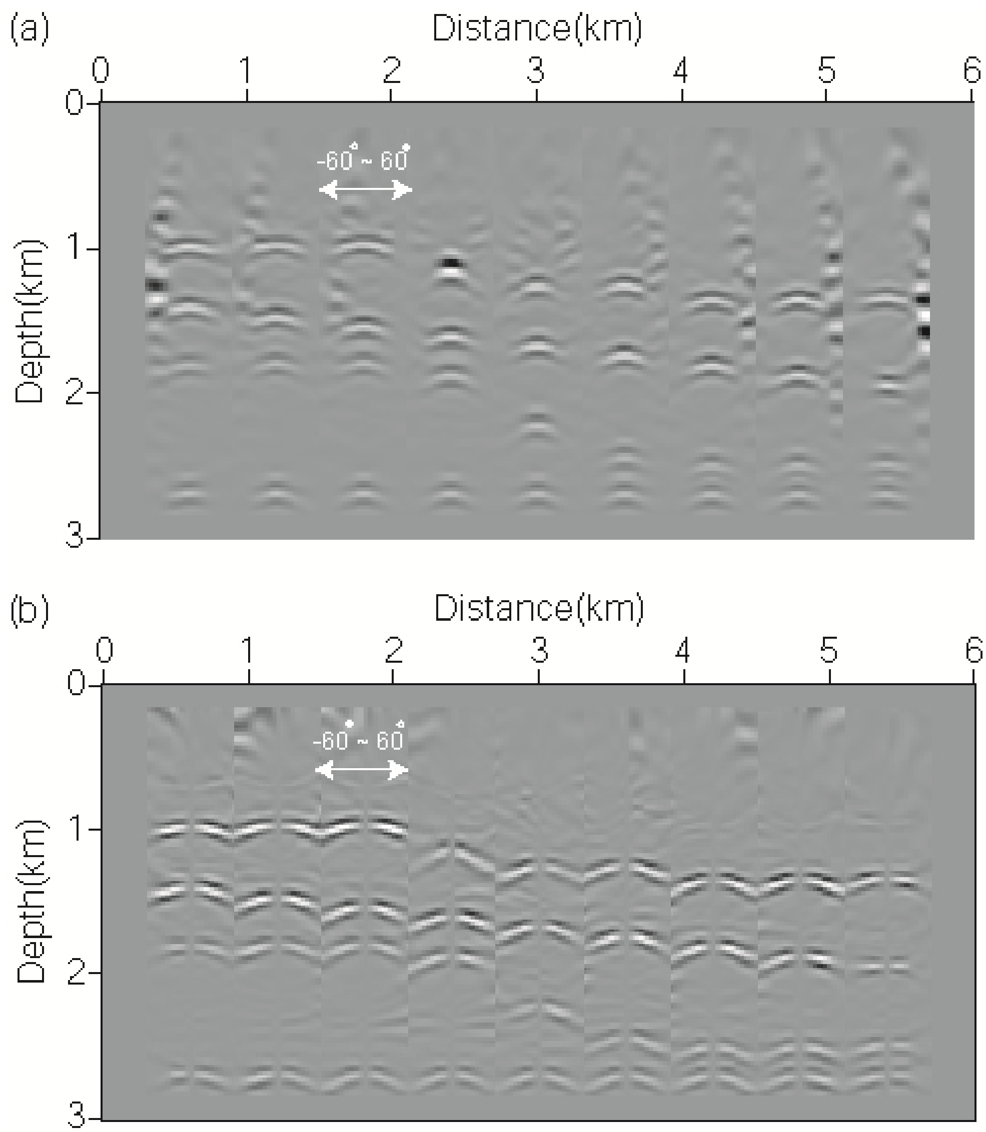

Figure 3.6 Similar to Figure 3.5, except the velocity model has +10% errors.

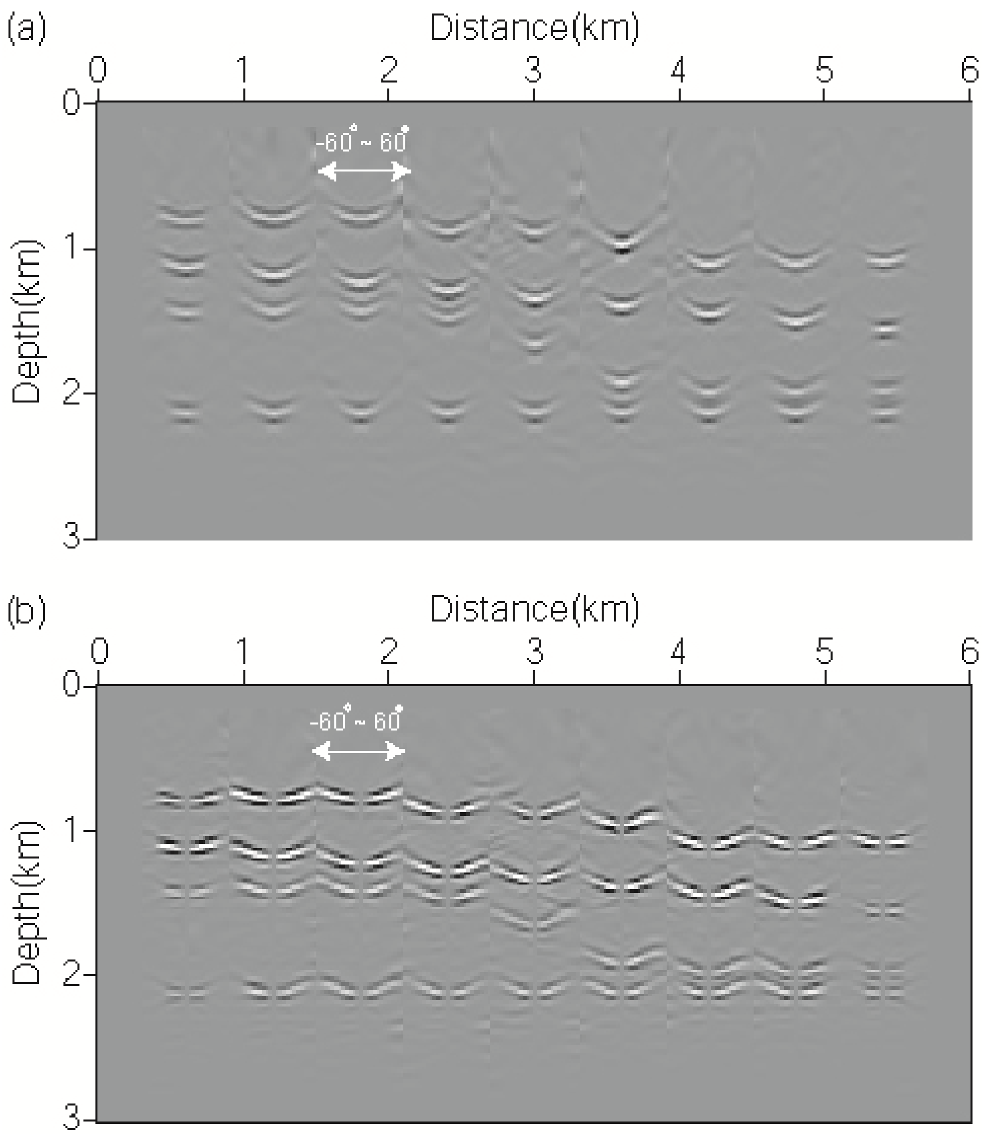

Figure 3.7 Similar to Figure 3.5, except the velocity model has -10% errors.

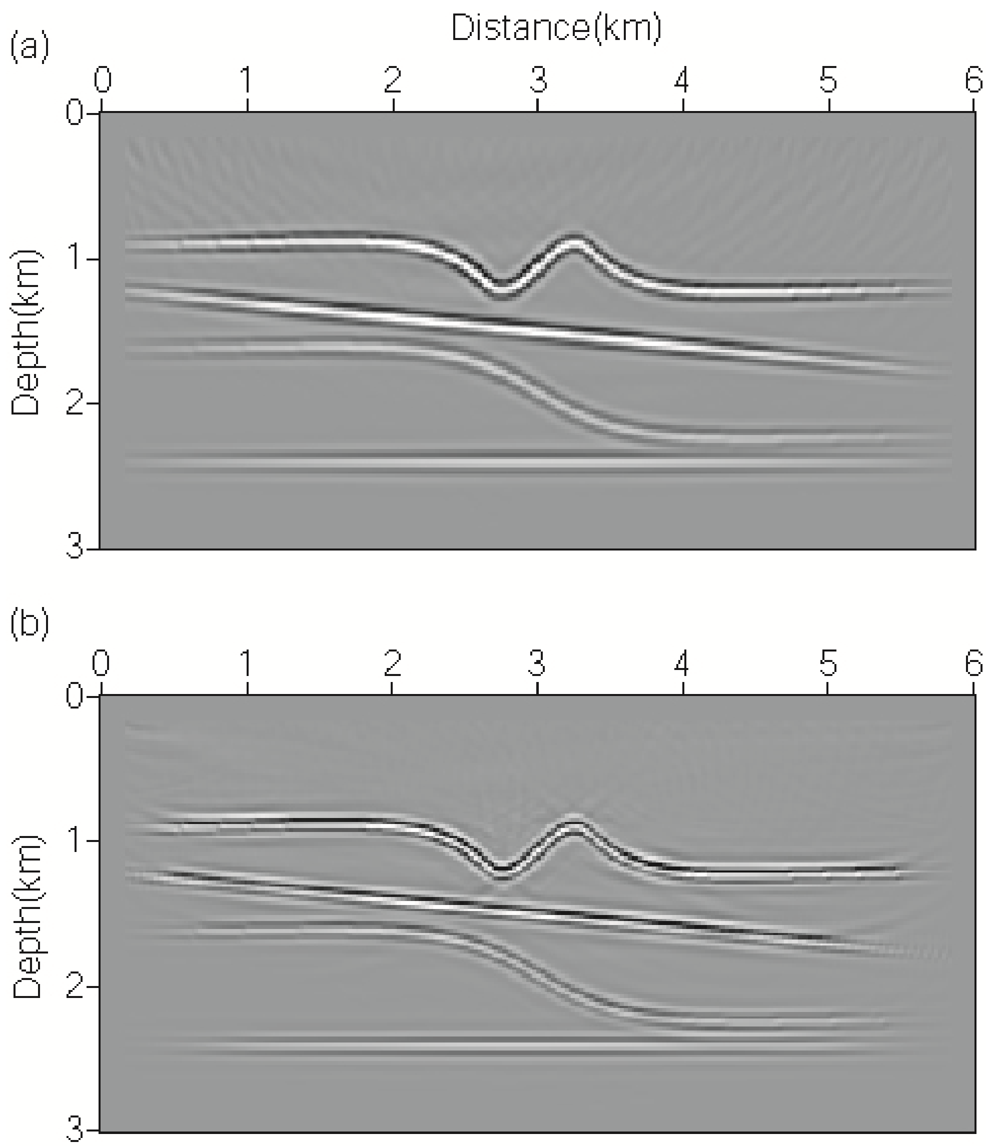

Figure 3.8 The migration images for the five-layer model, where (a) and (b) are for P-P and P-S images, respectively. Note, for the P-P image, the wide-angle artifacts has been removed by eliminating the energy with reflection angles larger than 60 degrees from the LIM, and for the P-S image, the polarization reversal has been corrected in the LIM.

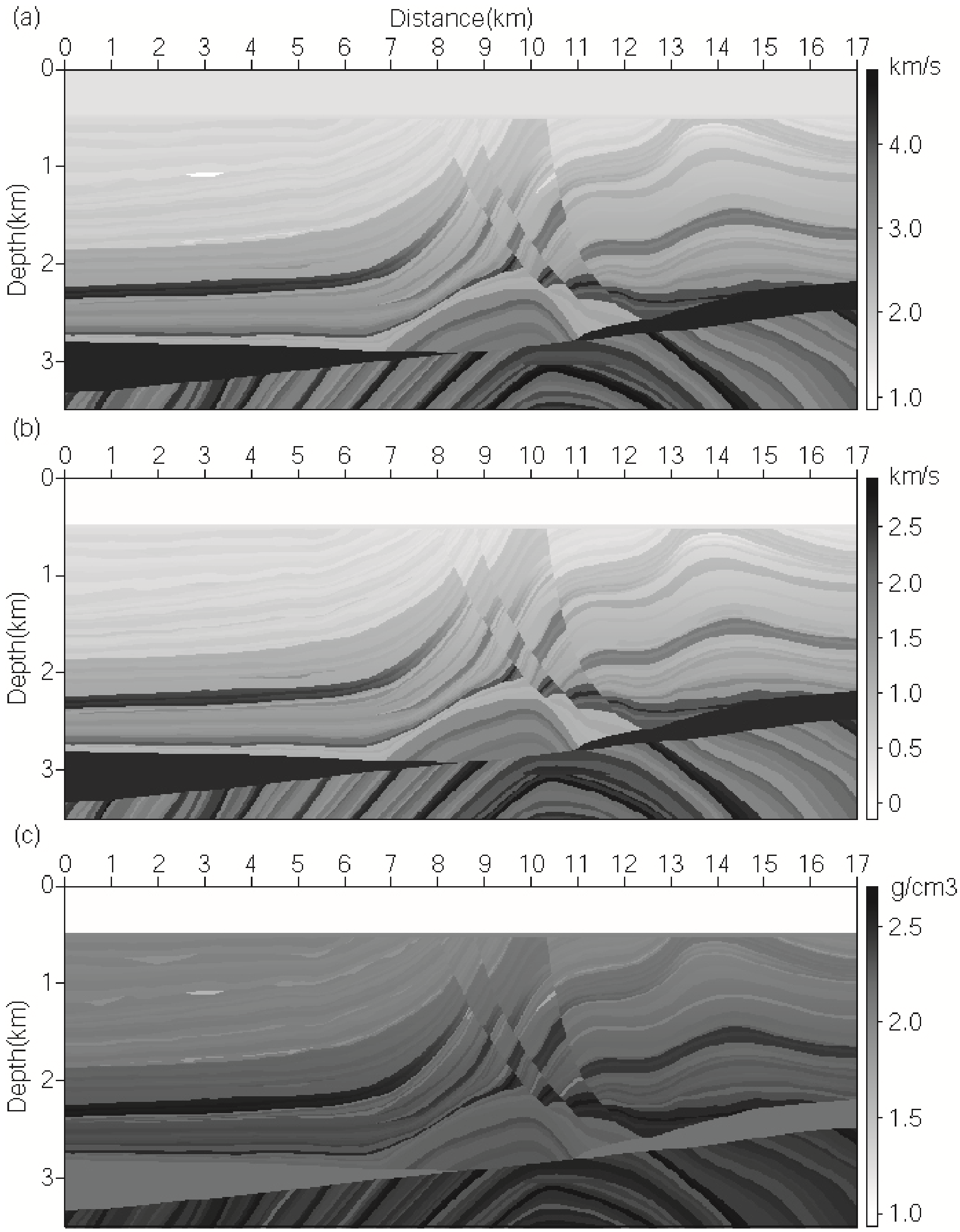

Figure 3.9 The elastic Marmousi2 model, with (a) P-wave velocity, (b) S-wave velocity and (c) density.

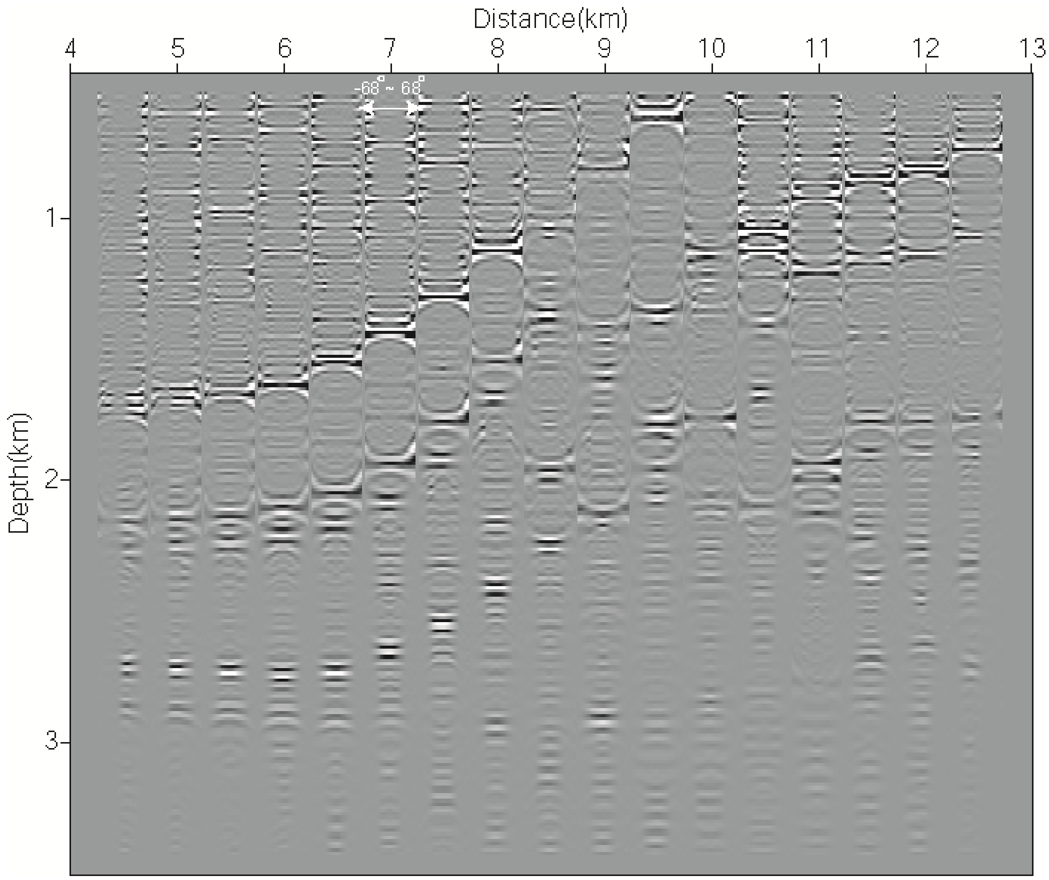

Figure 3.10 The P-P ADCIGs extracted from Marmousi2 model. The angle range is -68°-68°.

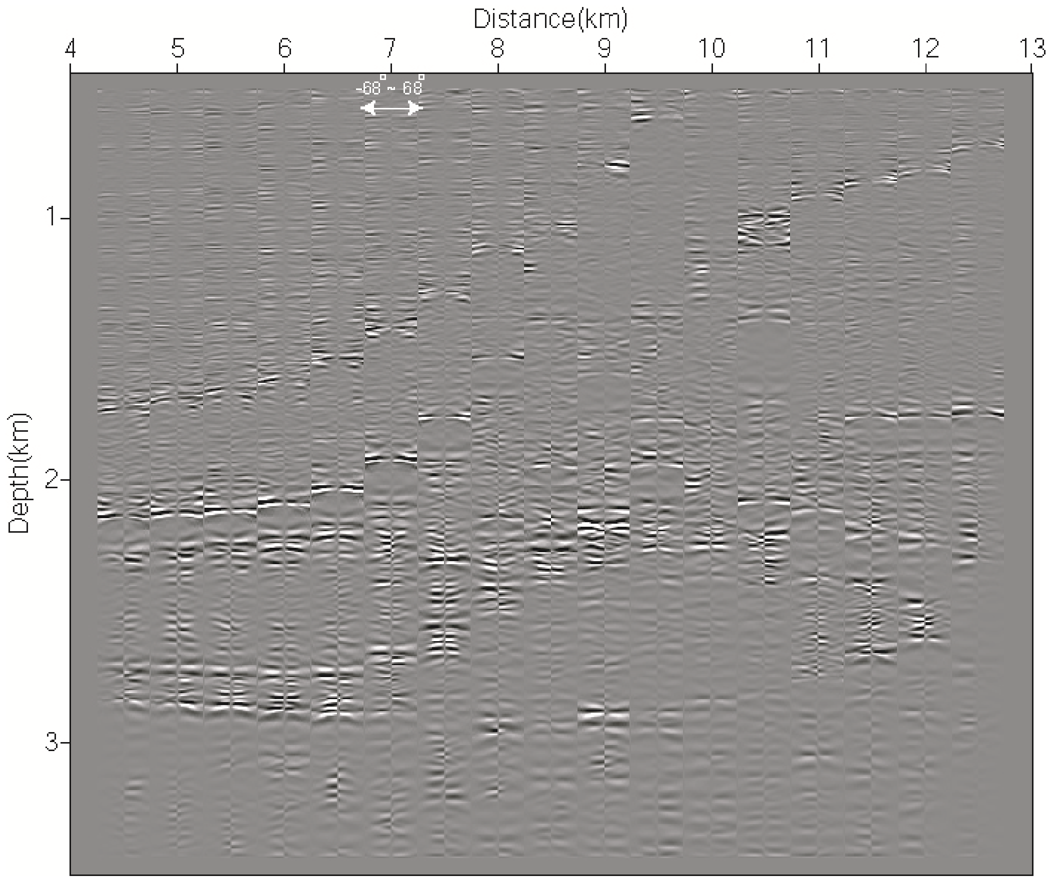

Figure 3.11 Similar to Figure 3.10, except for the P-S image.

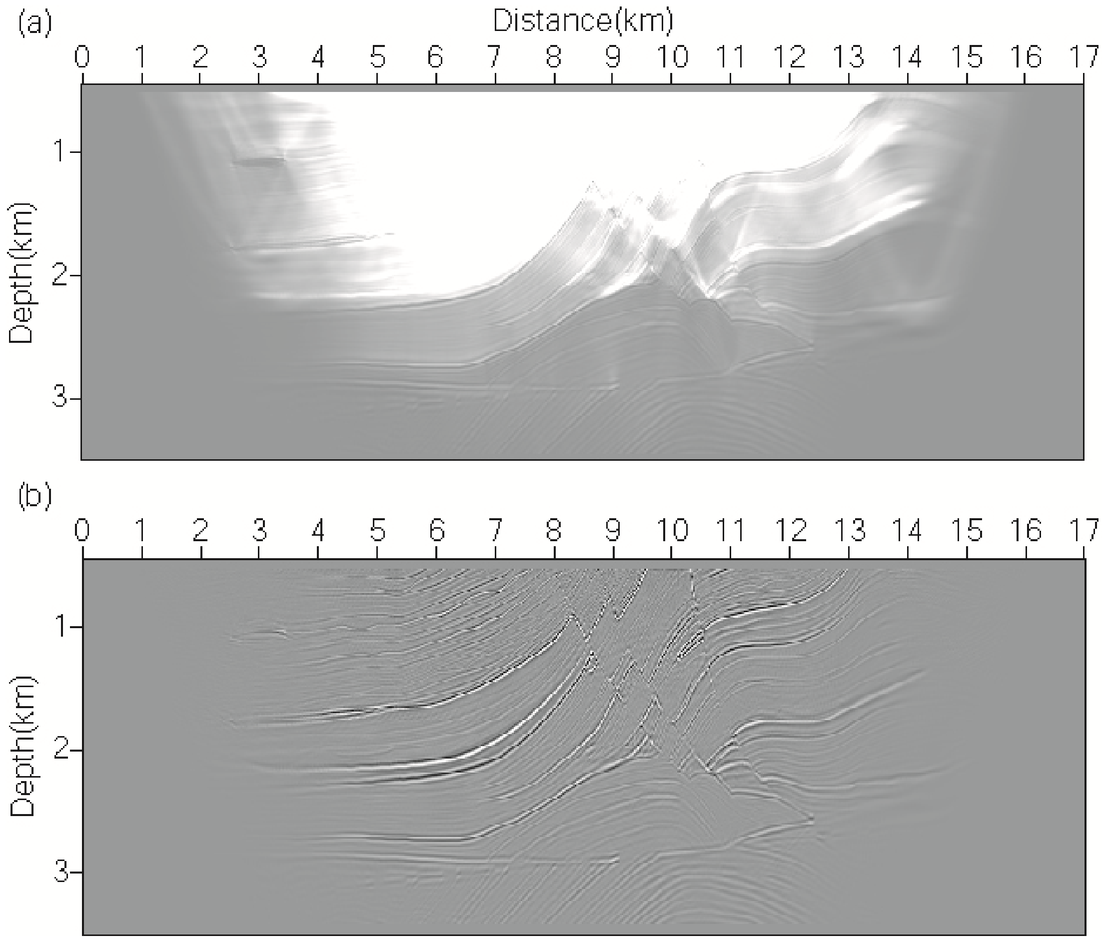

Figure 3.12 Comparison of migrated P-P images for Marmousi2 model, where (a) is the image before applying the angle-domain operator and (b) is the image where reflections with angle larger than 68 degrees have been eliminated.

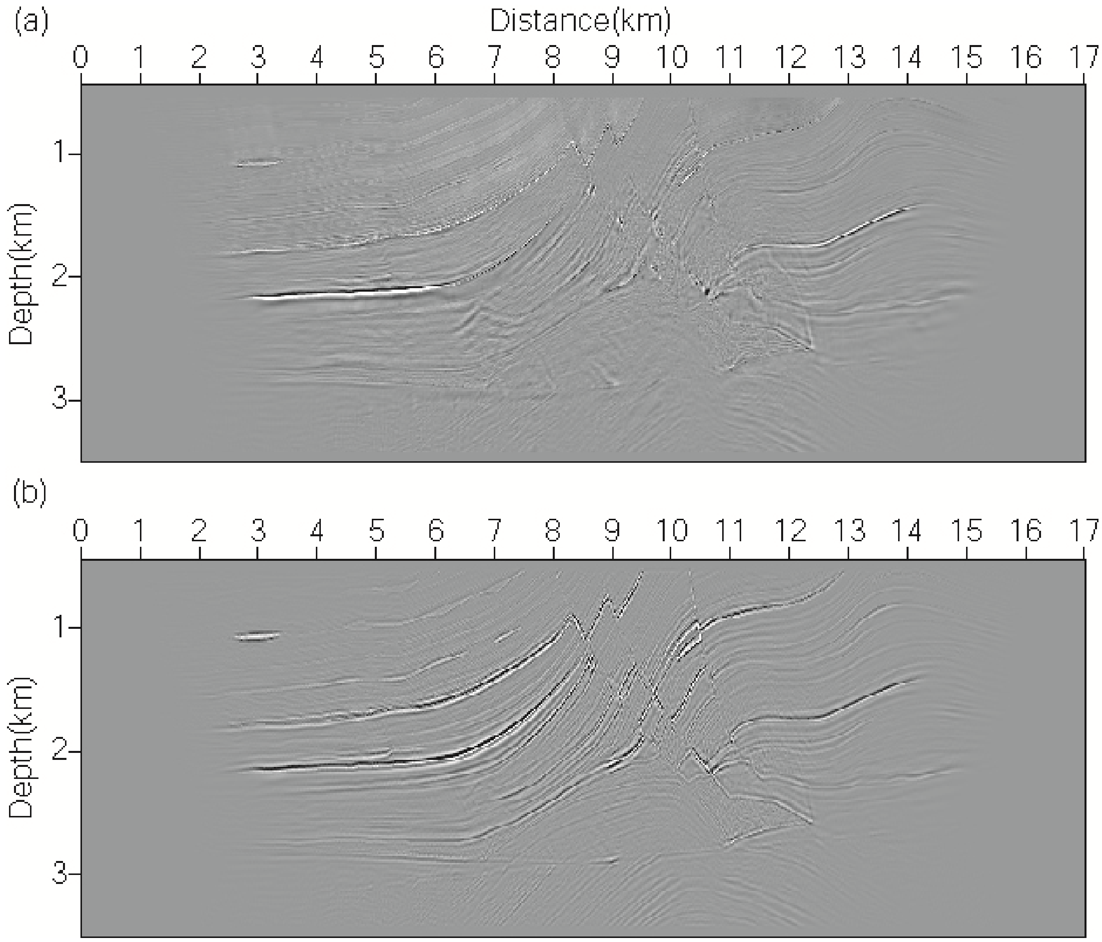

Figure 3.13 Similar to Figure 3.12, except it is for P-S image. Note that in (b), the polarization reversal has been corrected from the LIM.

Table 1 The radiation patterns of scattered P- and S-waves due to perturbations of different elastic parameters.

Perturbations	$\delta\rho$	$\delta\lambda$	$\delta\mu$
P-P scattering	$\cos\theta \cdot \frac{\delta\rho}{\rho_0}$	$-1 \cdot \frac{\delta\lambda}{\lambda_0}$	$-(1+\cos 2\theta) \cdot \frac{\delta\mu}{\mu_0}$
P-S scattering	$\sin\theta \cdot \frac{\delta\rho}{\rho_0}$	$0 \cdot \frac{\delta\lambda}{\lambda_0}$	$\sin 2\theta \cdot \frac{\delta\mu}{\mu_0}$

θ: the scattering angle relative to the incident direction.

ρ_0 : the background density.

λ_0 : the background Lame's first parameters.

μ_0 : the background shear modulus.

Table 2 The P and S-wave velocities and density of the model.

Layer	P velocity km/s	S velocity km/s	Density g/cm^3
1	3.50	2.00	2.00
2	3.70	2.12	2.04
3	4.00	2.30	2.10
4	4.20	2.42	2.14
5	4.50	2.60	2.20

4 AVA ANALYSIS BASED ON TRUE-AMPLITUDE RTM ANGLE-DOMAIN COMMON IMAGE GATHER[2]

4.1 SUMMARY

We propose a new method to extract true-amplitude angle-domain common image gather (ADCIG) for amplitude versus angle (AVA) analysis. The source and receiver wavefields are migrated into the target regions using accurate full-wave propagator and are decomposed into angle components along all directions to construct the local image matrix (LIM). Target illumination matrix relates LIM to local medium parameters. It accounts for the propagation effects and acquisition footprint. LIM is related to local medium parameters with target illumination. It can be formulated with the angle components of the background Green's function and accounts for the propagation effects and acquisition footprint. ADCIG and reflection-angle-dependent illumination are extracted from LIM and target illumination matrix. Normalized by the corresponding illumination, ADCIG becomes true-amplitude and gives the correct AVA information. To avoid the full-scale wavefield decomposition, we measure the angle information of the seismic event before the application of the imaging condition. The multi-frequency wavefields and dominant-frequency Green's functions on the source and receiver-side are projected to the incident and scattering angle directions using local slant stacking and further form ADCIG and target illumination. AVA response can be retrieved from true-amplitude ADCIG is further analyzed in cross-

[2] This Chapter will be submitted to Geophysics

plot domain. A simple layered reservoir model is used to demonstrate the accuracy of AVA calculation. Another reservoir model illustrates that the subsequent AVA analysis in the cross-plot panel can effectively separate reservoir from background reflections.

4.2 INTRODUCTION

Dynamic information about the wavefields such as AVO/AVA (amplitude versus offset or angle) analysis is crucial in geological interpretation of reservoirs. The traditional procedure of AVO analysis is to examine the amplitude versus offset directly from the offset domain surface seismic data, followed by time-dependent mapping from offset to incident angle (e.g., Chiburis, 1984; Ostrander, 1984; Castagna and Backus, 1993; Yilmaz, 2001). The subsequent AVO analysis is based primarily on differences between AVO/AVA observations in reservoir and non-reservoir locations at the target depth. It works well in regions where the overburden stratigraphic structure is relatively flat, but does not in areas with dips or strong lateral variations. AVA analysis based on the prestack depth migration has the advantage that the measurement is applied to the migrated wavefield right at the target depth. Thus the propagation effect caused by the complex overburden structure can be removed through the back propagation. The new technique has the great potential to replace the traditional AVO techniques. The structure complexities are better accounted during migration, providing greater confidence to locate the correct position of AVA anomalies (Mosher et al., 1996).

The basic requirement of AVA analysis is that the migration must be true amplitude. Many attempts have been made to develop a true-amplitude propagator for both ray-based migration (e.g., Bleistein et al., 1987; Hubral et al., 1991; Hanitzsch, 1995; Xu et al., 2001; Audebert et al., 2002; Brandsberg-Dahl et al., 2003) and the wave-equation based migration (OWEM) (e.g., Ursin, 1983; Zhang et al., 2003, 2005; Wu and Cao, 2005; Cao and Wu, 2008). The use of correct full wave equation, not an approximation, gives RTM greater amplitude fidelity than OWEM or ray-based migration. Hence it can be considered as the superior choice in quantitative AVA analysis. In addition to the true-amplitude propagator, the imaging condition must be dynamically correct. Cross-correlation of source and receiver wavefields is a stable imaging condition, but cannot provide image amplitude consistent with true reflectivity. The cross-correlation normalized by source illumination (Claerbout, 1971) is preferred for the sake of true amplitude. Many authors (e.g., Valenciano and Biondi, 2003; Guitton, 2007; Chattopadhyay and McMechan, 2008) have investigated this imaging condition. However, Wu et al. (2004) pointed out the importance of aperture coverage in affecting the image amplitude. The source illumination only compensates the geometric spreading and transmission lost on the source side. If the acquisition aperture is limited, the transmission loss on the receiver side cannot be compensated during migration and needs to be taken account in the imaging condition as well. To implement this imaging condition, many studies (Wu et al., 2004; Wu and Luo, 2005; Jin et al., 2006; Cao and Wu, 2009; Mao and Wu, 2010) have been published.

To retrieve the AVA behavior of the reflections, the most crucial step is to extract the directional information from the full wavefields generated by RTM. A variety of techniques have been proposed for this purpose and they mainly fall into three categories. In the first category, the source and receiver wavefields are decomposed into localized beams along all the possible directions, followed by the application of the imaging condition to every combination of them (Xie and Wu, 2002; Wu and Chen, 2003). Anti-leakage FFT and local slant stacking (e.g., Xie and Yang, 2008; Yang et al., 2008; Zhang et al., 2010; Xu et al., 2011; Yan and Xie, 2012) have been proposed for the RTM wavefield decomposition. In the second category, subsurface offset gathers are formed by the extended imaging condition with space and/or time lags and then are transformed into angle domain (Sava and Fomel, 2003, 2006). Some researchers (e.g., Zhang et al., 2007; Vyas et al., 2010; Sava and Vasconcelos, 2011) have practiced this method in the framework of RTM. Under the third category, the energy flux direction or the polarization direction of P-wave is computed and is considered as the wave propagation direction (e.g., Yoon et al, 2004; Zhang and McMechan, 2011).

In this chapter, we describe the workflow of AVA analysis based on true-amplitude ADCIG extracted in the scheme of RTM. First, we develop the theory to retrieve the true-amplitude ADCIG by removing the propagation and acquisition effects which are accounted in the target illumination. Second, we measure the incident angle and dip angle and use them as the prior information in the computation of ADCIG and target illumination. Normalizing ADCIG with target illumination will result in AVA responses. Third, we represent AVA responses in the crossplot of intercept and gradient. Fourth, two numerical experiments are used to demonstrate the AVA results extracted from subsurface image.

4.3 THEORY

Since the Earth is composed of elastic medium, AVA depends on the elastic parameters of upper and lower medium separated by the interface. Here we target at the AVA feature of P-P reflection. Without losing accuracy, only the pressure component of the seismic data is migrated to the target region using a scalar RTM propagator.

4.3.1 Imaging condition

The subsurface image is formed as the cross-correlation between the forward and backward propagating wavefields reconstructed by RTM

$$I(\mathbf{x};\mathbf{x}_s) = \sum_{\omega} u_s(\mathbf{x};\mathbf{x}_s,\omega)\cdot\left[u_g(\mathbf{x};\mathbf{x}_s,\omega)\right]^*, \tag{4.1}$$

where

$$u_s(\mathbf{x};\mathbf{x}_s,\omega) = f(\omega)G(\mathbf{x};\mathbf{x}_s,\omega), \tag{4.2}$$

is the forward propagating wavefields generated from shot location $\mathbf{x}_s$, and

$$u_g(\mathbf{x};\mathbf{x}_s,\omega) = \sum_{\mathbf{x}_g} D(\mathbf{x}_g;\mathbf{x}_s,\omega)\frac{\partial G^*(\mathbf{x};\mathbf{x}_g,\omega)}{\partial n}, \tag{4.3}$$

is the backward propagating wavefields from all the geophones related to shot location $\mathbf{x}_s$; where $s(\omega)$ is the spectrum of source wavelet; $G(\mathbf{x};\mathbf{x}_s,\omega)$ is the Green's function generated from the shot location $\mathbf{x}_s$; $G(\mathbf{x};\mathbf{x}_g,\omega)$ is the Green's function generated from the geophone location $\mathbf{x}_g$; $\partial/\partial n$ is the gradient relative to the normal direction of the recording surface; $D(\mathbf{x}_g;\mathbf{x}_s,\omega)$ is the seismic signal which travels from the shot $\mathbf{x}_s$ to the target and then reflected back to the geophone located at $\mathbf{x}_g$:

$$D(\mathbf{x}_g;\mathbf{x}_s,\omega) = s(\omega)\sum_{\theta_s}\sum_{\theta_g}\sum_{\mathbf{x}'} G(\theta_s,\mathbf{x}';\mathbf{x}_s,\omega) M(\theta_s,\theta_g,\mathbf{x}') G(\theta_g,\mathbf{x}';\mathbf{x}_g,\omega), \quad (4.4)$$

where $M(\theta_s,\theta_g,\mathbf{x}')$ is the local scattering matrix (LSM) (Wu et al., 2004) which gives the scattering amplitude at location $\mathbf{x}'$ for unit incident-scattering angle pairs (θ_s,θ_g); it contains information of the local structure and the elastic properties. $G(\theta_s,\mathbf{x}';\mathbf{x}_s,\omega)$ and $G(\theta_g,\mathbf{x}';\mathbf{x}_g,\omega)$ are the plane wave components of Green's function incident on $\mathbf{x}'$ in the direction of θ_s and θ_g, respectively. The reciprocity $G(\theta_g,\mathbf{x}';\mathbf{x}_g,\omega) = G(\theta_g,\mathbf{x}_g;\mathbf{x}',\omega)$ is used.

4.3.2 Local image matrix and local scattering matrix

If equation 4.4 is substituted into equation 4.1, the migration image is expanded to local image matrix (LIM) which is a collection of angle-domain partial images

$$I(\mathbf{x};\mathbf{x}_s) = \sum_{\theta_s}\sum_{\theta_g} I(\theta_s,\theta_g,\mathbf{x};\mathbf{x}_s), \quad (4.5)$$

where the angle-domain partial image is

$$I\left(\theta_s,\theta_g,\mathbf{x};\mathbf{x}_s\right)=\sum_{\omega}\sum_{\mathbf{x}_g}s(\omega)s^*(\omega)G\left(\mathbf{x};\mathbf{x}_s,\omega\right)$$
$$\left[\sum_{\mathbf{x}'}G^*\left(\theta_s,\mathbf{x}';\mathbf{x}_s,\omega\right)R\left(\theta_s,\theta_g,\mathbf{x}'\right)G^*\left(\theta_g,\mathbf{x}';\mathbf{x}_g,\omega\right)\right]\frac{\partial G\left(\mathbf{x};\mathbf{x}_g,\omega\right)}{\partial n},\quad(4.6)$$

If the migration model is close enough to the true model, the focusing point $\mathbf{x}$ will be very close to the true reflection point $\mathbf{x}'$. Therefore, the Green's function on the focusing point in the imaging process will almost have the same propagation direction as the Green's function on the true reflection point. So equation 4.6 is simplified to

$$I\left(\theta_s,\theta_g,\mathbf{x};\mathbf{x}_s\right)=R\left(\theta_s,\theta_g,\mathbf{x};\mathbf{x}_s\right)M\left(\theta_s,\theta_g,\mathbf{x}\right),\quad(4.7)$$

where

$$R\left(\theta_s,\theta_g,\mathbf{x};\mathbf{x}_s\right)=\sum_{\omega}s(\omega)s^*(\omega)$$
$$G\left(\theta_s,\mathbf{x};\mathbf{x}_s,\omega\right)G^*\left(\theta_s,\mathbf{x};\mathbf{x}_s,\omega\right)\sum_{\mathbf{x}_g}G^*\left(\theta_g,\mathbf{x};\mathbf{x}_g,\omega\right)\frac{\partial G\left(\theta_g,\mathbf{x};\mathbf{x}_g,\omega\right)}{\partial n},\quad(4.8)$$

is the target illumination matrix. LSM is the intrinsic property of the scattering medium. The LIM is an image of the LSM but often distorted because of the acquisition aperture limitation and the wave propagation through the overburden structures. Compared with source illumination defined as

$$S\left(\theta_s,\mathbf{x};\mathbf{x}_s\right)=\sum_{\omega}s(\omega)s^*(\omega)G\left(\theta_s,\mathbf{x};\mathbf{x}_s,\omega\right)G^*\left(\theta_s,\mathbf{x};\mathbf{x}_s,\omega\right),\quad(4.9)$$

the target illumination R not only takes into account of the propagation effects on the source-side, but also the propagation effects caused by the limited aperture on the receiver-side. It relates the LIM to LSM. Theoretically, after determine R, we can use equation 4.7 to convert the migration image into the scattering property of an interface and find the AVA.

Figure 4.1 shows a two layer velocity model and the acquisition system for the numerical experiment. An image point on the interface is selected to demonstrate the multi-shot LIM which is shown in Figure 4.2a. In a LIM, the horizontal axis is the incident angle and the vertical axis is the scattering angle. The two diagonal axes are the reflection angle and dipping angle, respectively. The relations between two pairs of angles are given by (see Figure 4.1)

$$\theta_d = \left(\theta_s + \theta_g\right) / 2\,, \tag{4.10}$$

$$\theta_r = \left(\theta_s - \theta_g\right) / 2\,. \tag{4.11}$$

The image point is located on a planar reflector, so an energy strip is formed at the target dip in LIM. The energy strip is the angle-domain common image gather (ADCIG). Figure 4.2b gives the amplitude behavior of ADCIG. The image amplitude cannot be directly used for AVA analysis because it is distorted by the propagation effects introduced in the migration process. The multi-shot target illumination and source illumination are shown in Figure 4.2c and 4.2e. The target illumination and source illumination are almost the same except at large reflection angle and large dip. Those are mostly affected by the incomplete coverage of sources and receivers. Amplitude curves are extracted at the target dip and are illustrated in Figure 4.2d and 4.2f. The target illumination shown in 4.2d is very consistent with the amplitude behavior of ADCIG shown in 4.2b; while the source illumination shown in 4.2f is merely consistent with ADCIG at small reflection angle. Note that in this example the aperture is very wide and overburden structures above the image point are simple. In this simple case, the image compensation with source illumination will give reasonable AVA and is efficient to implement. However, if the aperture is limited, or the overburden structures are very complicated, the transmission lost on the receiver side cannot be ignored. In this case, it is inevitable to compensate the image with target illumination in order to get a true-amplitude image.

4.4 FAST IMPLEMENTATION

The construction of LIM requires the wavefields decomposition along all propagation directions followed by cross-correlation between every possible combination (Yan and Xie, 2012). The seismic event will display its angle information in local image matrix. To avoid the full-scale angle decomposition, we propose to efficiently measure the propagation angle from the wavefields before applying the imaging condition so that we can directly target the seismic event in LIM.

4.4.1 Incident angle

The mono-frequency wavefield contains all the directional information within the total recording time, so the mono-frequency source wavefield can be used to determine the incident angle. The goal can be achieved by conducting local slant stacking to the source wavefields $u_s(\mathbf{r},\omega)$ (usually the source wavefields at the dominant frequency is selected for the angle measurement):

$$u_s(\theta,\mathbf{x},\omega) = \int W(\mathbf{x}'-\mathbf{x}) u_s(\mathbf{x}',\omega) e^{-i\omega p(\mathbf{x}'-\mathbf{x})\cdot\hat{\mathbf{e}}_\theta} d\mathbf{x}', \tag{4.12}$$

where $W(\mathbf{x}'-\mathbf{x})$ is a local spatial window function centered at location $\mathbf{x}$; $\hat{\mathbf{e}}_\theta$ is the unit vector specifying the propagation direction; $p = 1/\overline{v}$ is the slowness, in which $\overline{v}$ is the average velocity within W.

Shown in Figure 4.3 is the velocity model superimposed by a mono-frequency wavefield generated by a shot which is indicated in the model. Eight locations are selected in the wavefields and their angle-domain analysis results are illustrated on the top and bottom of the figure. All the energy peaks are located along dispersion circle $p = 1/\overline{v}$. Each energy peak represents a local plane wave. Its propagation angle is revealed by the polar angle of the energy peak. If multi-pathing occurs, multiple energy clusters will display in the angle domain and multiple incident angles can be identified. It is possible to include all arrivals into imaging but here we only select the most energetic arrival and use it as the incident angle. Though multi-arrivals are neglected, it is reasonable to make this assumption for the purpose of AVA analysis.

4.4.2 Structure dip

Since receiver wavefields are more complicated than source wavefields, we prefer not to measure the scattering angle in the same way as incident angle. However, the dip angle can be easily scanned from the stacked migration image using Fourier transform, so that the scattering angle can be calculated from the dip angle and the incident angle. Shown in Figure 4.4b is the multi-shot stacked migration image from the velocity model shown in Figure 4.3. Eight image spectra are demonstrated at selected points in the migration image. They are resulted from Fourier transform of the local migration image. The direction which has the dominant energy in the image spectrum represents the normal direction of the local reflector and thus can be used as the dip angle. It works well in areas with clear dip. In areas encountered diffraction points or interceptions of multiple structures, the measurements of dip angles are usually ambiguous. Fortunately, these areas are not the target areas of AVA analysis and will be discarded in analysis.

4.4.3 AVA response

With known incident and dipping angles, we can calculate the scattering angle using equation 4.10. To create ADCIG, we directly project the multi-frequency source and receiver waves along the directions of incident and scattering angles using local slant stacking equation 4.12. Note, with known incident and scattering angles, we do not need to scan the entire angle domain to find the right directions. Instead, we only need to substitute the angle into equation 4.12 to calculate once. This can save tremendous computation times. After obtaining the directional source and receiver waves, we can form the angle-domain partial image and map it from shot domain to reflection angle domain:

$$I\left(\theta_r = \frac{\theta_s - \theta_g}{2}, \mathbf{x}\right) = \sum_{\omega} u_s\left(\theta_s, \mathbf{x}; \mathbf{x}_s, \omega\right) \cdot u_g^*\left(\theta_g, \mathbf{x}; \mathbf{x}_s, \omega\right), \tag{4.13}$$

where $u_s\left(\theta_s, \mathbf{x}; \mathbf{x}_s, \omega\right)$ is the local incident plane wave and $u_g\left(\theta_g, \mathbf{x}; \mathbf{x}_s, \omega\right)$ is the local scattered plane wave.

The reflection-angle-dependent target illumination is calculated in the same fashion as ADCIG. The wavefield carries most of the energy around the dominant frequency. As an approximation, instead of summing up all the frequencies, we calculate the target illumination at the dominant frequency

$$R\left(\theta_r=\frac{\theta_s-\theta_g}{2},\mathbf{x}\right)=s(\omega)s^*(\omega)$$
$$G(\theta_s,\mathbf{x};\mathbf{x}_s,\omega_0)G^*(\theta_s,\mathbf{x};\mathbf{x}_s,\omega_0)\sum_{\mathbf{x}_g}G^*(\theta_g,\mathbf{x};\mathbf{x}_g,\omega_0)\frac{\partial G(\theta_g,\mathbf{x};\mathbf{x}_g,\omega_0)}{\partial n},\qquad(4.14)$$

where ω_0 is the dominant frequency; the plane wave components of Green's function $G(\theta_s,\mathbf{x};\mathbf{x}_s,\omega_0)$ and $G(\theta_g,\mathbf{x};\mathbf{x}_g,\omega_0)$ are calculated with equation 4.12. Again, the calculation is for known θ_s and θ_g. Angle domain scan is not required and the calculation is very efficient. Note that the source wavelet is ignored in the equation.

Finally, AVA response is obtained by normalizing ADCIG with the target illumination:

$$M(\theta_r,\mathbf{x})=\frac{I(\theta_r,\mathbf{x})}{R(\theta_r,\mathbf{x})}.\qquad(4.15)$$

where $M(\theta_r,\mathbf{x})$ is the AVA response retrieved from the migration image. Figure 4.5 shows the amplitude behavior of ADCIG, target illumination and AVA response retrieved at the same location as in Figure 4.1 and 4.2 with the fast implementation described above. Note that those results are obtained in shot domain and then converted to angle domain while the results shown in Figure 4.2 are directly extracted in angle domain. Though the two approaches will lead to the same AVA result, but ADCIG and target illumination used to calculate AVA appear very different. The shot footprint is included in the angle-domain results while not in the shot-domain results.

4.4.4 Computational issues

The computational efficiency is largely improved by taking the following two advantages: (1) The mono-frequency wavefield contains the directional information while processing mono-frequency wave to find the propagation direction is much cheaper than processing the entire space-time wavefield; (2) With known incident and scattering angles, the local slant stacking can directly project the space-time wavefield to the given direction. The time consuming angle-domain scan or full-scale transform is no longer required.

With conventional implementation, the construction of LIM needs a full-scale angle-domain scan for the multi-frequency wavefields. The decomposition takes $O\left(2 \cdot N_{angle} \cdot N_{\omega}\right)$ arithmetic operations, where N_{angle} is the number of propagation directions and N_{ω} is the number of frequencies. The new method uses mono-frequency wavefields to find the propagation direction followed by using the slant stack to project the space-domain wavefields to the known direction. The process takes $O\left(N_{angle} + 2 \cdot N_{\omega}\right)$ arithmetic operations. Hence, the computational efficiency is increased by a factor of $2N_{angle}N_{\omega} \big/ \left(N_{angle} + 2N_{\omega}\right)$.

The conventional method to calculate the angle-domain target illumination sums up all the frequency components. However, the computational cost is reduced by a factor of N_ω if only the mono-frequency wave is used to calculate the target illumination.

4.5 AVA ANYLYSIS

For relatively small incidence angles, usually less than 30 degrees, the reflectivity of compressive wave can be approximated by an equation (Shuey, 1985):

$$M(\theta) = A + B \cdot \sin^2 \theta, \tag{4.16}$$

where θ is the reflection angle. A is the intercept and B is the slope.

For an interface crossing for which the velocity and density perturbations are small, the intercept and slope can be approximated by

$$A = \frac{\Delta V_P}{2V_P} + \frac{\Delta \rho}{2\rho}, \tag{4.17}$$

$$B = \frac{\Delta V_P}{2V_P} - 4\frac{V_S^2}{V_P^2}\left\{\frac{\Delta \rho}{2\rho} + \frac{\Delta V_S}{V_S}\right\}, \tag{4.18}$$

where V_P, V_s and ρ are the average P-wave velocity, S-wave velocity and density above and below the interface, respectively; ΔV_P, ΔV_s and $\Delta\rho$ are the differences in P-wave velocity, S-wave velocity and density crossing the interface.

Let $\gamma = V_S / V_P$, the relation between slope B and intercept A (Foster and Keys, 1999; Foster et al, 2010) is

$$B = \left(1-8\gamma^2\right)A - 4\gamma\Delta\gamma + \left(4\gamma^2-1\right)\frac{\Delta\rho}{2\rho}. \quad (4.19)$$

If the ratio γ is close to 0.5, the last term can be neglected as a second-order perturbation, yielding

$$B = \left(1-8\gamma^2\right)A - 4\gamma\Delta\gamma . \quad (4.20)$$

In a crossplot of A versus B, if there is little contrast in V_S/V_P, the reflection tends to fall on the fluid line

$$B = \left(1-8\gamma^2\right)A. \quad (4.21)$$

From equation 4.17, 4.18 and 4.20, the key elastic properties controlling the angle-dependent reflection coefficient are acoustic-impedance contrast and contrast in V_P/V_S. Compared with the standard reflectivity curves, using intercept A and slope B is a concise and intuitive way to present AVO behavior. Shown in Table 4.1 are elastic parameters of shale and nine types of reservoirs. The corresponding nine pairs of intercepts and slopes are calculated by equations 4.17 and 4.18 and are cross-plotted in Figure 4.6.

In Figure 4.6 the reflections from the top of sand fall on a trend approximately parallel to the fluid line but with a negative intercept in the cross-plot domain. The reflections from the base of sand fall on a parallel trend on the opposite side of the fluid line. Each trend is defined by a V_P/V_S contrast (See equation 4.20). Hydrocarbon reservoirs typically have a lower V_P/V_S than the surrounding formation, and increasing pore fluid compressibility even reduces V_P/V_S . Thus gas produces the greatest departure from the fluid line, followed by oil and brine. Porosity is another rock property that has an impact on seismic responses. Increasing the porosity decreases acoustic impedance, but does not significantly affect V_P/V_S . As a result, porosity changes move the AVA responses along the trend parallel to fluid line.

4.6 NUMERCIAL EXAMPLES

We first use a simple layered reservoir model to extract the AVA and use it to calibrate the method. The background medium is the shale with constant velocity. A horizontal reservoir layer (hydrocarbon-saturated porous sand) is embedded in the background. Different pore fluids (gas, oil or brine) are filled into the reservoir layer. The elastic parameters of shale and nine types of reservoirs are shown in Table 4.1.

For this simple model, the seismic data are generated using an elastic finite difference code, and the acoustic RTM is employed to migrate the pressure seismic data. We select a vertical line in the model and show the ADCIGs in Figure 4.7. We normalized ADCIGs by the target illumination and compare the AVA responses with the theoretical reflection coefficients (Aki and Richards, 1980) in Figure 4.8. The extracted AVA response agrees very well with the theoretical reflectivity. Generally speaking, in this simple case, the proposed method can obtain reliable AVA responses.

In the second example, we design an elastic model (Figure 4.9a) to test our AVA analysis method. A hydrocarbon reservoir is embedded in the middle of the model, ranging between 2.5 km to 5.5 km along the distance and from 1.25 km to 1.75 km at depth. The reservoir has 23% pore porosity, and filled with gas, oil or brine. Their elastic parameters are shown in Table 4.1. For the background shale, V_P/V_S is about 1.9. There are multiple thin layers in both the background shale and the reservoir. We generate a synthetic data set which contains 71 shots ranging from 0.5 km to 7.5 km and 301 double-side receivers with a maximum offset of 6 km. The source time function is a 30 Hz Ricker wavelet.

Shown in Figure 4.9b is the stacked migration image produced by cross-correlation imaging condition. ADCIGs are obtained from shot-domain CIGs sorted by reflection angles. The AVA responses are extracted from ADCIGs and then fitted with equation 4.10 using least square fitting method, which gives the intercept A and slope B. Figure 4.10 depicts the AVA responses computed from subsurface ADCIGs in cross-plot domain. Reflectivity curve is extracted and then is fitted with equation 4.10 using least square fitting method. From Figure 4.8a to 4.8c, the pore fluids in the reservoir are gas, oil and brine. The reflections from shale, which have little contrast in V_P/V_S, fall near the fluid line. The reflections from the top of reservoir appear at the lower-left side of the fluid line and the bottom reflections appear at the upper-right side of the fluid line. In Figure 4.10a, the reflections from the reservoir stay furthest away from the fluid line. In Figure 4.10b and 4.10c, the reflections get closer to the fluid line, but still can be clearly distinguished from the background reflections in the cross-plot domain. Although there are overburden structures and the top of the reservoir has a complex shape and medium dips, the proposed method extracts correct AVAs from the background.

4.7 CONCLUSIONS

We provide an efficient method to extract the AVA under the RTM frame, and the results are investigated in the cross-plot domain. The new method extracts the AVA from the migrated wavefield and can remove the effect of the overburden structure. The AVA measurement is angle dependent. The incident angle is determined from the mono-frequency source wavefield by using only the most energetic phase. The dip angle is measured from the migration image. Based on Snell's law, the scattering and reflection angles can be calculated from incident and dip angles. Local slant stacking method is employed to project the broadband source and receiver wavefields as well as dominant-frequency Green's function to the incident and scattering directions. The resultant local plane waves are used to form ADCIG and target illumination. AVA responses are computed by normalizing ADCIG with the corresponding angle-domain illumination. The intercept and slope of AVA are extracted and further analyzed in cross-plot domain. The numerical examples demonstrate that the proposed approach is both efficient and accurate.The AVA extracted from top and bottom of the reservoir show distinctive behavior comparied to those from background shales in cross-plot domain.

4.8 REFERENCES

Aki, K., and P. G. Richard, 1980, Quantitative Seismology: W. H. Freeman & Co.

Audebert, F., P. Froidevaux, H. Rakotoarisoa, and J. SvayLucas, 2002, Insights into migration in the angle-domain: 72nd Annual International Meeting, SEG, Expanded Abstracts.

Bleistein, N., 1987, On the imaging of reflectors in the earth: Geophysics, 52, 931-942.

Brandsberg-Dahl, S., M. de Hoop, and B. Ursin, 2003, Focusing in dip and AVA compensation on scattering-angle/azimuth common image gathers: Geophysics, 68(1), 232–254.

Cao, J. and R. S. Wu, 2008, Amplitude compensation for one-way wave propagators in inhomogeneous media and its application to seismic imaging, Communications in Computational Physics, 3(1): 203-221.

Cao, J., and R. S. Wu, 2009, Fast acquisition aperture correction in prestack depth migration using beamlet decomposition, Geophysics, 74(4), S67–S74.

Castagna, J.P. and M. M. Backus, 1993, AVO analysis—tutorial and review, in Offset-Dependent Reflectivity—Theory and Practice of AVO analysis, Vol. 8, pp. 3–36, eds Castagna, J.P. and M. M. Backus, Investigations in Geophysics, Society of Exploration Geophysicists, Tulsa, Oklahoma.

Chattopadhyay, S., G. A. McMechan, 2008, Imaging conditions for prestack reverse-time migration: Geophyiscs, 73, S81-S89.

Claerbout, J. F., 1971, Towards a unified theory of reflector mapping: Geophysics, 36, 467-481.

Chiburis, E. F., 1984, Analysis of amplitude versus offset to detect gas-oil contacts in Arabia Gulf: 54th Annual International Meeting, SEG, Expanded Abstracts, 669-670.

Foster, D. J., and R. G. Keys, 1999, Interpreting AVO responses: 69th Annual International Meeting, SEG, Expanded Abstracts, 748-751.

Foster, D. J., R. G. Keys, and F. D. Lane, 2010, Interpretation of AVO anomalies: Geophysics, 75, 75A3-75A13.

Guitton, A., A. Valenciano, D. Bevc, and J. Claerbout, 2007, Smoothing imaging condition for shot-profile migration: Geophysics, 72, S149-S154.

Hanitzsch, C., 1995, Amplitude preserving prestack Kirchhoff depth migration/inversion in laterally inhomogeneous media: Ph.D. dissertation, University of Karlsruhe.

Hubral, P., M. Tygel, M., and H. Zien, 1991, Three-dimensional true-amplitude zero-offset migration. Geophysics, 56(1), 18–26.

Jin, S., M. Luo, S. Xu, and D. Walraven, 2006, Illumination amplitude correction with beamlet migration: The Leading Edge, 25(9), 1046–1050.

Mao, J. and R. S. Wu, 2010, Target oriented 3D acquisition aperture correction in local wavenumber domain: 80th Annual International Meeting, SEG, Technical Program Expanded Abstracts, 3237-3241.

Mosher, C.C., T.H. Keho, A.B. Weglein and D.J. Foster, 1996, The impact of migration on AVO: Geophysics, 61, 1603-1615.

Sava, P., and S. Fomel, 2003, Angle-domain common image gathers by wavefield continuation methods: Geophysics, 68, 1065-1074.

Sava, P., and S. Fomel, 2005, Time-shift imaging condition: 75th Annual International Meeting, SEG, Expanded Abstracts, 1850-1853.

Sava, P., and I. Vasconcelos, 2011, Extended imaging condition for wave-equation migration: Geophysical Prospecting, 59, 35–55.

Shuey, R. T., 1985, A simplification of the Zoeppritz equations: Geophysics, 50, no. 4, 609–614.

Ostrander, W.J., 1984, Plane wave reflection coefficients for gas sands at non normal angles of incidence: Geophysics, 49, 1637-1648.

Ursin, B., 1983, Review of elastic and electromagnetic wave propagation in horizontally layered media: Geophysics, 48, 1063-1081.

Valenciano, A., and B. Biondi, 2003, 2D deconvolution imaging condition for shot profile migration: 73rd Annual International Meeting, SEG, Expanded Abstracts, 1059-1062.

Vyas, M., E. Mobley, D. Nichols, and J. Perdomo, 2010, Angle gathers for RTM using extended imaging conditions: 80th Annual International Meeting, SEG, Expanded Abstracts, S252-S256.

Wu, R. S., and J. Cao, 2005, WKBJ solution and transparent propagators: 67th Annual International Meeting, EAGE, extended abstracts, P167.

Wu, R. S., M. Q. Luo, S. C. Chen, and X. B. Xie, 2004, Acquisition aperture correction in angle-domain and true-amplitude imaging for wave equation migration: 74th Annual International Meeting, SEG, Expanded Abstracts, 937–940.

Wu, R. S., and L. Chen, 2003, Prestack depth migration in angle-domain using beamlet decomposition: Local image matrix and local AVA: 73rd Annual International Meeting, SEG, Expanded Abstracts, 973–976.

Wu, R. S., and M. Q. Luo, 2005, Comparison of different schemes of image amplitude correction in prestack depth migration: 75th Annual International Meeting, SEG, Expanded Abstracts, 2060–2063.

Xie, X. B., and R. S. Wu, 2002, Extracting angle domain information from migrated wavefields: 72nd Annual International Meeting, SEG, Expanded Abstracts, 1360-1363.

Xie, X. B., and H. Yang, 2008, A full-wave equation based seismic illumination analysis methods: 70th Conference and Exhibition, EAGE, Extended Abstract, P284.

Xu, S., H. Chauris, G. Lambare, and M. Noble, 2001, Common-angle migration: A strategy for imaging complex media: Geophysics, 66, 1877–1894.

Xu, S., Y. Zhang, and B. Tang, 2011, 3D common image gathers from reverse time migration: Geophysics, 76, S77–S92.

Yan, R. and X. B. Xie, 2012, An angle-domain imaging condition for elastic reverse time migration and its application to angle gather extraction: Geophysics, 77, No 5, S105–S115.

Yilmaz, O., 2001, Seismic Data Analysis: Processing, Inversion and Interpretation of Seismic Data (Vols. 1 & 2): Society of Exploration Geophysicists, Tulsa Oklahoma.

Yoon, K., K. Marfurt, and E. W. Starr, 2004, Challenges in reverse-time migration: 74th Annual International Meeting, SEG, Expanded Abstracts, 1057–1060.

Zhang Y., G. Zhang, and N. Bleistein, 2003, True amplitude wave equation migration arising from true amplitude one-way wave equation: Inverse Problems, 19, 1113-1138.

Zhang Y., G. Zhang, and N. Bleistein, 2005, Theory of true-amplitude one-way wave equations and true-amplitude common-shot migration: Geophysics, 70, E1-E10.

Zhang, Q. and G. A. McMechan, 2011, Direct vector-field method to obtain angle-domain common-image gathers for isotropic acoustic and elastic reverse-time migration: Geophysics, 76, WB135-WB149.

Zhang, Y., J. Sun, and S. H. Gray, 2007, Reverse-time migration: amplitude and implementation issues: 77th Annual International Meeting, SEG, Expanded Abstract, 2145-2149.

Zhang, Y., S. Xu, B. Tang, B. Bai, Y. Huang and T. Huang, 2010, Angle gathers from reverse time migration: The Leading Edge, 29, 1364 – 1371.

4.9 FIGURES AND TABLES

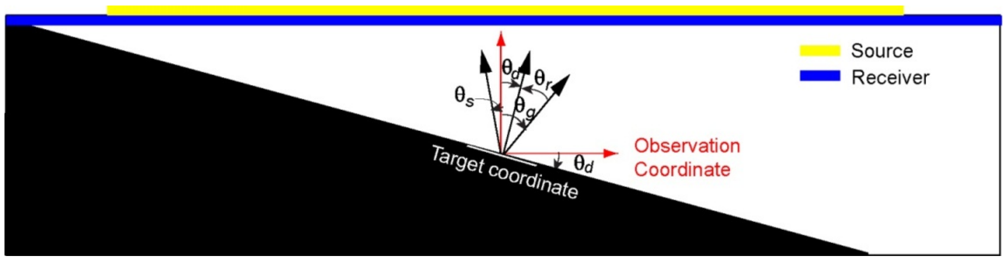

Figure 4.1 A velocity model consisting of two layers separated by a dipping interface. The elastic parameters of the upper and lower layers are $v_p = 3170\,m/s$, $v_s = 1668\,m/s$, $\rho = 2360\,kg/m^3$ and $v_p = 3550\,m/s$, $v_s = 1850\,m/s$, $\rho = 2360\,kg/m^3$. The coverage of shots and geophones are shown in the figure. The shots move with fixed geophones which cover the whole surface of the model. The coordinate system used for angle-domain analysis is shown in the figure. The incident and scattering angles are defined in the observation coordinate. The reflection angle and dipping angle are defined in the target coordinate.

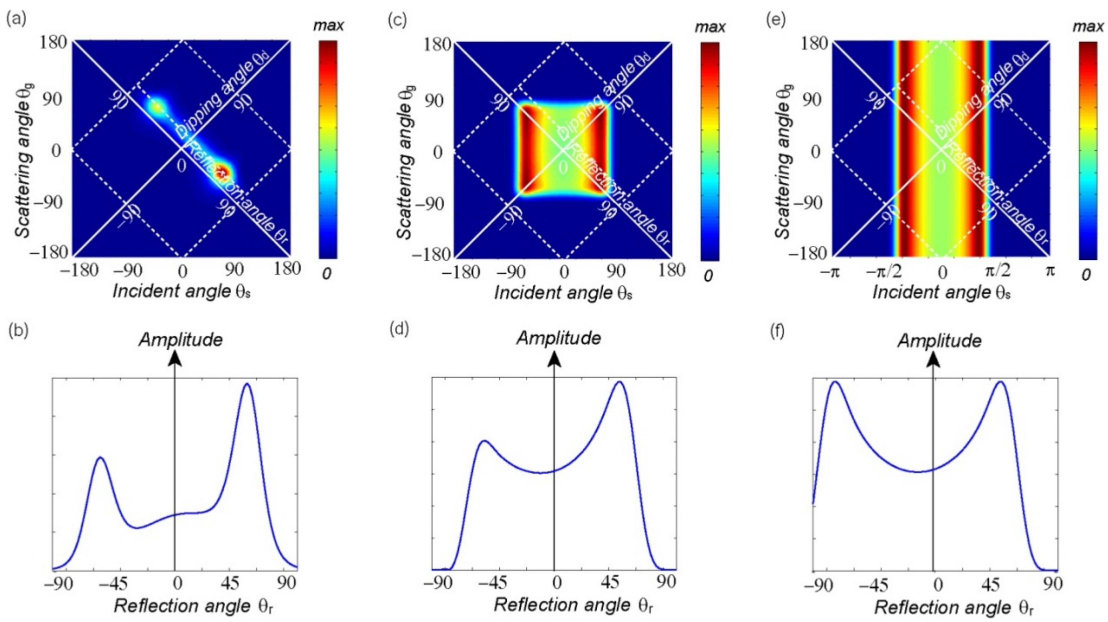

Figure 4.2 (a) The multi-shot local image matrix for an image point located on the dipping interface in Figure 1. (b) The amplitude behavior of ADCIG extracted from (a). (c) The multi-shot target illumination. (d) The amplitude of target illumination as a function of reflection angle at the target dip. (e) The multi-shot source illumination. (f) The amplitude of source illumination as a function of reflection angle at the target dip. In all the matrices, the horizontal and vertical coordinates are incident and scattering angles, respectively, while the two diagonals are dipping angle and reflection angle, respectively.

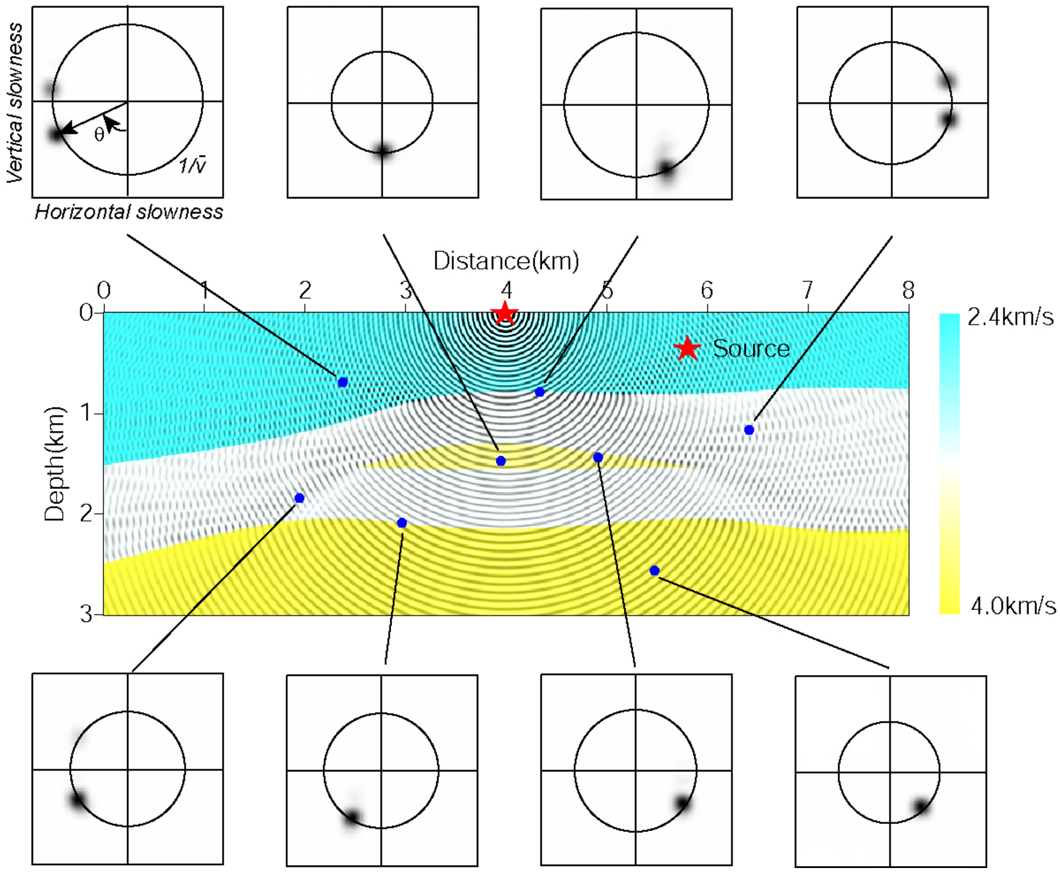

Figure 4.3 A velocity model used to demonstrate how to measure the propagation direction from mono-frequency wavefields. The mono-frequency wavefields generated from a shot is superposed on a velocity model. The shot location is indicated in the figure. Eight image locations are selected in the wavefields and their slowness analyses are shown on the top and bottom of the figure. Without exception, all the energy peaks are located along the dispersion circle indicated by average velocity.

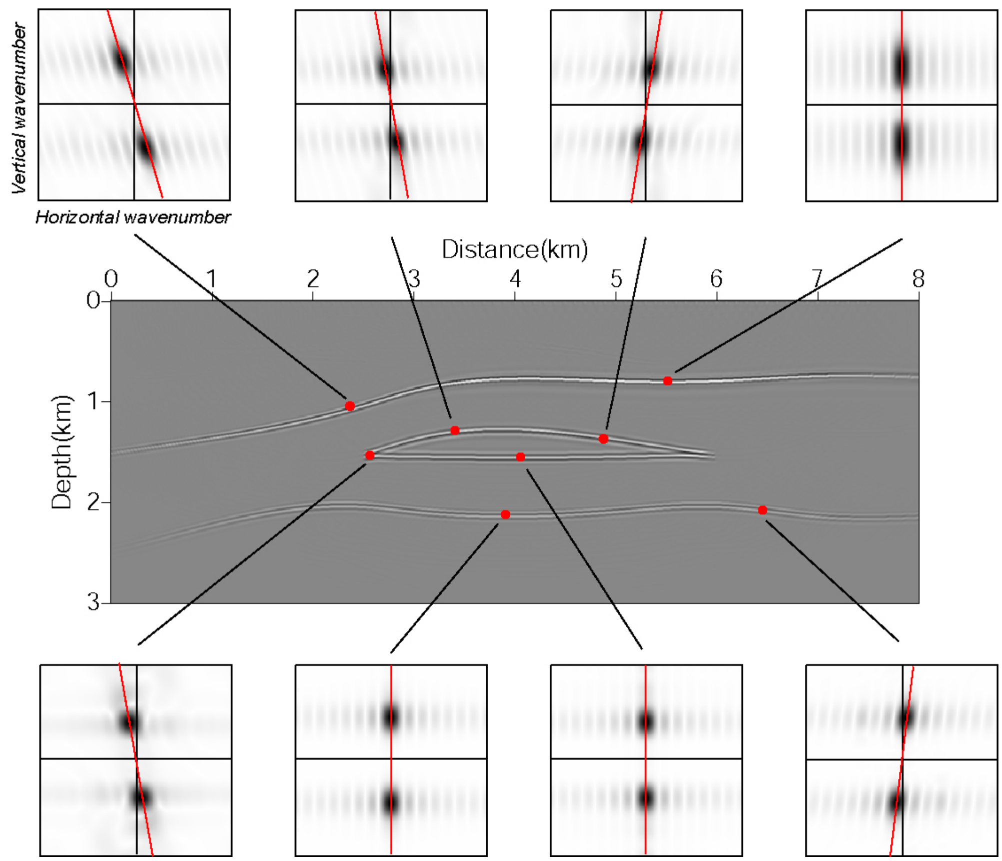

Figure 4.4 The local image spectrum calculated from the stacked migration image. Shown at the center is the stacked image marked with the location where the spectra are calculated. The shape of the spectra clearly gives the dipping angle of the image.

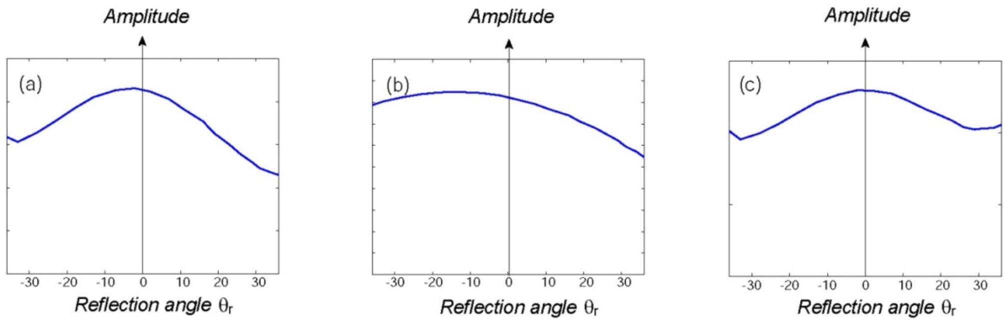

Figure 4.5 (a) the amplitude curve of ADCIG, (b) the amplitude curve of target illumination which is a function of reflection angle, and (c) AVA response obtained by normalizing ADCIG with target illumination.

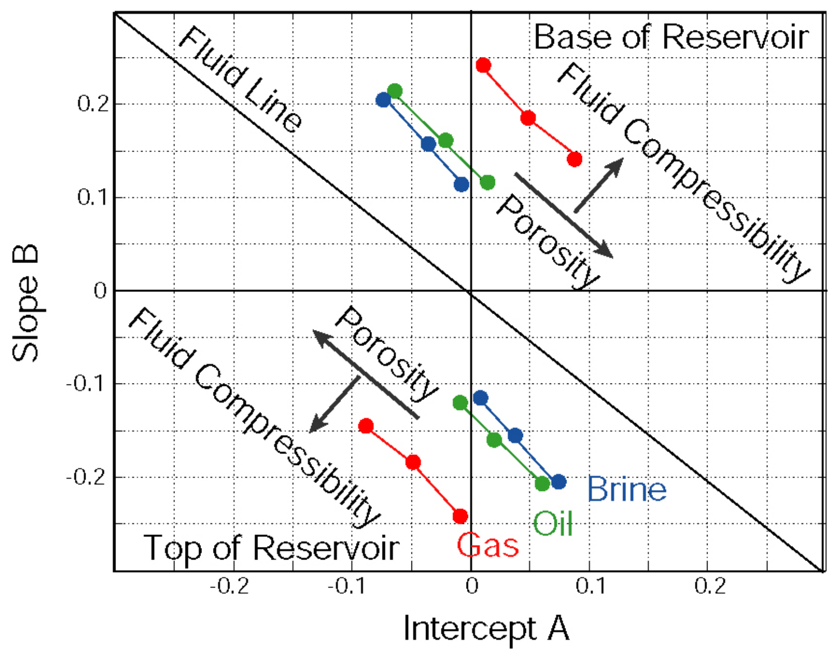

Figure 4.6 Changes of reservoir parameters on AVA responses shown in the A versus B cross-plot. An increase in pore-fluid compressibility displaces reflection response farther from the fluid-line trend. An increase in porosity moves the reflection response parallel to the fluid-line trend, in the direction of the solid arrows.

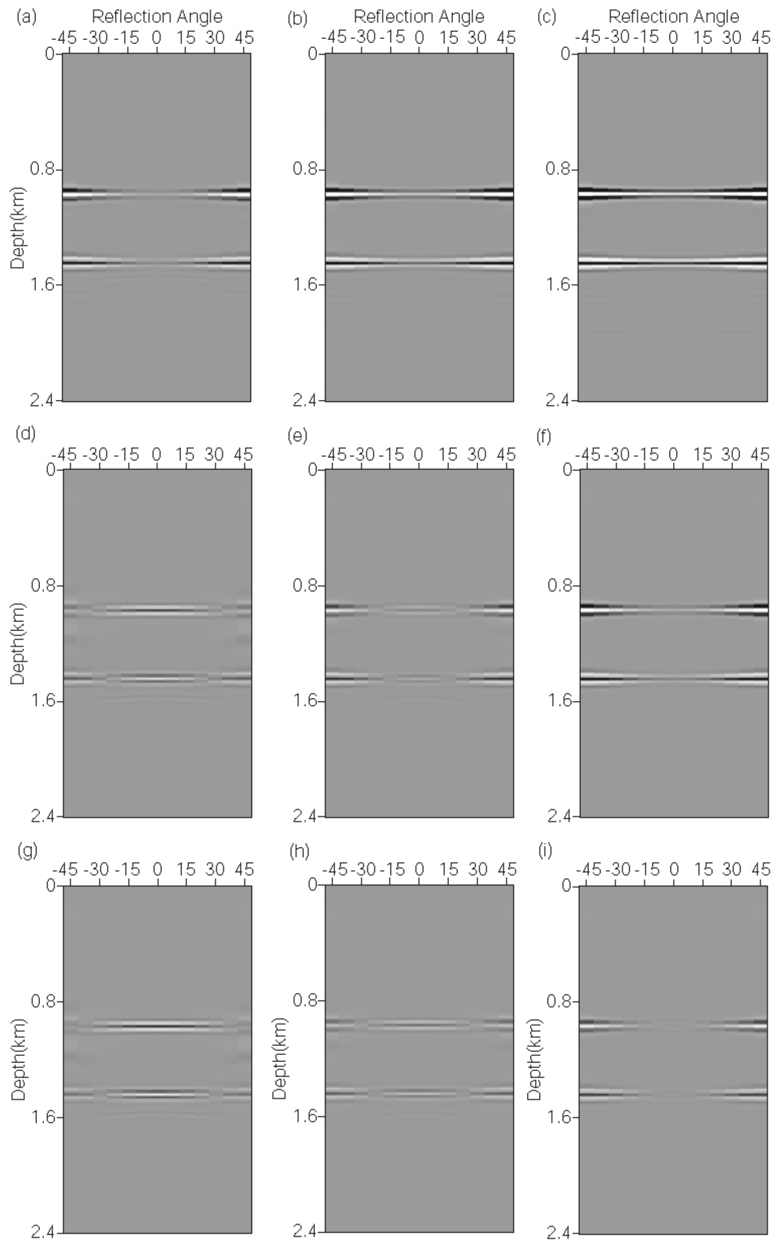

Figure 4.7 ADCIGs corresponding to nine different interfaces listed in Table 2. (a)-(c) are from shale/gas interfaces, (d)-(f) shale/oil interfaces, and (g)-(i) shale/brine interfaces. From left to right, the porosities are 20%, 23% and 25%, respectively. Note at certain reflection angles the reflectivity changed polarity.

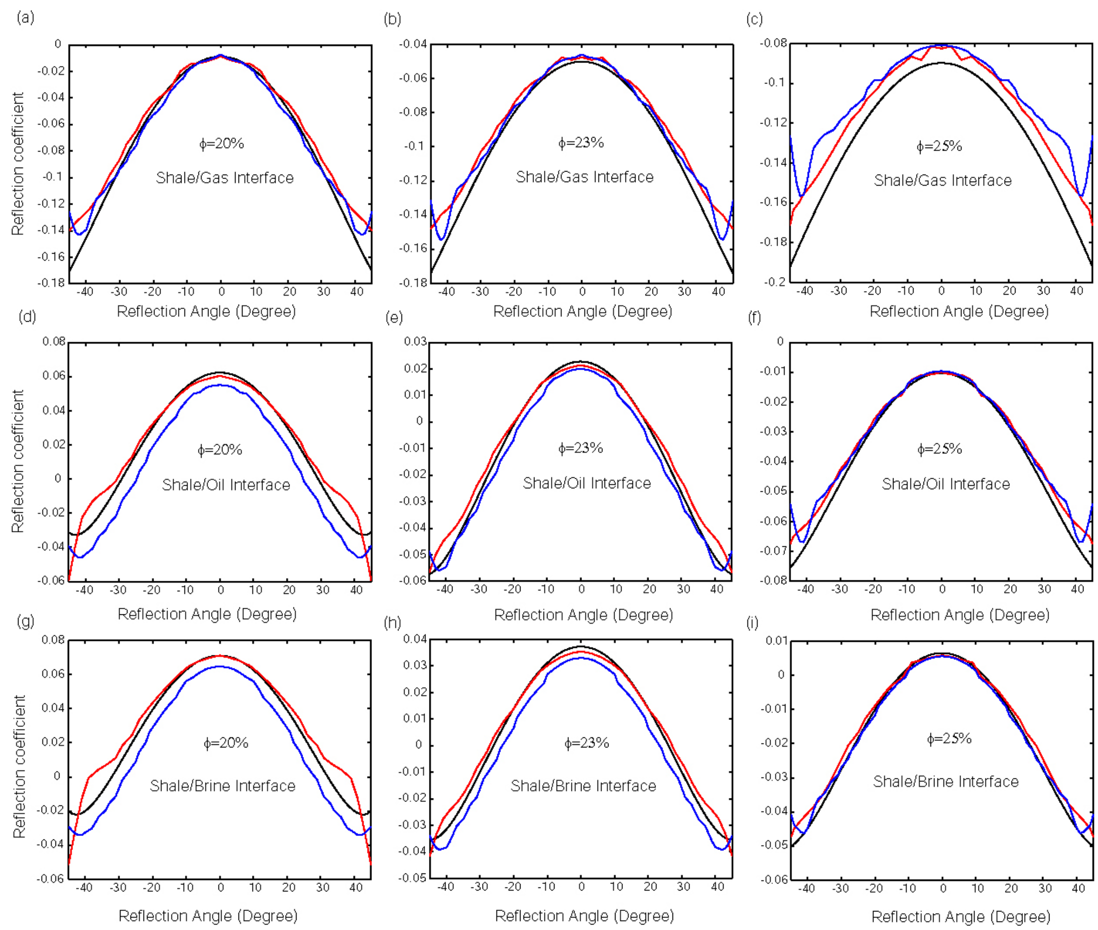

Figure 4.8 The comparison between the theoretical reflectivity and AVAs extracted at the top and bottom of the reservoir model. The incident angle is measured from the single-frequency source wavefield and AVA is retrieved from target-illumination-normalized ADCIG that is constructed by the cross-correlation of decomposed source and receiver wavefield. The black curve is the theoretical reflection coefficient. The red and blue curves are obtained from the top and the bottom of the reservoir.

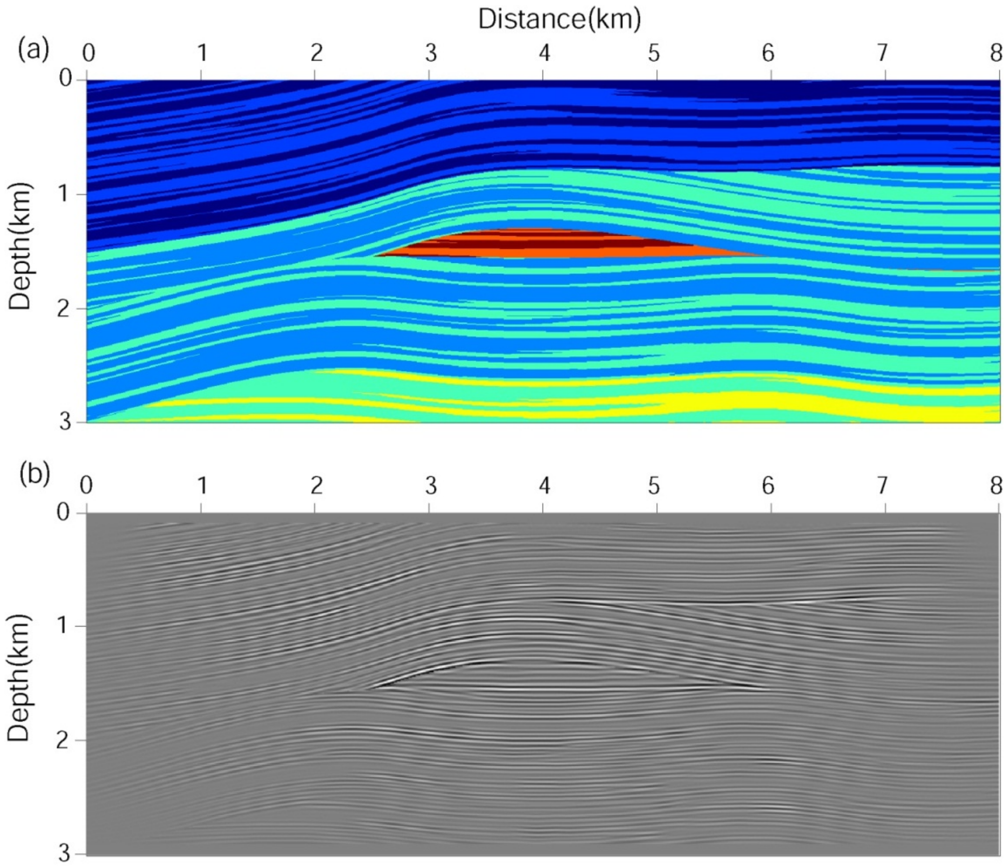

Figure 4.9 (a) The elastic velocity model. (b) The stacked migrated image produced by the cross-correlation imaging condition.

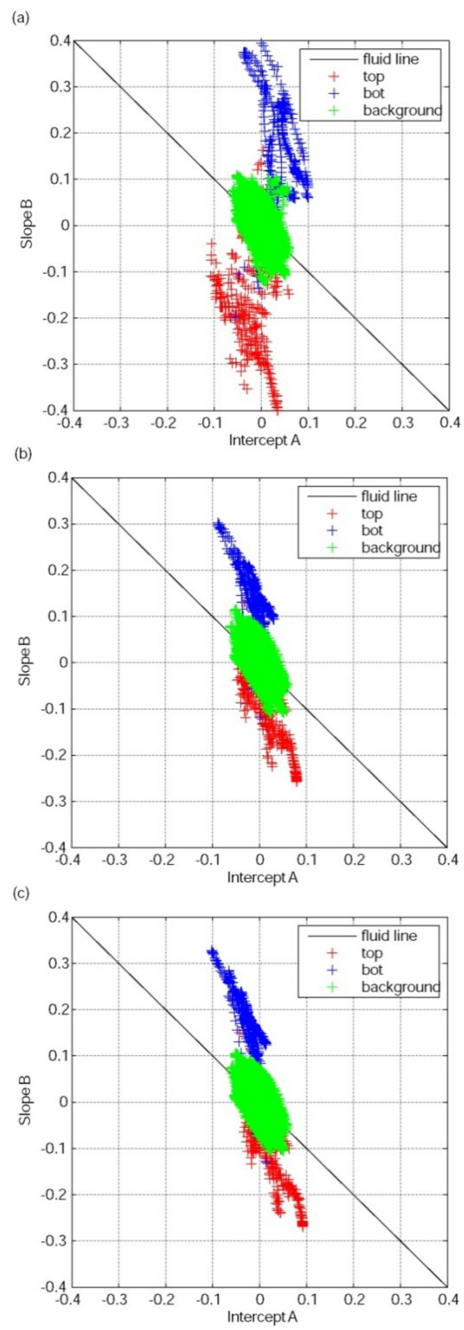

Figure 4.10 The crossplot panel of A versus B: (a) The pore fluid in reservoir is gas; (b) the pore fluid is oil; (c) the pore fluid is brine. The green crosses are from background reflections. The red and blue crosses are from the top and bottom of the reservoir.

Table 4.1 The elastic parameters of shale and hydrocarbon reservoir

	Percentage Porosity ϕ	P-velocity $V_P\left(m/s\right)$	S-velocity $V_S\left(m/s\right)$	Density $\rho\left(kg/m^3\right)$
Shale	20%	3170	1668	2360
	23%	3170	1668	2360
	25%	3170	1668	2360
Gas	20%	3500	2374	2100
	23%	3350	2231	2020
	25%	3188	2124	1960
Oil	20%	3734	2280	2270
	23%	3527	2131	2220
	25%	3362	2015	2180
Brine	20%	3749	2262	2310
	23%	3551	2109	2270
	25%	3399	1993	2230

5 ACQUISITION APERTURE CORRECTION IN ANGLE-DOMAIN TOWARDS THE TRUE-REFLECTION RTM[3]

5.1 SUMMARY

Due to the incomplete aperture coverage and complex overburden structures, the migration process cannot provide a true-reflection image even though a true-amplitude propagator, like RTM, is used. We develop a theory to relate the migration image to the true reflectivity in the dip angle domain and propose an amplitude correction method which is implemented at the post-image stage. The stacked migration image is decomposed into common dip images, which are compensated individually in the dip angle domain by the corresponding acquisition dip response. Then, the corrected images are summed up to form a final image consistent with the target impedance contrast. The Green's function at every shot/geophone location in the observation system is calculated and then decomposed into local plane waves. Based on the survey configuration, acquisition dip response is formulated as the total energy contributed from all the possible combinations of incident and scattered plane waves for a specific dip and is computed efficiently with the Green's functions at the dominant frequency. Two numerical experiments, a five-layer model and the SEG/EAGE salt model, demonstrate that the amplitude correction leads to an image amplitude that is much closer to the true reflectivity of subsurface structures.

[3] This Chapter has been submitted to Geophysics

5.2 INTRODUCTION

The ultimate goal of seismic imaging is to provide a reflector map consistent with the real subsurface structure correct geometrical locations of subsurface structures, and also the correct image amplitude, which reveals the reflection/scattering strength of the subsurface structure. However, the limited acquisition aperture and the complex overburden structure usually prevent us from obtaining correct image amplitude, even when accurate wave propagators are used. The combined effects from these two factors can cause irregular illuminations to subsurface structures, leading to biased image amplitude. To tackle this problem, Tarantola (1987) treated the image process as an inverse problem and solve it in an iterative way. However, the resulting approach usually is too expensive to practice. In addition, the instability and non-uniqueness are other unattractive features of the general inverse approach. Another approach lies between the conventional migration and general inversion. This method, the so called true-amplitude or true reflection imaging, applies a deconvolution operator to the distorted image and makes it proportional to the true reflectivity. The deconvolution operator is built based on the acquisition geometry and the background velocity model.

One important ingredient in this methodology is to use the amplitude-preserving wave propagator. Research along this direction has been developed for both the high-frequency asymptotic propagator (Bleistein et al., 1987; Hubral et al., 1991; Hanitzsch, 1995; Xu et al., 2001; Audebert et al., 2002; Brandsberg-Dahl et al., 2003) and the wave-equation based propagator (Ursin, 1983; Zhang et al., 2003, 2005; Wu and Cao, 2005; Cao and Wu, 2008). Without making any approximation to the wave equation, RTM can be considered as an amplitude-preserving propagator.

However, using true-amplitude propagator alone cannot guarantee true amplitude image. Acquisition geometry has been proved to be equally or even more important in recovering the true reflectivity (Wu et al., 2004; Cao and Wu, 2005). If the aperture is full, both geometric spreading and transmission loss can be compensated during back-propagation. But the limited aperture will cause irretrievable energy loss in the system so that will lead to incorrect image amplitude. In order to distinguish between the imaging using true-amplitude propagators alone with those pursuing true reflectivity, we call the latter "true-reflection imaging" or "true-reflectivity migration". In true-reflection imaging, we try to correct the conventional migration image to make the amplitude proportional to the local reflectivity. There are two different approaches in the literature. One is Hessian matrix based approach, which uses the inverse Hessian derived from the theory of least-square inversion (Tarantola, 1987) as the filter function applying to the original image. Since the inverse Hessian is difficult, if not impossible, to calculate, various approximations have been proposed for this approach (Hu et al., 2001; Rickett, 2003; Guitton, 2004; Plessix and Mulder, 2004; Valenciano et al., 2006, 2009). The second approach is resolution- or illumination-based approach. Resolution directly relates the migration image to the physical properties of the medium. Gelius et al. (2002) formulated the wavenumber-domain resolution function and used it to correct the migration image. This approach has been applied to the ray-based migration (Gelius et al., 2002; Lecomte et al., 2003, 2008) and one-way wave migration (Xie et al., 2005; Wu et al., 2006). Wu et al. (2004) proposed to compensate the image amplitude in local image matrix (LIM), which is in reflection and dipping angle domain. Wu and Luo (2005) tested different approaches for correction and demonstrated that the correction in dip angle domain has the greatest improvement to eliminate the acquisition effect. Later, based on the LEF (local exponential frame) decomposition, several authors (Jin et al., 2006; Cao and Wu, 2009; Mao and Wu, 2010) worked to speed up this technique.

In this chapter, we develop an amplitude correction algorithm implemented in dip angle domain to retrieve the true reflectivity of subsurface structure. We will start from the theory of amplitude correction in dip angle domain. The method used to calculate common dip image (CDI) will be provided in the second part. Third, we formulate acquisition dip response (ADR), which serves as the amplitude correction factor and explain some technical details. Both the ADR and CDI are obtained in RTM scheme. Finally, we will use 2D synthetic examples to demonstrate the great impact of ADR correction on the image amplitude.

5.3 THEORY

Consider using a survey system composed of a shot at $\mathbf{x}_s$ and a geophone at $\mathbf{x}_g$ to investigate the subsurface target region $V(x)$ surrounding $\mathbf{x}$. The wave radiated from the source, reflected from V and reaching to the geophone can be expressed as

$$D(\mathbf{x}_g;\mathbf{x}_s,\omega) = s(\omega)\int_V k_0^2 G(\mathbf{x}';\mathbf{x}_s,\omega) M(\mathbf{x}') G(\mathbf{x}';\mathbf{x}_g,\omega) d\mathbf{x}', \tag{5.1}$$

where $M(\mathbf{x}') = \delta c(\mathbf{x}')/c(\mathbf{x}')$ is the velocity perturbation; $k_0 = \omega/c_0(\mathbf{x}')$ is the background wavenumber; $c_0(\mathbf{x}')$ is the local background velocity. $s(\omega)$ is the source spectrum; $G(\mathbf{x}';\mathbf{x}_s,\omega)$ is the Green's function from shot location $\mathbf{x}_s$ to the target location $\mathbf{x}'$; $G(\mathbf{x}';\mathbf{x}_g,\omega)$ is the Green's function from geophone location $\mathbf{x}_g$ to target location $\mathbf{x}'$. The reciprocity $G(\mathbf{x}';\mathbf{x}_g,\omega) = G(\mathbf{x}_g;\mathbf{x}',\omega)$ is used here.

For a system composed of multiple shots and geophones, the image can be formed by

$$I(\mathbf{x},\omega) = \sum_{\mathbf{x}_s} s(\omega) G(\mathbf{x};\mathbf{x}_s,\omega)\left[\sum_{\mathbf{x}_g} D^*(\mathbf{x}_g;\mathbf{x}_s,\omega)\frac{\partial}{\partial n} G(\mathbf{x};\mathbf{x}_g,\omega)\right], \tag{5.2}$$

Substituting $D(\mathbf{x}_g;\mathbf{x}_s,\omega)$ with equation 1 will result in

$$I(\mathbf{x},\omega) = \int_V M(\mathbf{x}') R(\mathbf{x},\mathbf{x}',\omega) d\mathbf{x}', \tag{5.3}$$

where

$$\begin{aligned} R(\mathbf{x},\mathbf{x}',\omega) &= k_0^2 s(\omega) s^*(\omega) \\ &\sum_{\mathbf{x}_s}\sum_{\mathbf{x}_g} G(\mathbf{x};\mathbf{x}_s,\omega) G^*(\mathbf{x}';\mathbf{x}_s,\omega) G^*(\mathbf{x}';\mathbf{x}_g,\omega)\frac{\partial}{\partial n} G(\mathbf{x};\mathbf{x}_g,\omega), \end{aligned} \tag{5.4}$$

is called resolution operator. In this equation, two Green's functions involve in generating the data and two involve in the migration process. The image can be considered as the convolution of the resolution operator and the model parameter. In other words, the resolution operator maps a point scatter from the model space to the image space. It is also called the point spreading function (PSF) which includes the effects of both the acquisition (modeling) and inversion (imaging) processes (Wu et al., 2006).

The convolution in space domain corresponds to the multiplication in wavenumber domain. Thus equation 5.3 can be expressed as (Xie et al., 2005; Xie et al., 2006)

$$I\left(\mathbf{k}_d, \mathbf{x}, \omega\right) = M\left(\mathbf{k}_d, \mathbf{x}\right) R\left(\mathbf{k}_d, \mathbf{x}, \omega\right), \tag{5.5}$$

where $\mathbf{k}_d = k_d \hat{\mathbf{e}}_d$ is the wavenumber with k_d as its absolute value and $\hat{\mathbf{e}}_d$ as the unit vector related to the structure dips. For image I, model M and resolving kernel R, their space-domain representations and wavenumber-domain representations can be expressed as

$$I\left(\mathbf{k}_d, \mathbf{x}, \omega\right) = \int W\left(\mathbf{x}' - \mathbf{x}\right) I\left(\mathbf{x}', \omega\right) e^{-i\mathbf{k}_d\left(\mathbf{x}'-\mathbf{x}\right)} d\mathbf{x}', \tag{5.6}$$

$$R\left(\mathbf{k}_d, \mathbf{x}, \omega\right) = \int W\left(\mathbf{x}' - \mathbf{x}\right) R\left(\mathbf{x}, \mathbf{x}', \omega\right) e^{-i\mathbf{k}_d\left(\mathbf{x}'-\mathbf{x}\right)} d\mathbf{x}', \tag{5.7}$$

$$M\left(\mathbf{k}_d, \mathbf{x}\right) = \int W\left(\mathbf{x}' - \mathbf{x}\right) M\left(\mathbf{x}'\right) e^{-i\mathbf{k}_d\left(\mathbf{x}'-\mathbf{x}\right)} d\mathbf{x}'. \tag{5.8}$$

Note, the space sampling window W indicates all these quantities are localized.

All the following equations are derived in 2D scheme. Suppose f is an arbitrary space-domain function, we define its angle component $f(\theta)$ in

$$\int f(\mathbf{k})\,d\mathbf{k} = \int f(\theta)\,d\theta. \tag{5.9}$$

So that

$$f(\theta) = \int f(k,\theta)\,k\,dk, \tag{5.10}$$

where k and θ are the length and polar angle of wavenumber vector $\mathbf{k}$, respectively.

The dip component of the model parameter is

$$M(\theta_d,\mathbf{x}) = \int M(k_d,\theta_d,\mathbf{x})\,k_d\,dk_d, \tag{5.11}$$

where $M(\mathbf{k}_d,\mathbf{x})$ or $M(k_d,\theta_d,\mathbf{x})$ is the localized spectrum of the model defined at $\mathbf{x}$ and its vicinity, and θ_d is the local target dip. For a scattering point, i.e., a spatial delta function, its spectrum $M(k_d,\theta_d,\mathbf{x}) \sim$ constant. For a locally planar dipping structure whose dip is given by θ_n, its spectrum $M(k_d,\theta_d,\mathbf{x}) \sim \delta(\theta_d - \theta_n)$. No matter which type of model is used, $M(k_d,\theta_d,\mathbf{x})$ is independent of k_d, so it can be taken out from the integral. A structure characterized by spatial wavenumber $\mathbf{k}_d$ can be detected by a pair of source-receiver waves (Figure 5.1) satisfying the condition

$$\mathbf{k}_d = \mathbf{k}_s + \mathbf{k}_g, \tag{5.12}$$

where $\mathbf{k}_s = k_s\hat{\mathbf{e}}_s$ and $\mathbf{k}_g = k_g\hat{\mathbf{e}}_g$ are the wavenumbers of source- and receiver-side waves, in which k_s and k_g are their absolute values and $\hat{\mathbf{e}}_s$ and $\hat{\mathbf{e}}_g$ are their unit vectors, respectively. Since $k_s = k_g = k_0$, a mono-frequency wave can detect the local structure whose spectrum is from zero up to $2k_0$.

$$M(\theta_d, \mathbf{x}) = M(k_d, \theta_d, \mathbf{x}) \int_0^{2k_0} k_d dk_d \, . \tag{5.13}$$

Thus we have

$$M(k_d, \theta_d, \mathbf{x}) = \frac{1}{2k_0^2} M(\theta_d, \mathbf{x}) \, . \tag{5.14}$$

Substituting equation 5.14 into equation 5.5 yields

$$I(k_d, \theta_d, \mathbf{x}, \omega) = \frac{1}{k_0^2} M(\theta_d, \mathbf{x}) R(k_d, \theta_d, \mathbf{x}, \omega) \, . \tag{5.15}$$

Note that the constant in equation 5.14 is removed because a relative reflectivity is needed.

Following the definition in equation 5.10, we integrate equation 5.15 over k_d in the polar coordinate and end up with

$$I(\theta_d, \mathbf{x}, \omega) = \frac{1}{k_0^2} M(\theta_d, \mathbf{x}) R(\theta_d, \mathbf{x}, \omega) \, , \tag{5.16}$$

Then we integrate equation 5.16 over the frequency and get the equation as below

$$I(\theta_d, \mathbf{x}) = M(\theta_d, \mathbf{x}) A(\theta_d, \mathbf{x}) \, , \tag{5.17}$$

where

$$I(\theta_d, \mathbf{x}) = \int I(\theta_d, \mathbf{x}, \omega) d\omega \, , \tag{5.18}$$

$$A(\theta_d, \mathbf{x}) = \int \frac{1}{k_0^2} R(\theta_d, \mathbf{x}, \omega) d\omega \, , \tag{5.19}$$

where $I(\theta_d, \mathbf{x})$ and $A(\theta_d, \mathbf{x})$ are 2D common dip image (CDI) and acquisition dip response (ADR), respectively.

To sum up all the dip angle components, we obtain the space-domain model parameter.

$$M(\mathbf{x}) = \int \frac{I(\theta_d, \mathbf{x})}{A(\theta_d, \mathbf{x})} d\theta_d \ , \tag{5.20}$$

In the following sections, we will describe how to calculate $I(\theta_d, \mathbf{x})$ and $A(\theta_d, \mathbf{x})$.

5.4 IMAGE DECOMPOSITON

The common dip image (CDI) can be efficiently calculated at the post imaging stage. In 2D case, CDI is expressed as

$$I(\theta_d, \mathbf{x}) = \int I(k_d, \theta_d, \mathbf{x}) k_d dk_d \ , \tag{5.21}$$

where $I(k_d, \theta_d, \mathbf{x})$ can be obtained by decomposing migration image with local slant stacking:

$$I(k_d, \theta_d, \mathbf{x}) = \int W(\mathbf{x}' - \mathbf{x}) I(\mathbf{x}') e^{-i\mathbf{k}_d \cdot (\mathbf{x}' - \mathbf{x})} d\mathbf{x}' \ , \tag{5.22}$$

where $W(\mathbf{x}' - \mathbf{x})$ is a local spatial window function centered at $\mathbf{x}$ and $I(\mathbf{x})$ is the final stacked migration image.

5.5 AMPLITUDE CORRECTION FACTOR

5.5.1 Acquisition dip response (ADR)

Since $\mathbf{k}_d$ is closely related to $\mathbf{k}_s$ and $\mathbf{k}_g$, we start from equation 5.5 and expand it by $\mathbf{k}_s$ and $\mathbf{k}_g$:

$$R\left(\mathbf{k}_s,\mathbf{k}_g,\mathbf{x},\omega\right)=k_0^2 s(\omega)s^*(\omega)$$
$$\sum_{\mathbf{x}_s}\sum_{\mathbf{x}_g} G\left(\mathbf{k}_s,\mathbf{x};\mathbf{x}_s,\omega\right)G^*\left(\mathbf{k}_s,\mathbf{x};\mathbf{x}_s,\omega\right)G^*\left(\mathbf{k}_g,\mathbf{x};\mathbf{x}_g,\omega\right)\frac{\partial}{\partial n}G\left(\mathbf{k}_g,\mathbf{x};\mathbf{x}_g,\omega\right) \quad ,(5.23)$$

where $G\left(\mathbf{k}_s,\mathbf{x};\mathbf{x}_s,\omega\right)$ and $G\left(\mathbf{k}_g,\mathbf{x};\mathbf{x}_g,\omega\right)$ are the wavenumber components of incident wave (source-side Green's function) and scattered wave (receiver-side Green's function).

We integrate equation 5.23 over k_s and k_g in the polar coordinate

$$R\left(\theta_s,\theta_g,\mathbf{x},\omega\right)=\int R\left(\mathbf{k}_s,\mathbf{k}_g,\mathbf{x},\omega\right)k_s dk_s k_g dk_g, \qquad (5.24)$$

where θ_s and θ_g are the polar angles of $\mathbf{k}_s$ and $\mathbf{k}_g$. Physically, they are the propagation angles of source and receiver waves when approaching the image point $\mathbf{x}$. As mentioned before, $k_s = k_g = k_0$. It is equivalent to the introduction of $\delta\left(k_s-k_0\right)\delta\left(k_g-k_0\right)$ to the integral

$$R\left(\theta_s,\theta_g,\mathbf{x},\omega\right)=\int \delta\left(k_s-k_0\right)\delta\left(k_g-k_0\right)R\left(\mathbf{k}_s,\mathbf{k}_g,\mathbf{x},\omega\right)k_s dk_s k_g dk_g. \quad (5.25)$$

It results in

$$R\left(\theta_s,\theta_g,\mathbf{x},\omega\right)=k_0^4 s(\omega)s^*(\omega)$$
$$\sum_{\mathbf{x}_s}\sum_{\mathbf{x}_g} G(\theta_s,\mathbf{x};\mathbf{x}_s,\omega)G^*(\theta_s,\mathbf{x};\mathbf{x}_s,\omega)G^*\left(\theta_g,\mathbf{x};\mathbf{x}_g,\omega\right)\frac{\partial}{\partial n}G\left(\theta_g,\mathbf{x};\mathbf{x}_g,\omega\right), \tag{5.26}$$

where $G(\theta_s,\mathbf{x};\mathbf{x}_s,\omega)$ and $G\left(\theta_g,\mathbf{x};\mathbf{x}_g,\omega\right)$ are the local incident and scattered plane waves, respectively. They can be obtained by local slant stacking (Xie and Wu, 2002; Xie and Yang, 2008; Yan and Xie, 2012)

$$G(\theta,\mathbf{x},\omega)=\int W(\mathbf{x}'-\mathbf{x})G(\mathbf{x}',\omega)e^{-ik_0\hat{\mathbf{e}}_\theta(\mathbf{x}'-\mathbf{x})}d\mathbf{x}', \tag{5.27}$$

where $W(\mathbf{x}'-\mathbf{x})$ is a local spatial window function centered at location $\mathbf{x}$, $G(\mathbf{x}',\omega)$ is the Green's function initiated at a shot location; $\hat{\mathbf{e}}_\theta$ is the unit vector specifying the propagation direction of the plane wave.

5.5.2 Coordinate transform

Given a pair of incident and scattering angles θ_s and θ_g, we can calculate the target dip angle θ_d and the reflection angle θ_r. In 2D case,

$$\theta_d=\left(\theta_s+\theta_g\right)/2. \tag{5.28}$$

$$\theta_r=\left(\theta_s-\theta_g\right)/2, \tag{5.29}$$

With the equations above, the representation can be transformed from $R\left(\theta_s,\theta_g,\mathbf{x},\omega\right)$ to $R(\theta_r,\theta_d,\mathbf{x},\omega)$. For a given dip angle θ_d, summing up all the reflection-angle components will lead to the acquisition dip response (ADR)

$$R\left(\theta_d,\mathbf{x},\omega\right)=\int R\left(\theta_r,\theta_d,\mathbf{x},\omega\right)d\theta_r. \tag{5.30}$$

For commonly used seismic source functions such as the Ricker wavelet, the major energy is carried by waves near the dominant frequency. The CDI is obtained from the final stack image, which approximately has the resolution of $2k_0$ (k_0 is the wavenumber corresponding to the dominant frequency). Therefore, ADR at the dominant frequency is a good approximation of amplitude correction factor:

$$A(\theta_d, \mathbf{x}) = \frac{1}{k_0^2} R(\theta_d, \mathbf{x}, \omega_0), \tag{5.31}$$

where ω_0 is the dominant frequency of the source.

5.5.3 Computational issues on ADR calculation

The major factors affecting the cost of the ADR computation include the numbers of shots and geophones, the size of the velocity model and the number of dip angle θ_d .A full scale calculation is extremely expensive, particularly for 3D case. Therefore to turn this method into practical application, it is crucial that we can reduce the computation cost while retaining the reasonable accuracy.

Equation 5.26 requires calculating Green's functions for all shot/geophone pairs in the acquisition system. This involves great redundancies which can be potentially reduced. First, in an image process, the phase information is very important. To reduce the aliasing, we have to use dense source and receiver arrays to meet the spatial sampling requirement. However, for the ADR calculation, only the amplitude (or energy) is required. To save computational cost, we can use much coarse source and receiver arrays. Second, in the marine acquisition, from one shot to the next, most of the geophone positions are revisited, leaving some non-coincident geophones at the beginning and some at the end. The repetitive computation can be avoided if we reuse the geophones matched with the previous shot, and only subtract or add the geophones that are not overlapping with those of the previous one.

The model size for ADR computation can be reduced as well. The resolution function is a slow-varying function compared to the image. Thus it is not necessary to calculate the ADR using the same density as the image. Instead, we calculate the ADR at a sparse grid and the grid space can be as large as one wavelength. The values at other image points can be obtained through interpolation.

5.6 NUMERICAL EXAMPLES

In the first example, we use a simple five layer model (shown in Figure 5.2a) to test the accuracy of the amplitude correction. To generate the synthetic data, 201 surface shots are used and the source interval is 0.05 km. Each shot is equipped with 201 double-side receivers with a maximum offset of 2 km. The source time function is a 20 Hz Ricker wavelet. Figure 5.2b is the conventional RTM image. As a comparison, shown in Figure 5.3 is the RTM image compensated by the energy of the source wavefield. Superimposed on the image are vertical profiles of the image amplitude and the true reflectivity. Although the image amplitudes on near horizontal sections agree well with the true reflectivity, there are apparent discrepancies on steep sections. Figure 5.4 compares the RTM image compensated by the ADR with the true reflectivity. Even for reflectors with variable dip angles, the image amplitudes are almost constant. Figure 3 and 4 demonstrate that the correct illumination correction not only depends on the source side illumination but also depends on the receiver side illumination and the target dip angle.

Next we conduct the amplitude correction on 2D SEG/EAGE salt model (Figure 5.5a). The observation system for the model is composed of 325 shots with an interval of 160 feet. Each shot is matched with 176 left-side receivers separated by 80 feet. Figure 5.5b shows the conventional RTM image. Figure 5.6 shows the source illumination and the image corrected by the source illumination. Though the amplitudes of the image are more balanced than the conventional image, it ignores the propagation effects from the target to the geophones as well as the aperture effects. We decompose the stacked migration image into 24 CDIs and show four samples in Figure 5.7. Figure 5.8 displays the corresponding ADRs for the selected dips. By comparing the CDIs and ADRs, we notice that the deviation of the image amplitude from the true reflectivity is largely controlled by the ADR. We correct individual CDIs with the ADRs and the results are shown in Figure 5.9. Then all the corrected images are summed up to form the final image which is shown in Figure 5.10. After the correction, the image amplitudes of reflectors with different dipping angles become more balanced and the structures appear more continuous. The subsalt structures are greatly enhanced, particularly for steep structures. Superimposed on the image are the image amplitude and the true reflectivity. They match with each other very well.

5.7 DISCUSSIONS

Traditionally, the amplitude corrections (Gelius et al., 2002; Lecomte et al., 2003; Xie et al., 2005) are conducted in the $\mathbf{k}_d$ -domain. For the proposed method, the calculation is between the CDI and ADR in the θ_d -domain. Compared with the original implementation, the proposed method is more feasible because less computation costs and disk storages are involved. For 2D case, it takes the several times of as the conventional RTM.

Theoretically, to recover the model structure from the image, the calculation should be conducted in the $\mathbf{k}_d$ -domain, i.e., a scale length is involved. However, for structures which are infinitely sharp, e.g., an ideal point scatter or a sharp planar reflector, their local spectra are constant over k_d so there is no characteristic scale involved. For a real model, as long as the structure is sharp enough, i.e., its local spectrum is nearly constant up to the detecting power of the source wavelet, the characteristic scale can be neglected. This is the theoretical basis for correcting the image in dip angle domain instead of in wavenumber domain. Similar techniques can also be used to improve the AVA measurement.

5.8 CONCLUSIONS

We formulate the true-amplitude imaging as a process of conventional RTM plus a post-image amplitude correction in the dip angle domain. The correction is based on the resolution operator which accounts for the target illumination. The overburden velocity structure, the acquisition geometry and the target dipping angle are the most important factors affecting the amplitude correction. Both the migration image and Green's function are decomposed into the angle domain using local slant stacking. The ADR, which is derived from the resolution operator, is constructed with the decomposed Green's functions. In the dip-angle domain, the CDIs are corrected with the ADRs and then are stacked to obtain the final image. Compared to the compensation with source illumination, ADR correction shows significant improvement in image amplitude. The efficient algorithms are proposed to make the algorithm practical. The theoretical derivations can be easily extended from 2D to 3D case and can be implemented in a target-oriented fashion.

5.9 REFERENCES

Audebert, F., P. Froidevaux, H. Rakotoarisod, and J. Svay-Lucas, 2002, Insights into migration in the angle domain: 72nd Annual International Meeting, SEG, Expanded Abstracts, 1188–1191.

Bleistein, N., 1987, On the imaging of reflectors in the earth: Geophysics, 52, 931–942.

Brandsberg-Dahl, S., M. de Hoop, and Ursin, B., 2003, Focusing in dip and AVA compensation on scattering-angle/azimuth common image gathers: Geophysics, 68(1), 232–254.

Cao, J., and R. S. Wu, 2005, Influence of propagator and acquisition aperture on image amplitude: 75th Annual International Meeting, SEG, Expanded Abstracts, 1946–1949.

Cao, J., and R. S. Wu, 2008, Amplitude compensation for one-way wave propagators in inhomogeneous media and its application to seismic imaging: Communications in Computational Physics, 3, 203–221.

Cao, J., and R. S. Wu, 2009, Fast acquisition aperture correction in prestack depth migration using beamlet decomposition: Geophysics, 74(4), S67–S74.

Gelius, L. J., I. Lecomte, and H. Tabti, 2002, Analysis of the resolution function in seismic prestack depth imaging: Geophysical Prospecting, 50, 505–515.

Guitton, A., 2004, Amplitude and kinematic corrections of migrated images for nonunitary imaging operators: Geophysics, 69, 1017–1024.

Hanitzsch, C., 1995, Amplitude preserving prestack Kirchhoff depth migration/inversion in laterally inhomogeneous media: Ph.D. dissertation, University of Karlsruhe.

Hu, J., G. T. Schuster, and P. Valasek, 2001, Poststack migration deconvolution, Geophysics, 66(3), 939–952.

Hubral, P., M. Tygel, and H. Zien, 1991, Three-dimensional true-amplitude zero-offset migration: Geophysics, 56(1), 18–26.

Jin, S., M. Luo, S. Xu, and D. Walraven, 2006, Illumination amplitude correction with beamlet migration: The Leading Edge, 25(9), 1046–1050.

Lecomte, I., I. H. Gjoystdal, and A. Drottning, 2003, Simulated Prestack Local Imaging: a robust and efficient interpretation tool to control illumination, resolution, and time-lapse properties of reservoirs: 73rd Annual International Meeting, SEG, Expanded Abstracts, 1525-1528.

Lecomte, I., 2008, Resolution and illumination analyses in PSDM: A ray-based approach: The Leading Edge, 27(5), 650–663.

Mao, J. and R. S. Wu, 2010, Target oriented 3D acquisition aperture correction in local wavenumber domain: 80th Annual International Meeting, SEG, Technical Program Expanded Abstracts, 3237-3241.

Plessix, R.E. and W. A. Mulder, 2004, Frequency-domain finite-difference amplitude-preserving migration: Geophys. J. Int., 157, 975-987.

Rickett, J. E., 2003, Illumination-based normalization for wave-equation depth migration: Geophysics, 68(4), 1371-1379.

Tarantola, A., 1987, Inverse problem theory: Methods for data fitting and model parameter estimation: Elsevier Science Publication Company, Inc.

Ursin, B., 1983, Review of elastic and electromagnetic wave propagation in horizontally layered media: Geophysics, 48, 1063-1081.

Valenciano, A. A., B. Biondi, and A. Guitton, 2006, Target-oriented wave-equation inversion: Geophysics, 71, A35-38.

Valenciano, A. A., L. Biondo, R. G. Clapp, 2009, Imaging by target-oriented wave-equation inversion: Geophysics, 74, WCA109-WCA120.

Wu, R.S., and J. Cao, 2005, WKBJ Solution and Transparent Propagators, 67th Annual Meeting, EAGE, Extended Abstracts, P167.

Wu, R. S., and M. Q. Luo, 2005, Comparison of different schemes of image amplitude correction in prestack depth migration: 75th Annual International Meeting, SEG, Expanded Abstracts, 2060–2063.

Wu, R. S., M. Q. Luo, S. C. Chen, and X. B. Xie, 2004, Acquisition aperture correction in angle-domain and true-amplitude imaging for wave equation migration: 74th Annual International Meeting, SEG, Expanded Abstracts, 937–940.

Wu, R.S., X. B. Xie, M. Fehler, and L. J. Huang, 2006, Resolution analysis of seismic imaging: 68th Annual International Meeting, EAGE, Expanded Abstracts.

Xie, X. B. and R. S. Wu, 2002, Extracting angle related image from migrated wavefield, 72nd Annual International Meeting, SEG, Expanded abstracts , 1360-1363.

Xie, X.B., S. Jin, and R. S. Wu, 2006, Wave-equation based seismic illumination analysis: Geophysics, 71, No 5, S169-177

Xie, X. B., and H. Yang, 2008, A full-wave equation based seismic illumination analysis methods: 70th Annual International Meeting, EAGE, Expanded Abstract, P284.

Xie, X.B., R.S., Wu, M. Fehler and L. Huang, 2005, Seismic resolution and illumination: A wave-equation-based analysis, 75th Annual International Meeting, SEG, Expanded Abstracts, 1862-1865.

Xu, S., H. Chauris, G. Lambaré, and M. Noble, 2001, Common-angle migration: A strategy for imaging complex media: Geophysics, 66(6), 1877–1894.

Yan, R. and X. B. Xie, 2012, An angle-domain imaging condition for elastic reverse time migration and its application to angle gather extraction: Geophysics, 77, No 5, S105–S115.

Zhang Y., G. Zhang, and N. Bleistein, 2003, True amplitude wave equation migration arising from true amplitude one-way wave equations: Inverse Problems 19, 1113-1138.

Zhang Y., G. Zhang G. and N. Bleistein, 2005, Theory of true-amplitude one-way wave equations and true-amplitude common-shot migration: Geophysics 70(4), E1–E10.

5.10 FIGURES AND TABLES

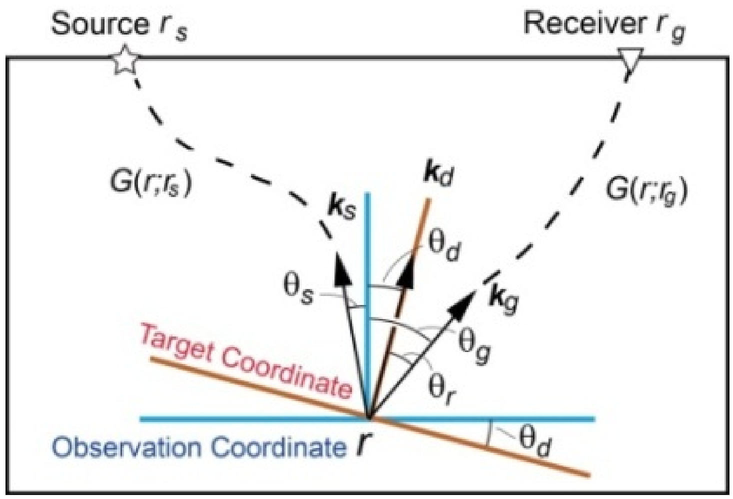

Figure 5.1 The coordinate system used in angle-domain analysis.

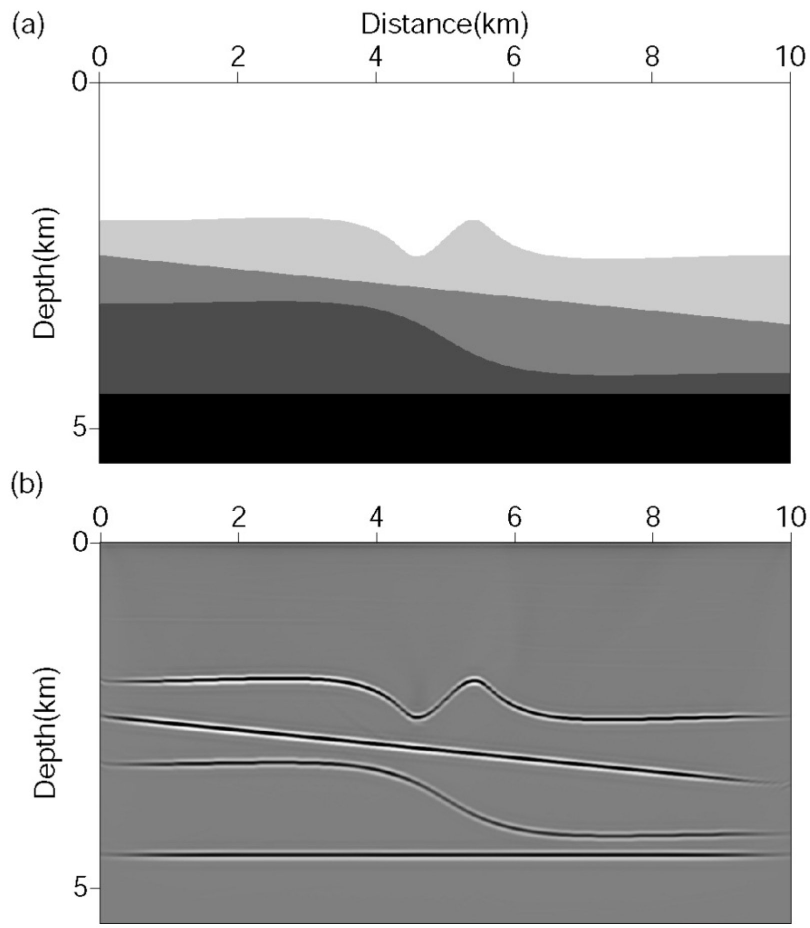

Figure 5.2 (a) The 5-layer velocity model, and (b) the conventional RTM image.

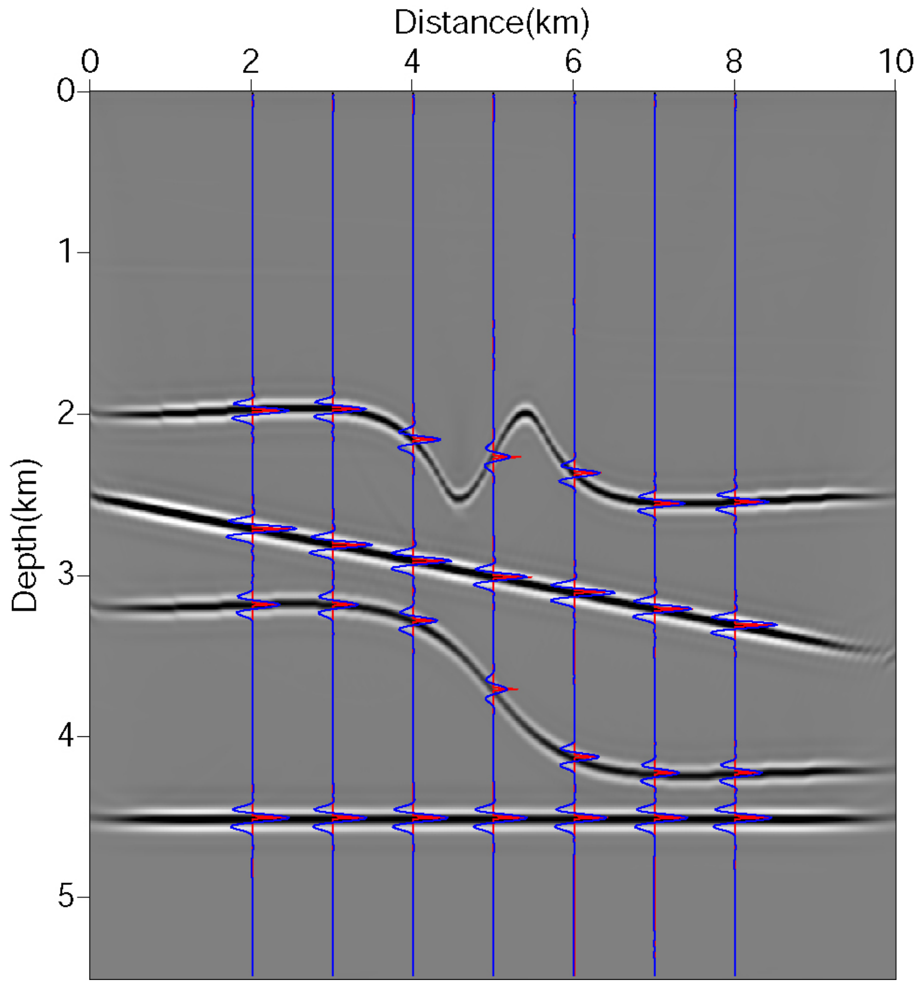

Figure 5.3 The migration image compensated by the source illumination (the energy of source-side wavefields). Superimposed wiggles are the reflectivity (red) and the image amplitude (blue).

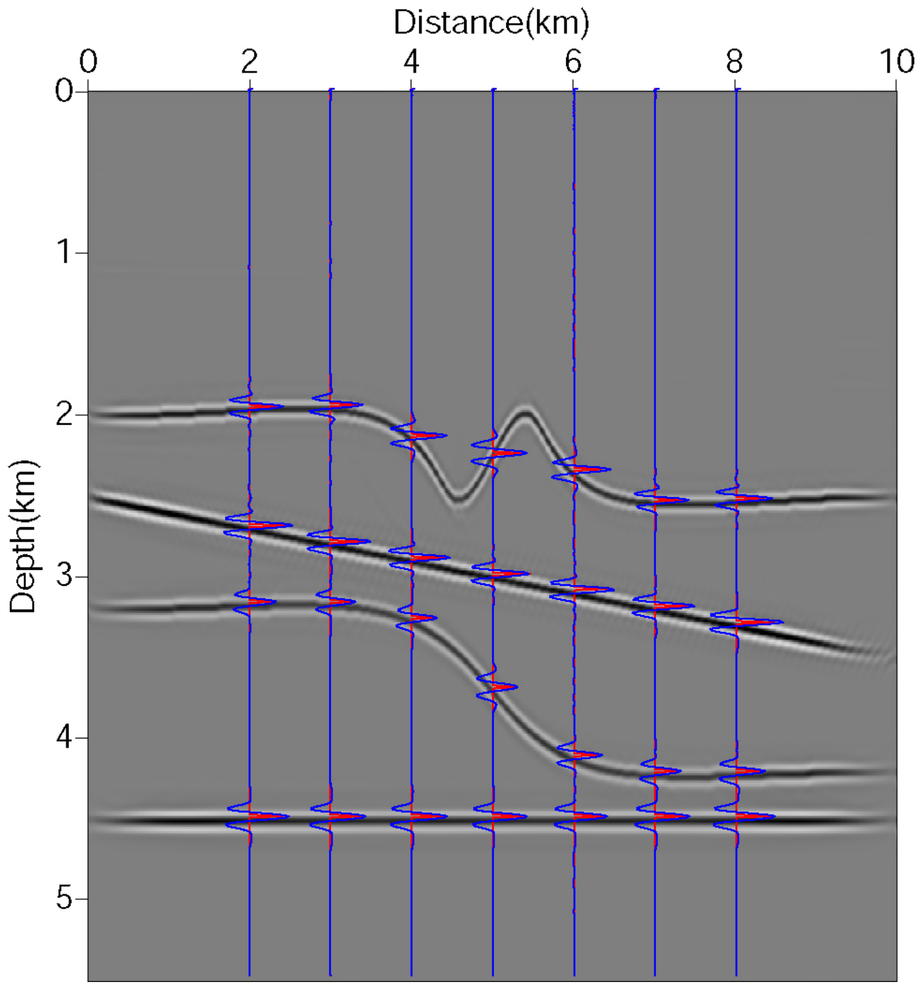

Figure 5.4 The migration image compensated by the ADR. Superimposed are the reflectivity (red) and the image amplitude (blue).

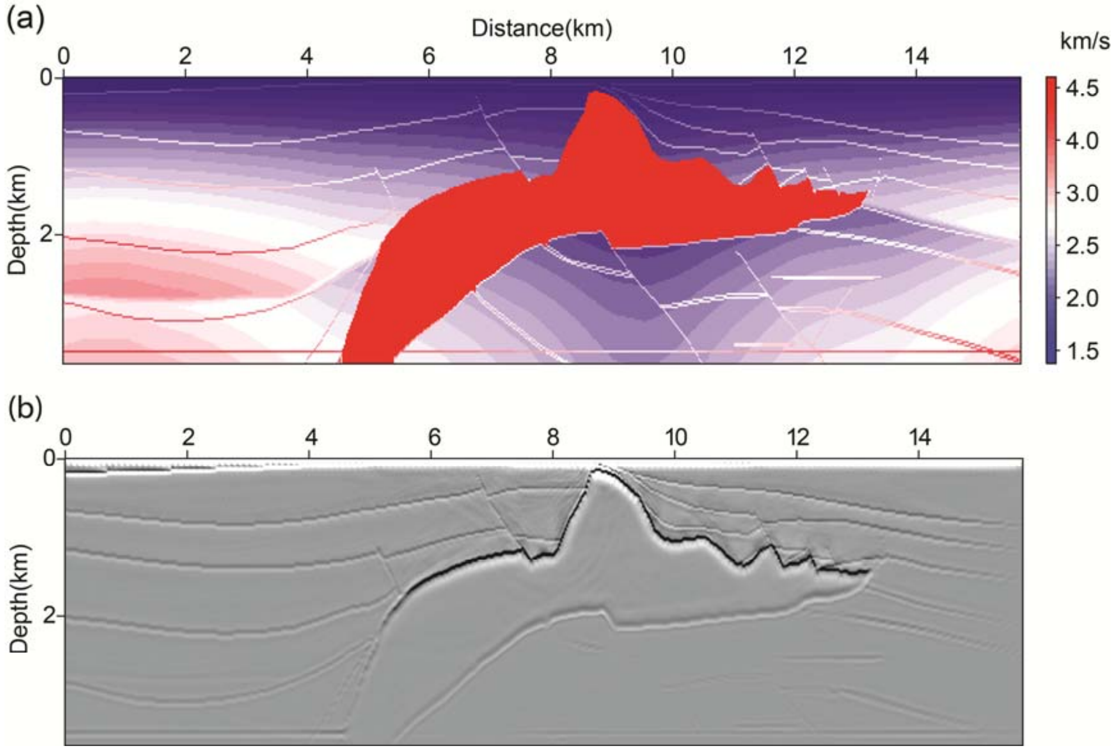

Figure 5.5 (a) The 2D SEG/EAGE salt model. (b) the conventional migration image.

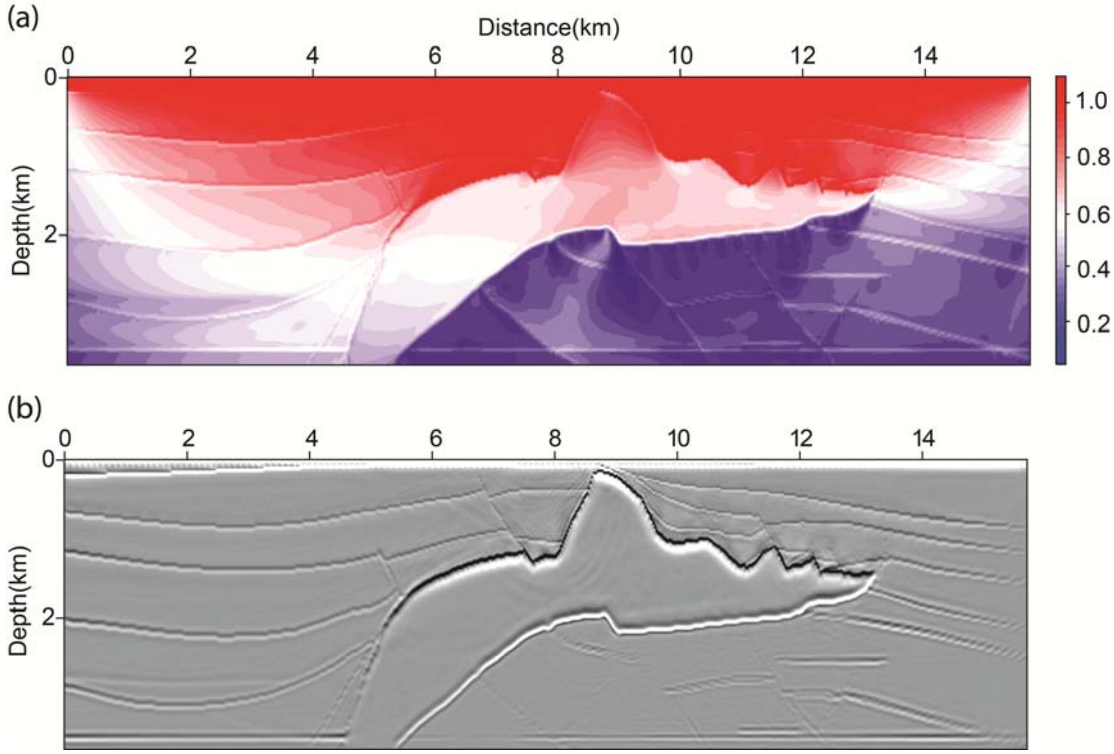

Figure 5.6 (a) source illumination (the energy of source-side wavefields) and (b) image compensated by the source illumination.

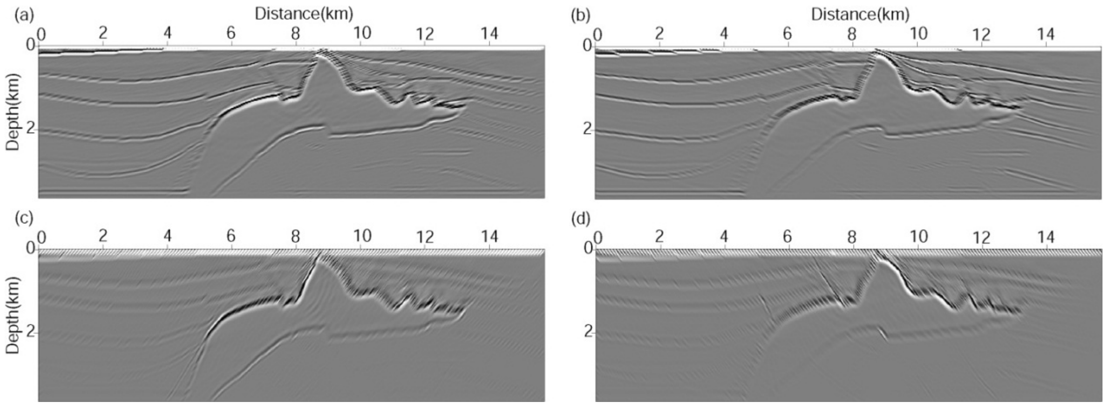

Figure 5.7 CDIs for selected dip angles with (a) -15º, (b) 15º, (c) -45º and (d) 45º.

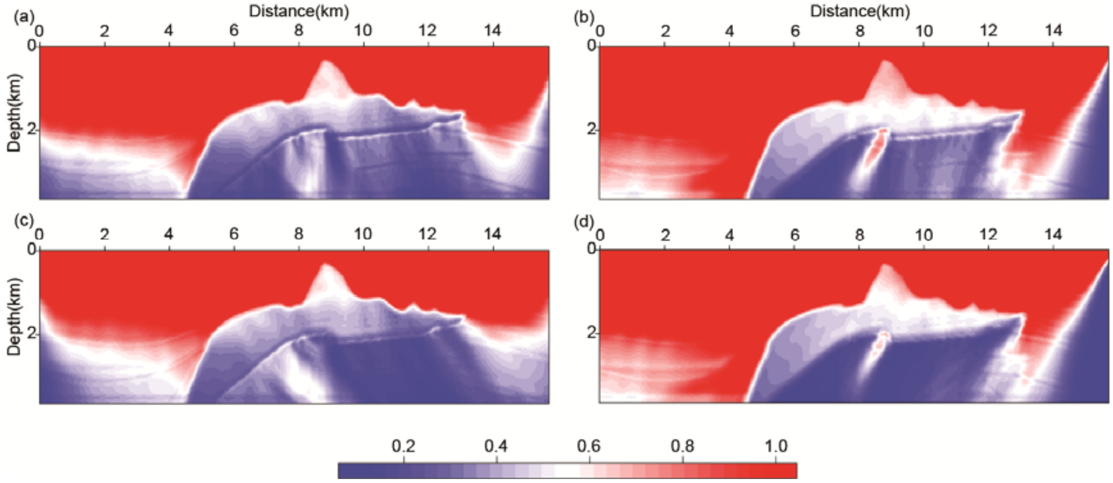

Figure 5.8 ADR (acquisition dip response) for selected dip angles with (a) -15º, (b) 15º, (c) -45º and (d) 45º.

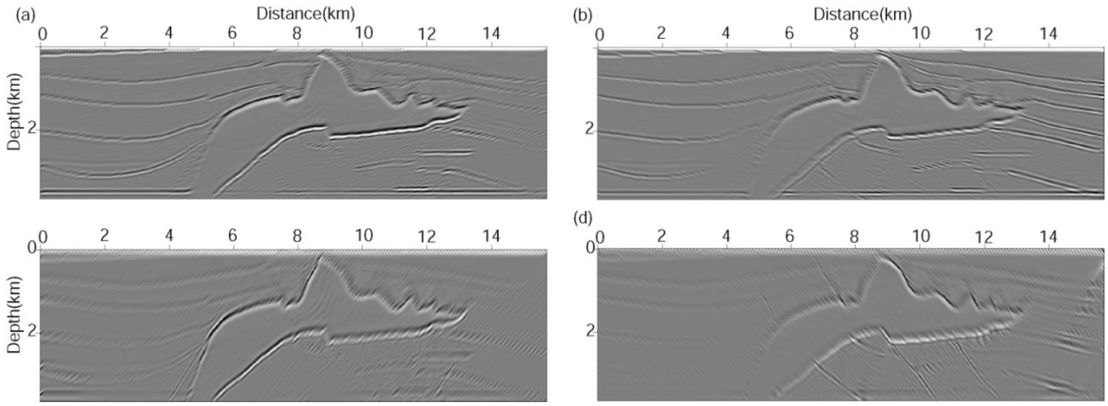

Figure 5.9 The corrected CDIs for selected dip angles with (a) -15º, (b) 15º, (c) -45º and (d) 45º.

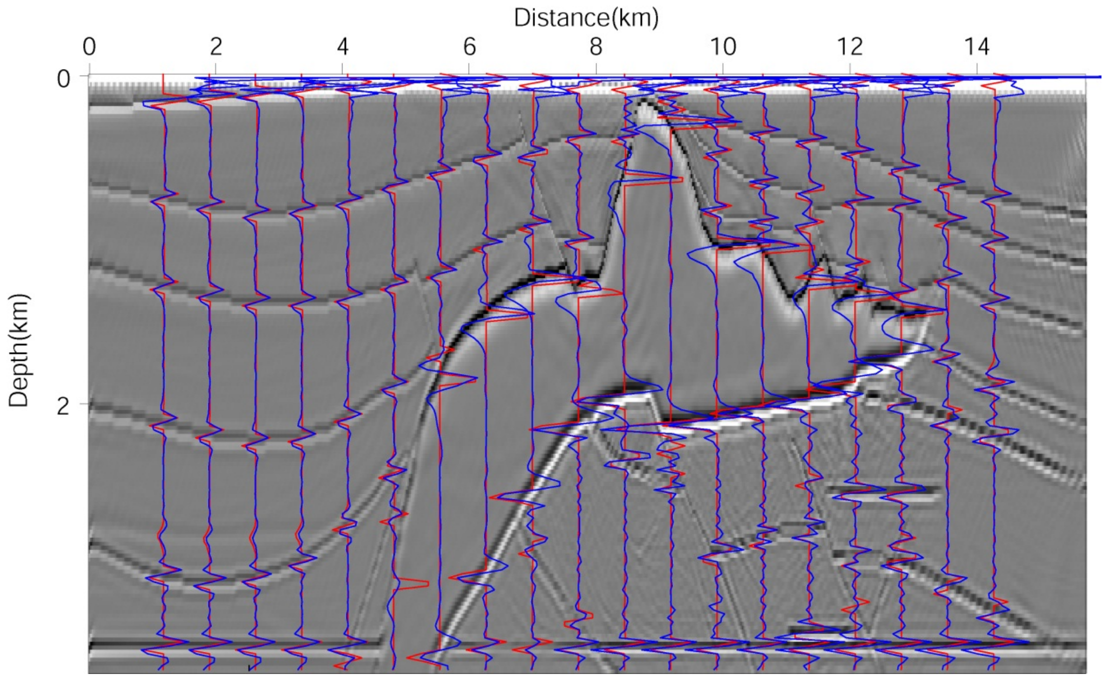

Figure 5.10 The migration image compensated by the ADR. Superimposed are the reflectivity (red) and the image amplitude (blue).

6 A PRELIMINARY STUDY ON SUBSALT IMAGING USING CONVERTED-PATH MIGRATION

6.1 SUMMARY

We carry out some quantitative studies on a simple salt model to examine the feasibility of using converted waves for subsalt imaging. The survey efficiencies of Converted-path (C-path) are evaluated in terms of open angle at the subsalt target, surface offset and the target dip. The analyses validate the idea of C-path imaging, in which the migration path is controlled by switching on/off mode conversion at the salt boundary, and provide some hints on C-path selection. Numerical examples demonstrate the benefit of C-path imaging. It eliminates the blind area for steep subsalt faults having dip larger than the critical angle (37º) created by P-wave migration. Compared with conventional elastic RTM, C-path imaging effectively remove certain migration artifacts caused by mismatches between the data path and migration path.

6.2 INTRODUCTION

Large hydrocarbon deposits are often associated with the presence of salt structures due to favorable conditions for accumulation and trapping of oil and gas, thus it is very important to be able to image the subsalt prospects correctly. However, due to the huge velocity contrast between the sediments and salt bodies, the P-wave path can only pass through the salt bodies within the range of critical incidence, and the waves beyond the critical angle are completely blocked, resulting in various shadow zones (or blind areas) for subsalt imaging. Converted-paths (C-paths), including P-waves and S-waves undergoing one or more mode conversions along the path from source to receiver, can penetrate high-velocity salt structure with much less defocusing and traverse the shadow zone of P-wave survey.

There are some debates in the seismic exploration community on exploiting converted waves for subsalt imaging. Purnell (1992) used the physical modeling to produce more complete images of the sub-HVL (high velocity layer) reflectors, especially high-dip ones, by exploiting waves that traveled at least once through the HVL in the S mode. Wu et al. (2001) applied the post-stack depth migration to synthetic data of the SEG/EAGE salt model generated by exploding reflector modeling method and obtained clear images of all the steep subsalt faults by assigning S-wave velocity to the salt and P-wave velocity to other regions. However, some scientists (e.g., Hanssen et al., 2000) claimed that the energy of converted wave is too weak to be utilized for subsalt or sub-basalt imaging. The situation of converted waves becomes even worse in reality due to the higher noise-to-signal ratio of seismic data. The difficulty in separating converted waves from multiples and other types of waves also impedes its applications.

Due to the difficulty to utilize converted waves, several authors have investigated various methods to enhance the imaging in some real cases. Kendall et al. (1998) processed 4-component data from Mahogany field using an anisotropic prestack depth migration and illustrated improved imaging of targets underlying a salt structure. Jones and Gaiser (1999) described their processing flow including multiple-suppression and mode-conversion-identification, followed by prestack depth migration, and identified the salt base and the possible subsalt structure in the migrated image.

This study investigates the possibility of using converted waves for subsalt imaging. First, we build an elastic model composed of a salt layer and some subsalt reflectors for numerical analysis. The energy partitioning of wave mode conversion at the subsalt target and wave transmission through the salt body are evaluated. The amplitudes and energy of converted waves are compared in terms of certain attributes, such as the open angle at the target and surface offset. We develop a hybrid propagator based on the reflection/transmission coefficient plus the Born approximation (R/T-Born propagator) as the modeling and migration operator and demonstrate the concept of elastic C-path migration. Secondly, we create some subsalt reflectors with variable dipping angles to investigate the illumination efficiency of different C-paths on these subsalt reflectors. The numerical examples demonstrate the benefit and limitation of C-path imaging.

6.3 TESTING C-PATH MODELING AND IMAGING FOR STEEP SUBSALT FAULTS IN LAYERED MODELS

A simple 2D salt model (Figure 6.1) is generated for numerical analysis. The background of the model contains three horizontal layers: the top and bottom layers are sediments and a salt layer is in the middle. The S-wave velocity of the salt is very close to the P-wave velocities in the sedimentary layers. Target objects are located beneath the salt layer, including a horizontal reflector with positive perturbation and a 45^0 dipping fault with negative perturbation. Even though the salt layer is not representative of real salt structures and scattering effects are substantially reduced for waves penetrating the salt body, the fundamental nature of mode conversion is preserved.

6.3.1 Mode conversion at the target

In this study, we are mainly concerned with subsalt faults which have great dips and weak velocity perturbations relative to the surrounding media. Thus they are almost invisible under conventional P-wave imaging. In the numerical model, the 45°-dipping fault is our focus. The energy partition between P and S scattering (reflection) on this 45°-dipping fault is shown in Figure 6.2 as a function of incident angle. We know that for these steep faults, the recorded P-to-S reflections from targets are mainly from near-normal incident waves due to the acquisition aperture limitation. For these near-normal events, their reflection angles (the angle between the incident direction and the reflector normal) are very small. Under this circumstance, the P-S conversion coefficient is much weaker than that of P-P reflection.

6.3.2 Energy partition of different C-Paths

Figure 6.3a and 6.3b show different paths of converted waves in penetrating the salt layer in Figure 6.2 and their energy transmission coefficients, respectively. Due to the huge velocity contrast between the sediments and salt bodies, the P-wave path can pass through the salt body only within the range of critical incidence and the waves beyond the critical angle (37º) are completely blocked, resulting in various shadow zones (or blind areas) for subsalt imaging. For small angles, the PPP and PPS paths carry most of the energy. However beyond the critical angle only the paths with an S-segment inside the salt body (paths PSP and PSS) can carry the energy through salt. This figure illustrates the basic concept of subsalt illumination with different C-paths.

6.3.3 The strength of the converted waves

In this simple case, we define C-path survey efficiency as two-way transmission ratio which can be theoretically computed as the product of all the transmission coefficients at the top and base of salt for the downgoing and upgoing paths. By integrating the C-path survey efficiency with the target reflection coefficient, we can calculate the strength of converted wave. Figure 6.4 shows a schematic diagram of six converted waves that are reflected from the 45º-dipping subsalt fault and received on the surface. The traveling paths are labeled with two legs such as PPP-PSP. The left leg (PPP) is the downgoing path and the right leg (PSP) is the upgoing leg. Not all the C-paths which provide illumination to the fault are plotted. I use those with upgoing path as PSP or PSS. Figure 6.5 illustrates the strength of the converted waves as a function of the open angle at the target, which is the sum of the incident angle and the scattering angle. The energy of path PPP-PSP/S (i.e. PPP-PSP and/or PPP-PSS) is zero at small open angles but peaks around 20^0; the energy of path PSP-PSP/S is less than half of the energy of path PPP-PSP/S and is mainly distributed at small open angle (-20^0-20^0); path PSS-PSP/S falls within the angle coverage of PPP-PSP/S but with smaller amplitude. Figure 6.6 shows the strength of the converted wave as a function of offset normalized by the depth. We see that path PPP-PSP/S has the greatest amplitude at zero offset. It spreads broadly over offset and still shows great efficiency at large offset; path PSP-PSP/S reaches to its peak at small offset but decreases rapidly as offset increases. Path PSS-PSP/S has maximum amplitude at medium offset, and also has wide offset spread. Generally, the converted waves involved with fewer mode conversions have larger amplitudes; the symmetric C-path mainly concentrates at the small offset and the asymmetric C-path has broad spread over the offset. Most of the converted waves which can effectively provide illumination to the steep subsalt fault have at least one S-leg in the salt. The energy analysis shows that S-waves received on the surface are stronger than P-waves. Thus multi-component seismic surveys capable of recording both P- and S-waves are preferred in elastic wave imaging or converted-path imaging.

6.3.4 Hybrid R/T-Born propagator

We use the simple salt model to demonstrate the idea and feasibility of converted-wave path (C-path) imaging. In the case of layered models, a hybrid reflection/transmission (R/T) – Born method was developed for both the modeling and migration. At both the top and base salt boundaries, the elastic transmission and reflection coefficients were calculated using the Zoeppritz equation (see Fuchs and Muller, 1971; Chapter 5, Aki and Richards, 1980; Muller, 1985), which can be considered as an exact one-way elastic propagator for the salt layer. For the case of subsalt faults which involve weak perturbations, the local Born approximation is utilized which includes incident field updating by the forward scattering (Wu and Aki, 1985; Wu, 1994; Wu, 1996; Wu et al., 2006). This hybrid method is considered an accurate elastic one-way propagator for this model. When the synthetic seismograms computed using the new hybrid method are compared to those generated by an elastic finite difference algorithm, excellent agreement is obtained. Figure 6.7 shows the comparison of the synthetic seismograms calculated by R/T method and those from the finite difference method for the background salt layer (where a and b are for horizontal and vertical components, respectively). Figure 6.8 gives the comparison of the seismograms calculated by the local elastic Born approximation and a finite difference method for the target reflectors (where a and b are for horizontal and vertical components, respectively). The background reflections are eliminated by setting all the reflection coefficients at the salt/sediment interfaces at zero during the simulations. For both methods, the salt response and the target scattering are in good agreement. The successful forward modeling allows us to use this propagator for the imaging. Figure 6.9 shows the synthetic seismograms for the model with reflections from the salt layer and reflections from the subsalt steep faults through different C-paths. This provides the physical basis for C-path migration for subsalt imaging.

6.3.5 Elastic converted-path migration

A seismic experiment is carried out with 41 shots starting at 2 km and spaced at 0.15 km. For each shot there are 500 receivers arranged in a fixed-spread configuration. The interval between receivers is 0.02 km. The seismic data is modeled with hybrid R/T-Born method. R/T propagator is utilized as the one-way elastic migration operator. This R/T operator has the flexibility of switching on/off for different elastic scattering modes among P-P, P-S, S-P and S-S at each sediment-salt interface. In this way, one can control the C-paths in the modeling and migration processes.

Figure 6.10 compares the conventional acoustic migration and elastic migration. To see the details of images, only the subsalt part of the image is shown in the figures. Figure 6.10a shows the image from the acoustic migration with the surface P-wave data. It is clear that pure P-wave migration has a blind zone for steep subsalt imaging (in this case, it is located for dip > 37^0). Figure 6.10b and 6.10c show the elastic RTM and the elastic migration with one-way R/T propagator. The three-component seismic data are migrated to the subsurface with all the wave paths switched on. Under this circumstance, the one-way result should be equivalent to the elastic RTM without considering the up-going waves. Regular imaging condition is applied to the migrated wavefields to generate the image. It can be expressed as the dot product of the source and receiver wavefields

$$I(\mathbf{r}) = \sum_{\omega} \mathbf{u}_S(\mathbf{r},\omega) \cdot \mathbf{u}_R^*(\mathbf{r},\omega), \tag{6.1}$$

where $\mathbf{u}_S(\mathbf{r},\omega)$ and $\mathbf{u}_R(\mathbf{r},\omega)$ are the vectorized source and receiver wavefields, respectively. Both of them are mixed with P and S modes. In this elastic migration, though the steep reflector clearly shows itself in the image, there are apparent artifacts alongside the reflector and it is difficult to distinguish between them.

To understand the artifacts generated by conventional elastic migration, it is instructive to show some examples of path mismatch (Figure 6.11). In all these examples, the seismic data are computed using hybrid R/T-Born modeling method but with the pre-designed path switched on. For testing purpose, it is possible to select P- or S-mode at the sediment/salt interface during modeling, but choose a different wave path during migration. In Figure 6.11a, the data path is PSP-PSP, but the migration path is PSS-PSP. In this case, the back-propagation leg in migration (PSS) is mismatched with the propagation leg in generating data (PSP), resulting in a false image of wrong location and dip. The second example (Figure 6.11b) shows the mismatch between PSS-PSP (signal) and PSP-PSP (migration). In the third example (Figure 6.11c), the path in the data is PPP-PSP, but the migration path is PSP-PSP. The resulting artifact is parallel to the true image but at a wrong location. All the mismatches between the data-path and migration-path produce false images as artifacts. In an ideal acquisition of 360^0 coverage, these mismatch-induced artifacts will be cancelled by interference. However, in the case of limited surface acquisition, these artifacts are inevitable.

If the migration operator (e.g., RTM) contains all the possible paths, the artifacts generated are difficult to identify and separate. But it is possible to reduce the artifacts by selecting C-path during migration. Figure 6.12 shows the migration results with a single path switched on. From top to the bottom, the migration path is PPP-PSP/S, PSP-PSP/S and PSS-PSP/S, respectively. PPP-PSP/S successfully separates the true image from the artifacts. Both the true image and the artifacts show similar amplitude in PSP-PSP/S image, and it is hard to distinguish them. PSS-PSP/S image is dominated by artifacts. While all those C-paths can provide illumination to the reflector, the best strategy of reducing artifacts is to select the one with the highest efficiency and switch off other paths which will not contribute much to the image, but generate strong noises.

In this section, we only focus on a steep reflector. By selecting certain C-paths during migration, most of artifacts can be avoided. But it may not be true if there are multiple reflectors with different dip angles located at the subsalt region. This will be discussed in the next section.

6.4 TESTING C-PATH MODELING AND IMAGING IN LAYER MODEL FOR SUBSALT FAULTS WITH DIFFERENT DIPS

6.4.1 The dip response of pure P-wave and C-paths for subsalt survey

It is interesting and instructive to evaluate C-path survey efficiency for subsalt reflectors having a full range of dips. The survey efficiency depends on both the target dip and the open angle of the target reflection. The dip response is defined as the maximal survey efficiency for a given dip. Figure 6.13 shows the dip response of pure P-path (PPP-PPP) and C-paths. The pure P-path carries substantial energy to illuminate the near horizontal reflector in the subsalt region but it is blind to the steeply dipping structure whose dip is larger than 37°. However, the C-paths can have much broader view angles. We only show the C-paths with P-P reflection at the subsalt region. Path PPP-PSP/S, PSP-PPP/S can image reflector with dip less than about 60°, and it can better image reflector with medium dip. Path PSP-PSP/S favors imaging reflector with dip around 0° and 45°. They can image a very broad range of dips in the subsalt region. This analysis is done for the ideal case, without taking account of aperture limitation on the surface. In reality, we need to check the effective acquisition aperture for the target area. For example, very large aperture is needed for path PSP-PSP/S to image horizontal reflector, but very small aperture to image the 45º-dipping reflectors. Overall, different C-paths can complement with each other in the dip coverage. However, the steeper reflector the path can image, the lower efficiency the path has. If different C-paths have distinct dip coverage, then no artifacts will be generated by the mismatch between data path and migration path. The overlap of the data path and migration path in dip coverage will inevitably introduce artifacts to the C-path image.

6.4.2 Elastic converted-path migration

In order to test the C-path imaging for multiple subsalt reflectors with different dips, a velocity model consisting of a salt layer embedded in the sedimentary background with three subsalt faults of 15°, 30° and 45° dips (Figure 6.14a) was constructed. The synthetic data were then migrated with the one-way hybrid R/T-Born propagator. Figure 14b gives the image using all the paths and regular elastic imaging condition (similar to the elastic RTM). Although all the subsalt faults are imaged, there are numerous artifacts (false images) which are hard to be distinguished from the real reflectors. The subsalt imaging is conducted individually by switching on C-paths without any S-segment in the salt, with one S-segment in the salt and two S-segments in the salt during migration, and the result is successively stacked to obtain the migration image. Figure 6.14c gives the PPP-PPP/S image. As expected, the steep fault of 45^0 is missing. Figure 6.14d gives the image which corresponds to path combination of PPP-PPP/S, PPP-PSP/S and PSP-PPP/S. The steep reflector is shown in the image but some artifacts are introduced to the image as well. Nevertheless, compared with the conventional elastic image, the artifacts are well controlled. Figure 6.14e shows the subsalt image with PSP-PSP/S stacked on. Extra artifacts are shown in the image but the true reflections remain unchanged. In fact, C-path migration cannot exclude all the mismatches and therefore cannot remove all the artifacts for complex models, but at least it helps to suppress the artifacts and enhance the true image.

6.5 CONCLUSIONS

Using a simple elastic model with salt layers and both flat and steep subsalt faults, we demonstrate the concept and method of C-path (converted-wave path) imaging. We analyze the survey efficiency of C-paths with at least one S-segment inside the salt body and summarize three facts about C-paths: 1) The C-path involving fewer mode conversions has higher efficiency. 2) The symmetric C-path mainly concentrates at the small offset and the asymmetric C-path has broad spread over the offset. 3) The C-paths complement the dip coverage of pure P-path which has a cut-off angle. The C-path is capable of imaging very steep subsalt reflectors, but often is less efficient. The efficiency analyses provide the strategy for C-path selection during migration. By selecting proper C-path or C-path combination, we can image the steep subsalt reflectors missing in the conventional P-wave image, and better control the migration artifacts. Even then C-path migration cannot exclude all the cross-talks. The preprocessing of the seismic data may help to remove all the artifacts.

6.6 REFRENCES

Aki, K., and P.G. Richards, 1980, Quantitative seismology: Theory and methods, W. H. Freeman and Co., 151-153.

Fuchs, K., and G. Müller, 1971, Computation of synthetic seismograms with the reflectivity method and comparison with observations: Geophys. J. R. astr. Soc., 23, 417-433.

Hanssen, P., X. Y. Li, and A. Ziolkowski, 2000, Converted waves for sub-basalt imaging? 70th Annual International Meeting, SEG, Expanded Abstracts, MC 2.3.

Jones, N. and J. Gaiser, 1999, Imaging beneath high-velocity layers: 68th Annual International Meeting, SEG, Expanded Abstacts, 713-716.

Kendall, R.R., S. H. Gray, and G. E. Murphy, 1998, Subsalt imaging using prestack depth migration of converted waves: Mahogany Field, Gulf of Mexico: 68th Annual International Meeting, SEG, Expanded Abstacts, 2052-2055.

Müller, G., 1985, The reflectivity method: a tutorial: J. geophys, 58, 153-174.

Purnell, G. W., 1992, Imaging beneath a high-velocity layer using converted wave, Geophysics, 57, 1444-1452.

Wu, R.S., and K. Aki, 1985, Scattering characteristics of waves by an elastic heterogeneity: Geophysics, 50, 582-595.

Wu, R. S., 1994, Wide-angle elastic wave one-way propagation in heterogeneous media and an elastic wave complex-screen method: Journal of Geophysical Research, 99, 751–766.

Wu, R. S., 1996, Synthetic seismograms in heterogeneous media by one-return approximation: Pure and Applied Geophysics, 148, 155–173.

Wu, R.S., X.B. Xie and X.Y. Wu, 2006, One-way and one-return approximations for fast elastic wave modeling in complex media, Chapter 5 of " Advances in Wave Propagation in Heterogeneous Earth", edited by R.S. Wu and V. Maupin, Elsevier, 266-323.

Xie, X. B., and R. S. Wu, 2001, Modeling elastic wave forward propagation and reflection using the complex screen method: Journal of the Acoustic Society of America, 109, 2629–2635.

6.7 FIGURES AND TABLES

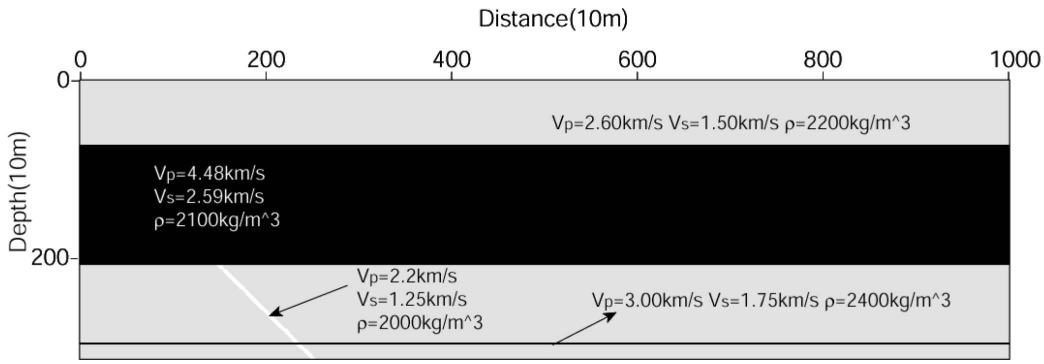

Figure 6.1 The elastic model used for converted path investigation. The P- and S-wave velocities and density are labeled in the figure. The horizontal salt layer is embedded between two sedimentary layers. A horizontal reflector and a 45^0-dipping reflector are located beneath the salt layer.

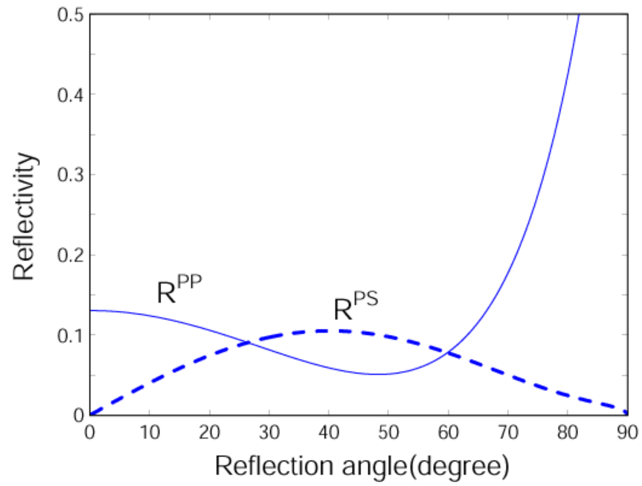

Figure 6.2 P-P (solid line) and P-S (dashed line) reflectivity on a reflector (fault). Note that at small reflection angles, the P-to-S reflectivity (conversion coefficient) is very weak in comparison with the P-P reflectivity.

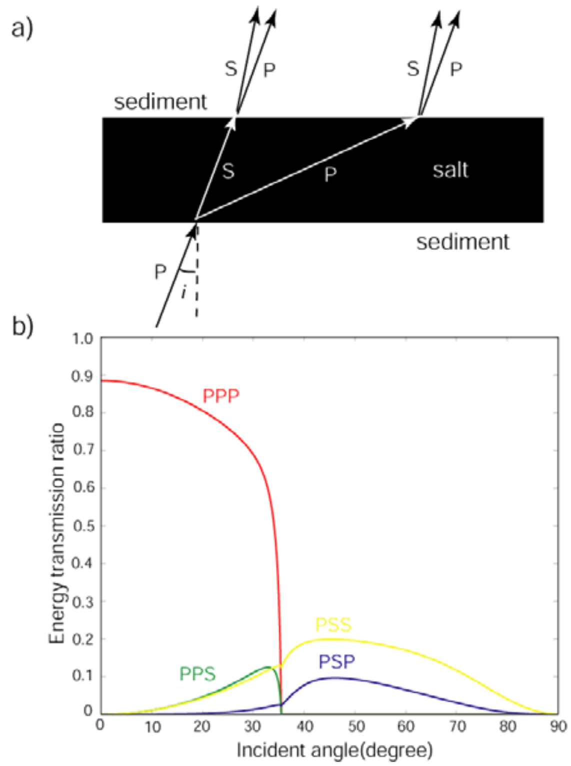

Figure 6.3 a) A schematic diagram of one-way transmitted wave paths penetrating through a salt layer, (b) wave energy versus the incident angle for different converted paths.

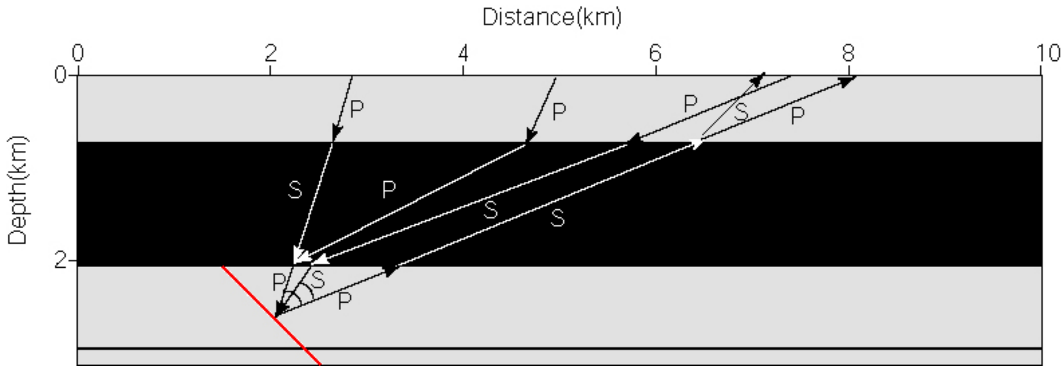

Figure 6.4 A schematic diagram of converted wave paths that provide illumination to a 45°-dip subsalt fault (C-path illumination analysis).

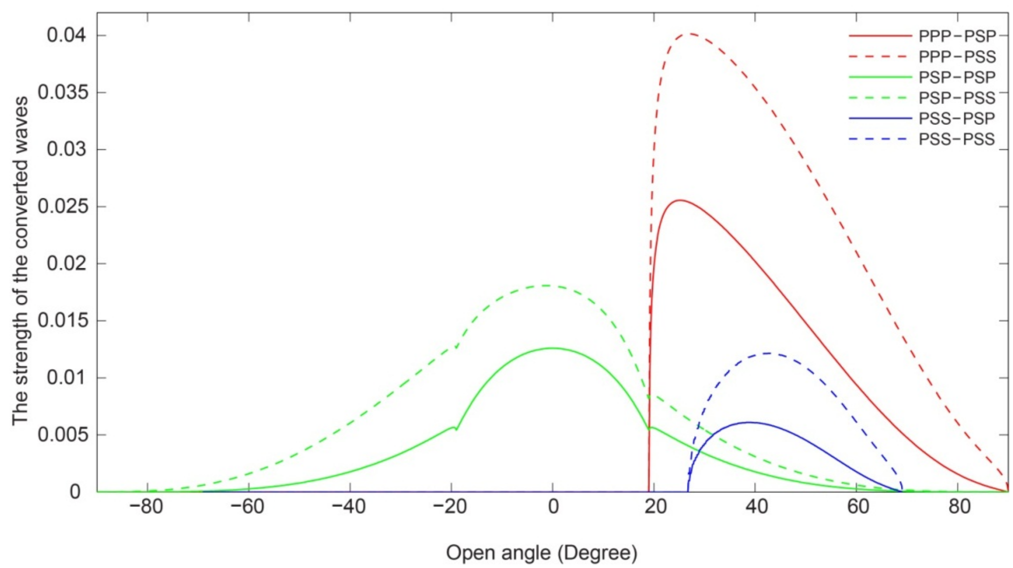

Figure 6.5 The strength of C-path as a function of open angle at the target for steep fault illumination as shown in Figure 6.4.

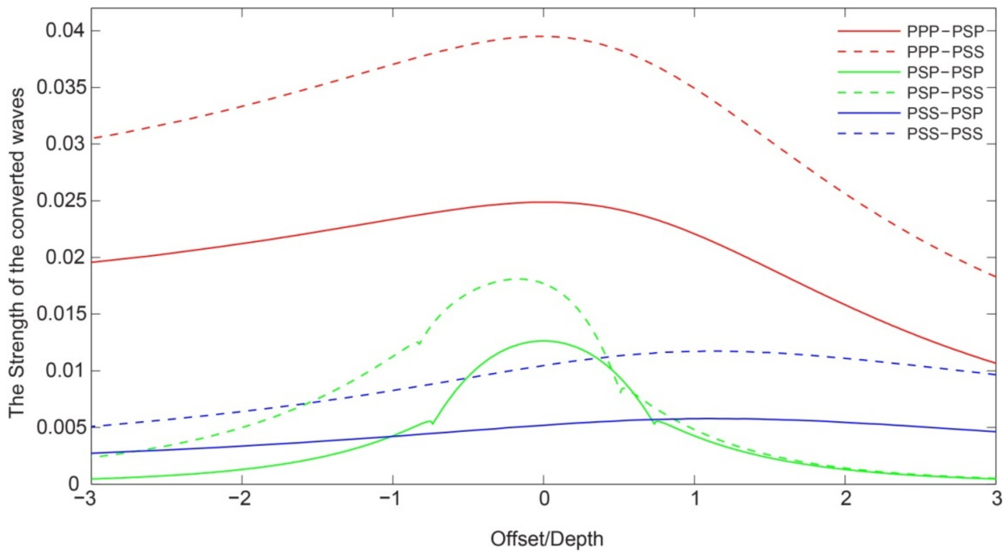

Figure 6.6 The strength of C-path as a function of normalized offset for steep fault illumination.

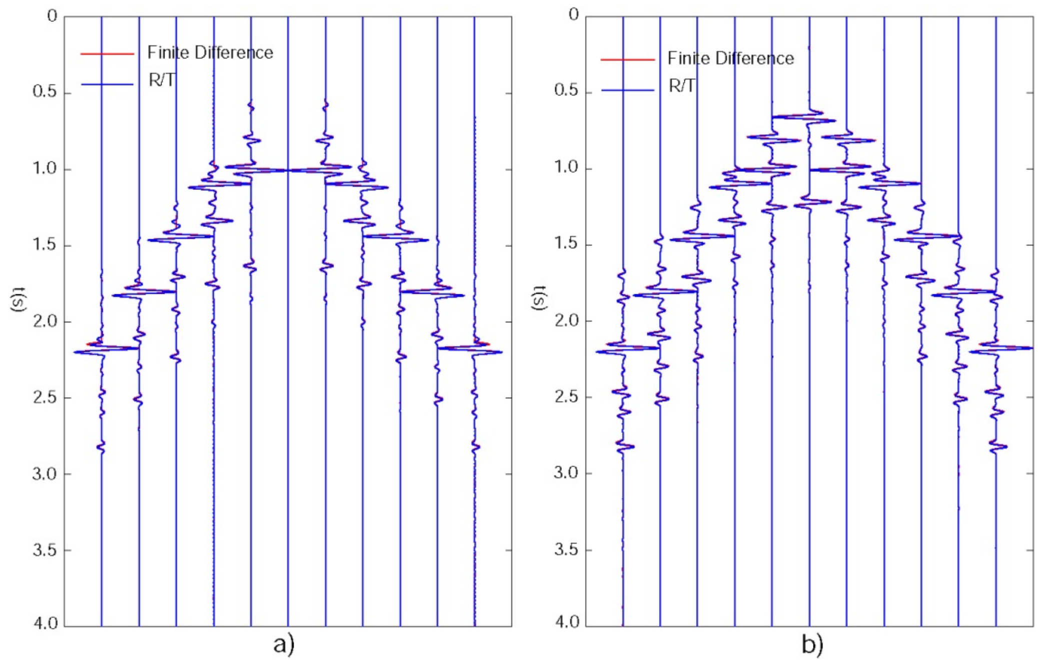

Figure 6.7 Comparison of the seismograms calculated by R/T method and the finite difference method for the background layered medium. a) horizontal displacement, b) vertical displacement.

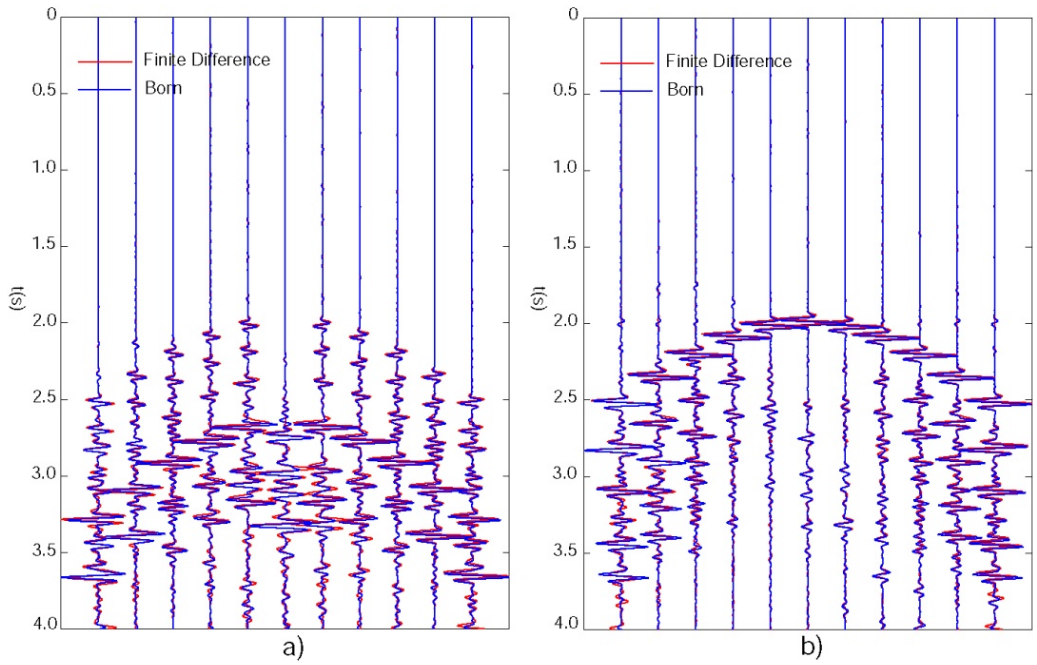

Figure 6.8 Comparison of the seismograms calculated by elastic Born approximation and finite difference method for the target reflectors. a) horizontal displacement, b) vertical displacement. The background reflections are eliminated by setting all the reflection coefficients at the salt/sediment interfaces to zero.

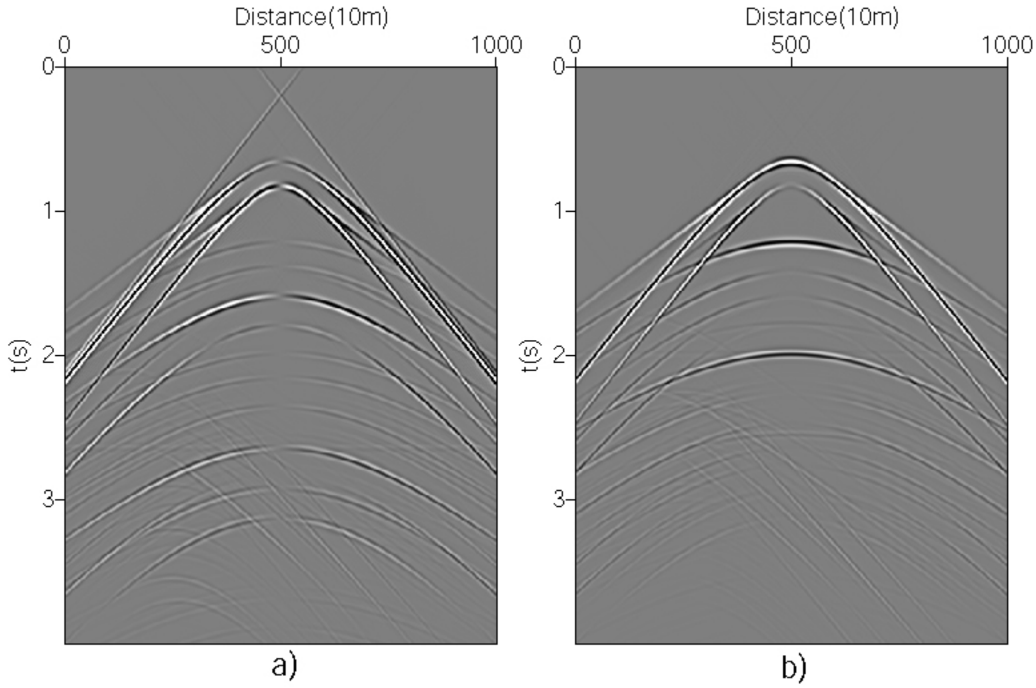

Figure 6.9 a) Horizontal-component and b) vertical-component seismograms calculated by the hybrid R/T-Born method. The reflections from the subsalt steep reflector through C-paths are evident.

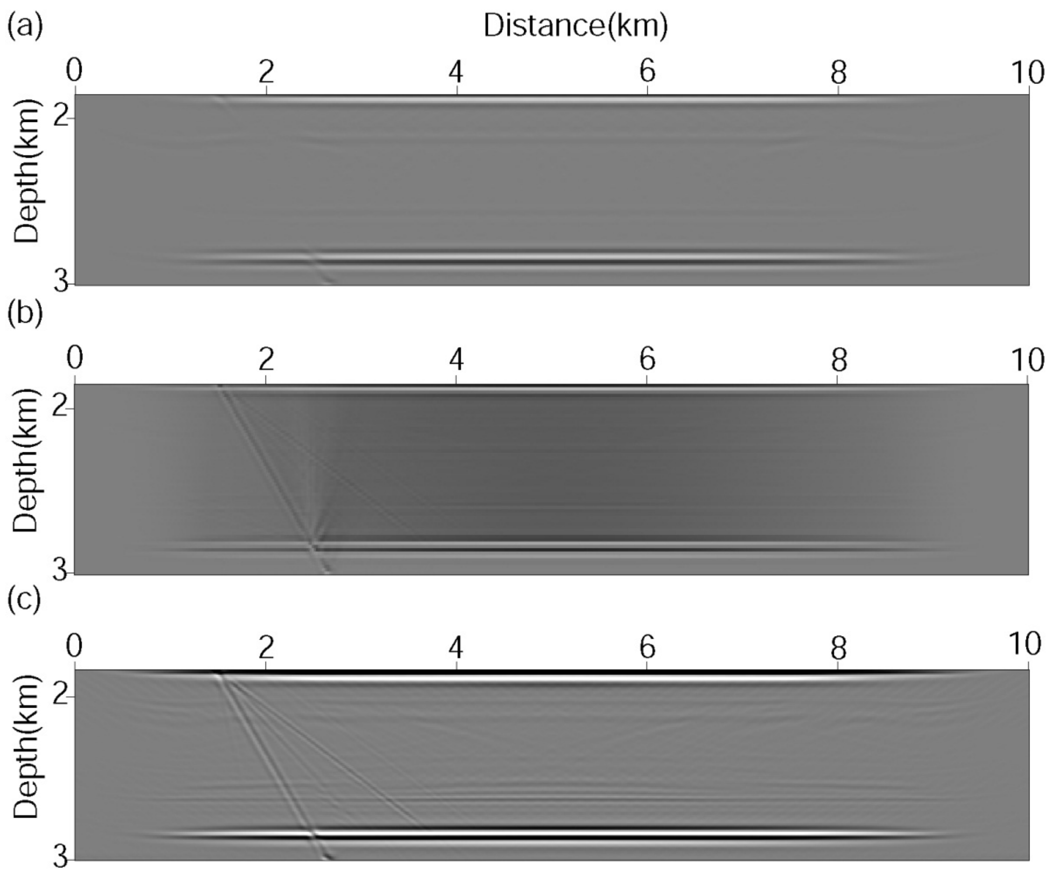

Figure 6.10 Comparison of (a) conventional acoustic migration, (b) conventional elastic RTM migration, and c) conventional elastic one-way migration.

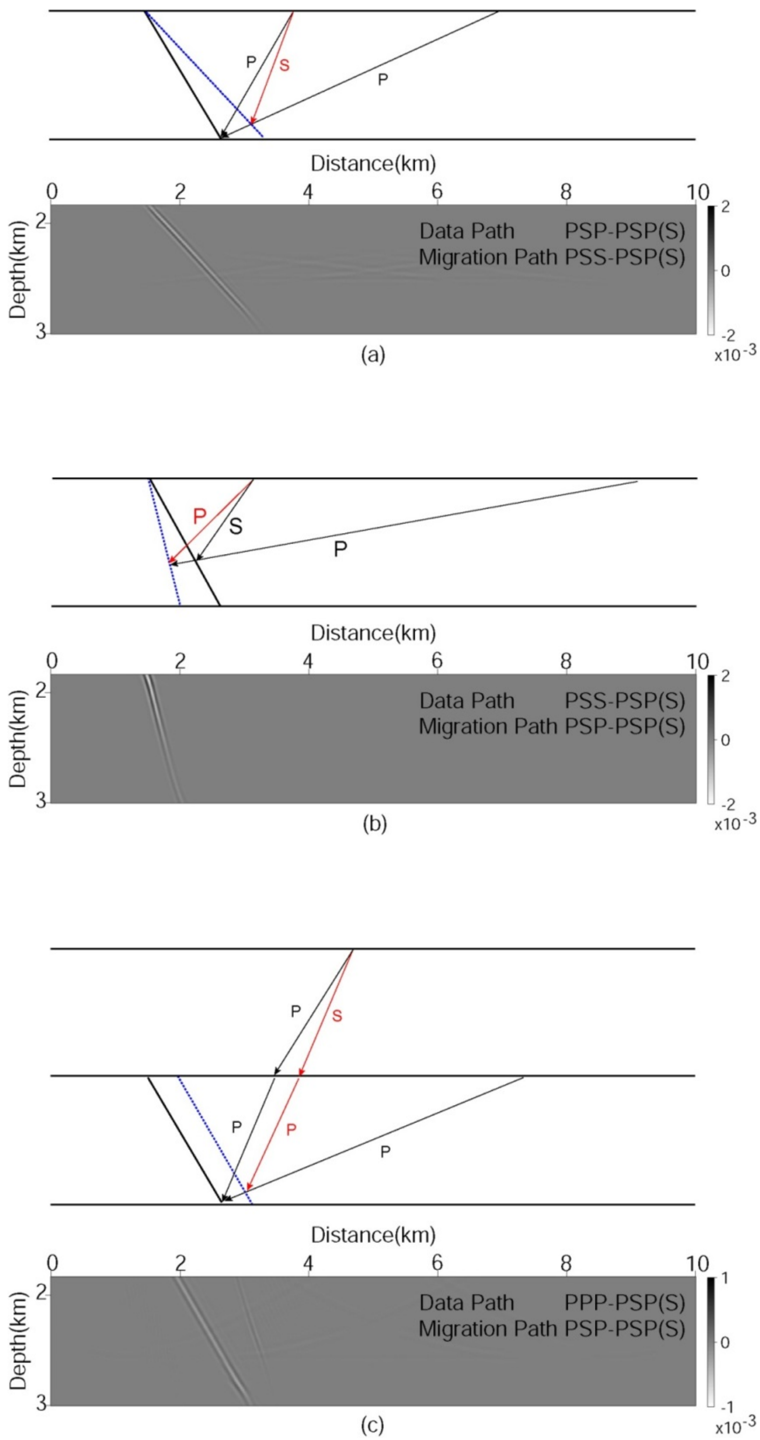

Figure 6.11 Examples of path mismatch between the data and the migration operator.

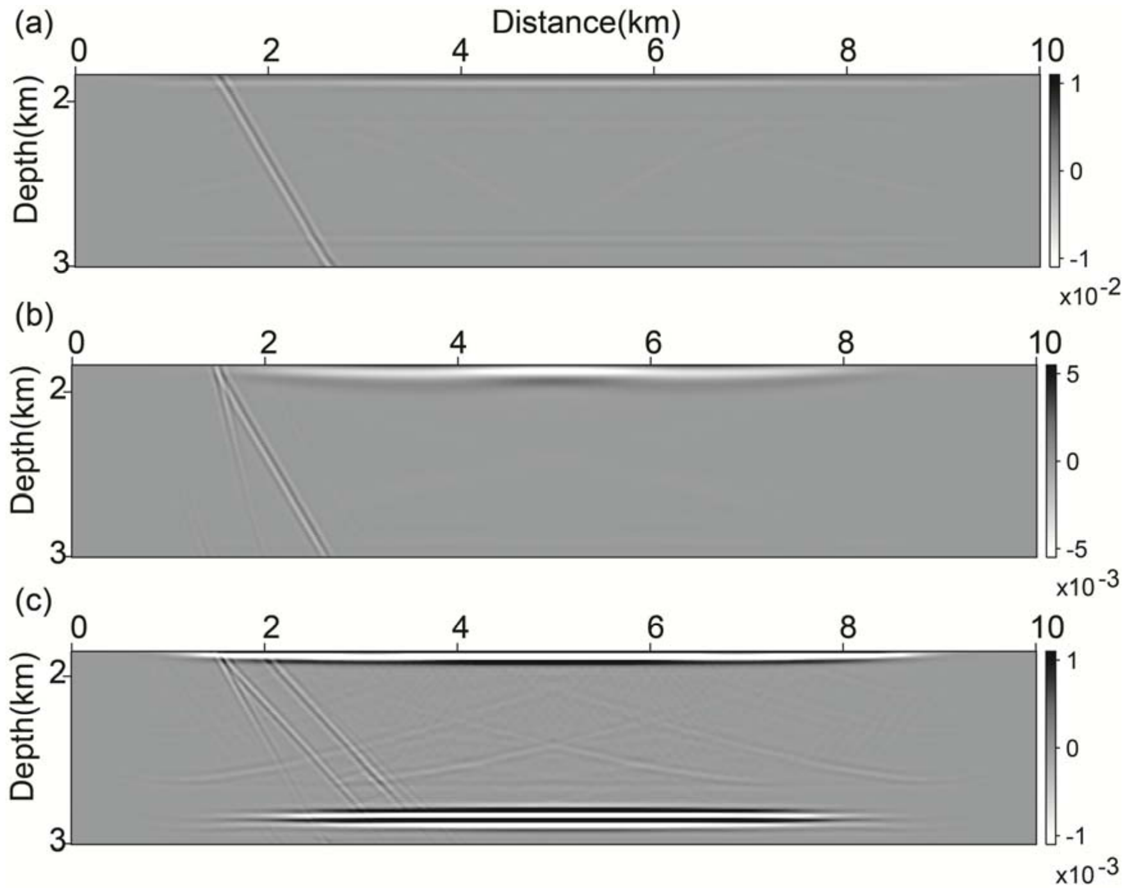

Figure 6.12 Comparison of (a) C-path image through PPP-PSP(S), (b) through PSP-PSP(S), and c) through PSS-PSP(S).

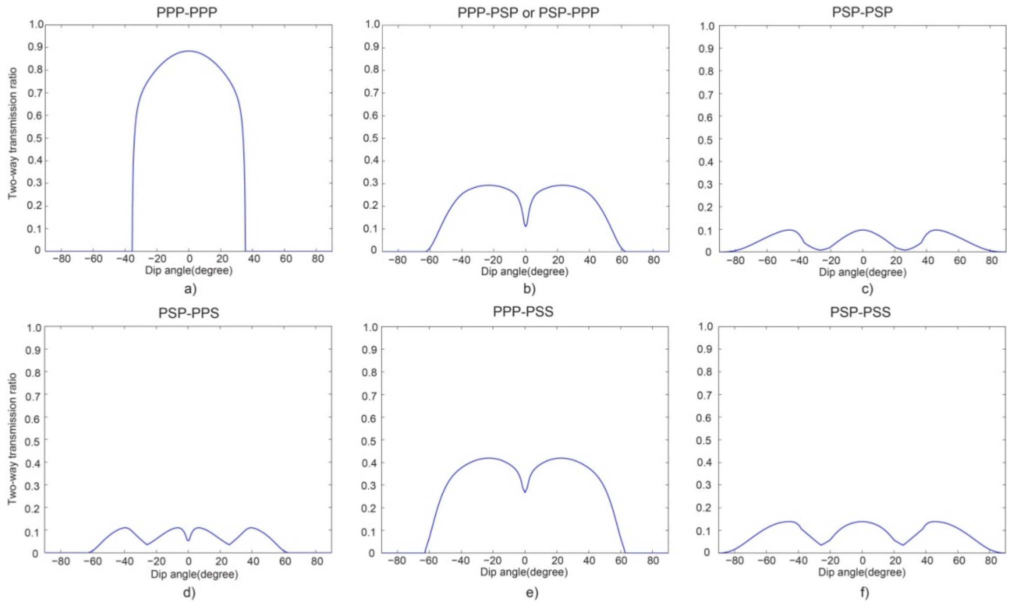

Figure 6.13 The dip responses of P-path and C-paths as a function of subsalt reflector-dip. The horizontal axis is the dip angle of the subsalt reflector.

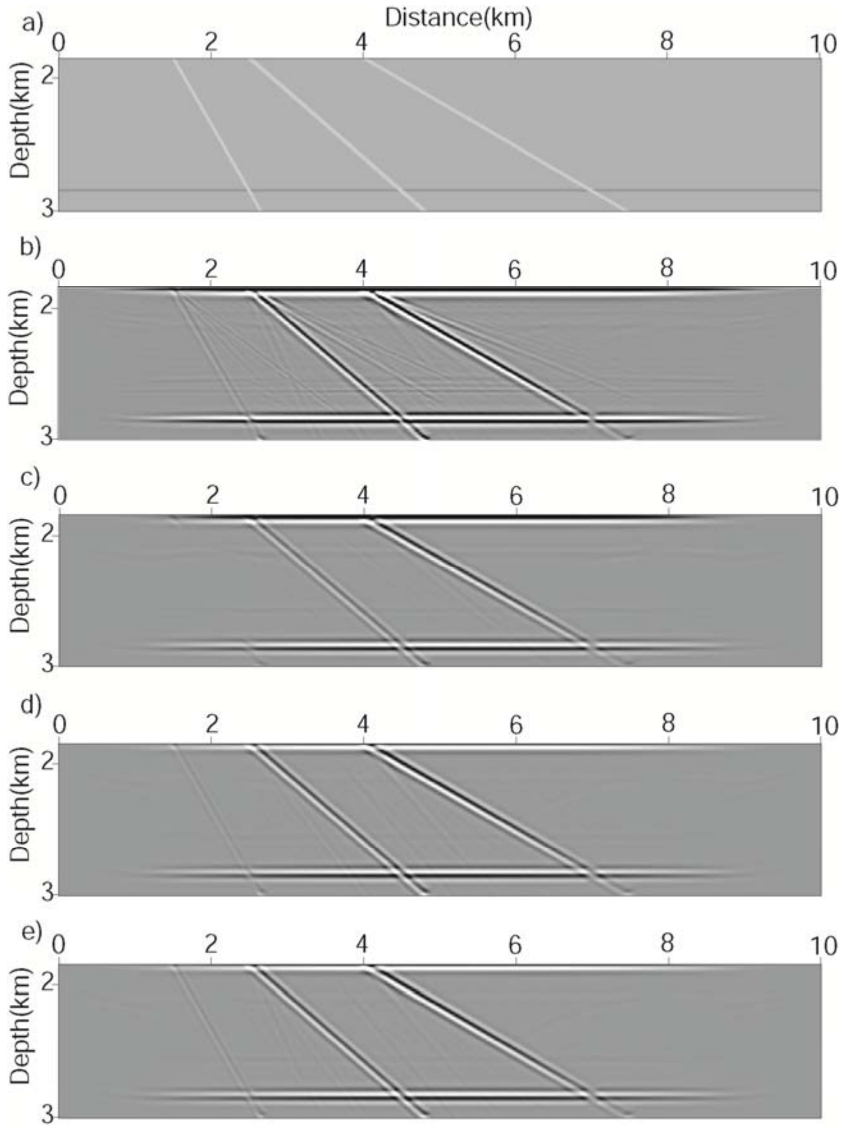

Figure 6.14 (a) The velocity model having three subsalt faults with different dip angles (45^0, 30^0 and 15^0). (b) Image by conventional elastic wave migration; (c) Image with path PPP-PPP/S switched on; (d) Image with path combination PPP-PPP/S, PPP-PSP/S and PSP-PPP/S switched on; (e) Image with path combination PPP-PPP/S, PPP-PSP/S, PSP-PPP/S and PSP-PSP/S switched on.

7 A HYBRID ELASTIC ONE-WAY PROPAGATOR FOR STRONG-CONTRAST MEDIA AND ITS APPLICATION TO SUBSALT IMAGING[4]

7.1 SUMMARY

To overcome the weak scattering limitation of traditional one-way elastic propagator, we propose a hybrid elastic propagator for strong-contrast media, which combines the thin-slab propagator with RT (reflection/transmission) operator at the sharp boundary. In the framework of the hybrid one-way propagator, the elastic model is separated into two or more domains along the strong contrast boundary and the wave propagation in each domain is realized in a depth-marching fashion. Within the thin-slab of each marching step, the perturbations are relatively weak so are treated as volume scatterings and are solved by local Born approximation. The communications between different domains occurs at the boundary elements within the thin slab and are formulated as boundary scatterings, which are calculated by applying the local reflection/transmission operator to the incident wave with the tangent plane approximation. The wavefields at the exit of the thin slab will be updated by the scattered waves from the volume heterogeneities plus the reflected/transmitted waves from the sharp boundary, and then serve as the incident waves at the entrance of the next thin slab. The hybrid propagator shuttles between wavenumber and space domain: wave propagation in wavenumber domain and heterogeneities interaction in

[4] This paper has been submitted to Geophysical Prospecting.

space domain, promising high efficiency and accuracy of the propagator. Numerical tests using two simple salt models demonstrate the validity of the hybrid propagator. Finally the new propagator is applied to subsalt migration using synthetic data generated based on the 2D Subsalt model.

7.2 INTRODUCTION

Subsalt exploration can be very challenging due to the issues posed by the often complex geometry of the salt bodies and the large impedance contrasts between salt and surrounding sediment deposits. The large velocity contrast across the sedimentary/salt interfaces together with the frequently rugose character of these interfaces prevents P-waves from penetrating through the salt body with sufficient strength. However, the mode conversion is quite efficient at the salt interfaces. Converted waves may carry considerable energy to illuminate the subsalt structure (Purnell, 1992; Wu et al., 2001, 2010). The elastic nature of seismic waves is amplified in such kind of strong contrast media, so that it is preferred to conduct elastic wave imaging in order to improve the migration image provide by P-wave survey alone.

Previous attempt of elastic wave imaging adopted scalar wave propagators for both P- and S-waves (e.g., Zhe and Greenhalgh, 1997; Sun and McMechan, 2001; Hou and Marfurt, 2002). However, the use of scalar wave propagator for elastic wave extrapolation is dynamically incorrect. Elastic RTM (e.g., Sun and McMechan, 1986; Chang and McMechan, 1987, 1994) extrapolates the wavefields based on the elastic wave equation, but P- and S- modes are mixed together and hard to separate. Elastic thin-slab and elastic complex screen method (Wu and Xie, 1994; Xie and Wu, 1995, 2001, 2005; Wu and Wu, 2005; for a review, see Wu et al., 2007) are developed for one-way migration. It has its special features and advantages in applying to seismic imaging. First of all, similar to elastic RTM, those one-way migrations use vector wavefield extrapolator so P-S and S-P conversions are well handled. Secondly, mode type is kept during migration, which is especially useful for elastic wave imaging in terms of controlling migration cross-talks and parameter inversion. Thirdly, one-way wave method is much more efficient, often being orders of magnitude faster than the full wave method.

The elastic thin-slab or elastic complex screen methods are based on perturbation theory. They can handle elastic perturbations only up to 30% (Wu and Wu, 2005). The algorithms may become instable beyond this limit. Although these methods can be useful in reservoir modeling and imaging, they are currently excluded from the applications for strong-contrast media, such as salt or basalt inclusions. In order to take its full advantages, it is pressing to extend the one-way elastic method to the case of strong-contrast media.

To handle the strong heterogeneous media with sharp boundary, we propose to solve the boundary problem by applying a local reflection/transmission operator and combine it with thin-slab propagator for weak perturbations in the framework of one-way marching algorithm. In this study, we first briefly summarize the theory of the elastic one-way propagator realized by sequential thin-slab for weak perturbations. Secondly, we present the formulations for the new theory on hybrid elastic one-way propagator in strong contrast medium with sharp boundary and describe its three essential components in detail. Finally, we conduct two numerical tests to verify the accuracy and efficiency of the hybrid elastic one-way propagator and also use the Subsalt model to demonstrate its application to seismic imaging.

7.3 ELASTIC THIN-SLAB PROPAGATOR FOR WAKLY HETEROGENOUS MEDIA

For an arbitrary heterogeneous medium, we slice the medium into numerous thin-slabs transverse to the propagation direction (preferred direction). Shown in Figure 7.1 is an example of an individual thin-slab for elastic media. Assume each thin-slab is thin enough so that the Born approximation can be used for the volume scattering calculation. In the perturbation theory- based method, the weak heterogeneities in a thin slab are treated as parameter perturbations from the background medium. (See Aki and Richards, 1980; Wu and Aki, 1985)

$$\begin{aligned} \rho(\mathbf{x}) &= \rho_0 + \delta\rho(\mathbf{x}) \\ c(\mathbf{x}) &= c_0 + \delta c(\mathbf{x}) \ , \\ \mathbf{u}(\mathbf{x}) &= \mathbf{u}_0 + \mathbf{u}_V(\mathbf{x}) \end{aligned} \tag{7.1}$$

where ρ_0 and $\mathbf{c}_0$ are the density and elastic constants of the background medium, $\delta\rho$ and $\delta\mathbf{c}$ are the corresponding perturbations, $\mathbf{u}_0$ is the incident displacement field, $\mathbf{u}_V$ is the scattered field by the volume heterogeneities and $\mathbf{u}$ is the total field. See Figure 7.1.

In the frequency domain, elastic wave equation can be written as

$$-\omega^2 \rho(\mathbf{x})\mathbf{u}(\mathbf{x}) = \nabla \cdot \left[\frac{1}{2}\mathbf{c} : \left(\nabla \mathbf{u} + \mathbf{u}\nabla \right) \right] , \tag{7.2}$$

where ∇ is the spatial gradient operator. From equation 7.2 and 7.3 we derive the wave equation for the scattered field

$$-\omega^2 \rho_0 \mathbf{u}_V - \nabla \cdot \left[\frac{1}{2}\mathbf{c}_0 : \left(\nabla \mathbf{u}_V + \mathbf{u}_V \nabla \right) \right] = \mathbf{Q}, \tag{7.3}$$

Where

$$\mathbf{Q} = \omega^2 \delta\rho \mathbf{u} + \nabla \cdot \left[\delta \mathbf{c} : \varepsilon \right], \tag{7.4}$$

is the equivalent body force due to volume scattering.

In a thin slab, local Born approximation is used to calculate the scattered wave

$$\mathbf{u}_V \left(\mathbf{x}, z_j \right) = \int_{z_{j-1}}^{z_j} dz \int d^2 \mathbf{x}_T \left\{ \mathbf{Q}_0 \left(\mathbf{x}_T, z \right) \cdot \mathbf{G}_0 \left(\mathbf{x}, z_j; \mathbf{x}_T, z \right) \right\}, \tag{7.5}$$

where $\mathbf{u}_V \left(\mathbf{x}, z_j \right)$ is the scattered field in the horizontal wavenumber domain, z_{j-1} is the entrance of the thin slab, z_j is the exit of the thin slab, $\mathbf{G}_0 \left(\mathbf{x}, z_j; \mathbf{x}_T, z \right)$ is the background elastic Green's function in the current thin slab, where

$$\mathbf{Q}_0 \left(\mathbf{x}_T, z \right) = \delta\rho\omega^2 \mathbf{u}_0 \left(\mathbf{x}_T, z \right) + \nabla \cdot \left[\delta \mathbf{c} : \varepsilon_0 \left(\mathbf{x}_T, z \right) \right], \tag{7.6}$$

is the equivalent body force under Born approximation, where $\mathbf{u}_0$ and ε_0 are the incident displacement and strain fields at the thin-slab, respectively.

Following the derivation of this equation, we express the scattered displacement fields for P and S modes within a thin-slab in the horizontal wavenumber domain (Wu, 1994, 1996; Wu et al., 2007):

$$\mathbf{u}_V^P\left(\mathbf{K}_T, z_j\right) = \int_{z_{j-1}}^{z_j} dz \int d^2\mathbf{x}_T \mathbf{Q}_0\left(\mathbf{x}_T, z\right) \cdot \mathbf{G}_0^P\left(\mathbf{K}_T, z_i; \mathbf{x}_T, z\right), \tag{7.7}$$

$$\mathbf{u}_V^S\left(\mathbf{K}_T, z_j\right) = \int_{z_{j-1}}^{z_j} dz \int d^2\mathbf{x}_T \mathbf{Q}_0\left(\mathbf{x}_T, z\right) \cdot \mathbf{G}_0^S\left(\mathbf{K}_T, z_i; \mathbf{x}_T, z\right), \tag{7.8}$$

where $\mathbf{G}_0^P\left(\mathbf{K}_T, z_j; \mathbf{x}_T, z\right)$ and $\mathbf{G}_0^S\left(\mathbf{K}_T, z_j; \mathbf{x}_T, z\right)$ are the background Green's function for P and S waves, respectively (see Appendix A).

For isotropic media,

$$\begin{aligned}\mathbf{Q}_0\left(\mathbf{x}_T, z\right) = {} & \delta\rho\left(\mathbf{x}_T, z\right)\omega^2\mathbf{u}_0\left(\mathbf{x}_T, z\right) \\ & +\nabla\cdot\left[\delta\lambda\left(\mathbf{x}_T, z\right)\left|\varepsilon_0\left(\mathbf{x}_T, z\right)\right|\mathbf{I} + 2\delta\mu\left(\mathbf{x}_T, z\right)\varepsilon_0\left(\mathbf{x}_T, z\right)\right]\end{aligned}, \tag{7.9}$$

where λ and μ are the Lame constants, $\mathbf{I}$ is the unit tensor. In this equation, the space-domain incident field, its divergence and strain field (composed of its gradients) at level z are calculated in the spectral domain as

$$\begin{aligned}\mathbf{u}_0\left(\mathbf{x}_T, z\right) = {} & \int \mathbf{u}_0^P\left(\mathbf{K}'_T, z_{j-1}\right) e^{i\gamma'_\alpha\left(z - z_{j-1}\right)} d^2\mathbf{K}'_T \\ & + \int \mathbf{u}_0^S\left(\mathbf{K}'_T, z_{j-1}\right) e^{i\gamma'_\beta\left(z - z_{j-1}\right)} d^2\mathbf{K}'_T \\ \nabla\cdot\left\{\left|\varepsilon_0\left(\mathbf{x}_T, z\right)\right|\mathbf{I}\right\} = {} & -\int\left[\mathbf{k}'_\alpha\cdot\mathbf{u}_0^P\left(\mathbf{K}'_T, z_{j-1}\right)\right]\mathbf{k}'_\alpha e^{i\gamma'_\alpha\left(z - z_{j-1}\right)} d^2\mathbf{K}'_T \\ \nabla\cdot\varepsilon_0\left(\mathbf{x}_T, z\right) = {} & -\int\left[\mathbf{k}'_\alpha\mathbf{u}_0^P\left(\mathbf{K}'_T, z_{j-1}\right) + \mathbf{u}_0^P\left(\mathbf{K}'_T, z_{j-1}\right)\mathbf{k}'_\alpha\right]\cdot\mathbf{k}'_\alpha e^{i\gamma'_\alpha\left(z - z_{j-1}\right)} d^2\mathbf{K}'_T \\ & -\int\left[\mathbf{k}'_\beta\mathbf{u}_0^S\left(\mathbf{K}'_T, z_{j-1}\right) + \mathbf{u}_0^S\left(\mathbf{K}'_T, z_{j-1}\right)\mathbf{k}'_\beta\right]\cdot\mathbf{k}'_\beta e^{i\gamma'_\beta\left(z - z_{j-1}\right)} d^2\mathbf{K}'_T\end{aligned}, \tag{7.10}$$

with $\mathbf{k}_\alpha = (\mathbf{K}_T, \gamma_\alpha)$ and $\mathbf{k}_\beta = (\mathbf{K}_T, \gamma_\beta)$ representing the P and S wavenumber vectors respectively, with $\mathbf{K}_T$ as the horizontal wavenumber while γ_α and γ_β are the vertical wavenumbers for P and S waves, respectively.

The incident waves are propagated with the background reference velocities in the current slab

$$\mathbf{u}_0^P\left(\mathbf{K}_T, z_j\right) = \mathbf{u}_0^P\left(\mathbf{K}_T, z_{j-1}\right) e^{i\gamma_\alpha\left(z_j - z_{j-1}\right)}, \tag{7.11}$$

$$\mathbf{u}_0^S\left(\mathbf{K}_T, z_j\right) = \mathbf{u}_0^S\left(\mathbf{K}_T, z_{j-1}\right) e^{i\gamma_\beta\left(z_j - z_{j-1}\right)}. \tag{7.12}$$

At the exit (bottom) of each thin-slab, the scattered field is added to the incident field to obtain the total wave-field which in turn is treated as the updated incident wave-field for the next thin-slab.

$$\mathbf{u}^P\left(\mathbf{x}_T, z_j\right) = \frac{1}{4\pi^2} \int d^2\mathbf{K}_T e^{i\mathbf{K}_T\mathbf{x}_T} \left[\mathbf{u}_0^P\left(\mathbf{K}_T, z_j\right) + \mathbf{u}_V^P\left(\mathbf{K}_T, z_j\right)\right], \tag{7.13}$$

$$\mathbf{u}^S\left(\mathbf{x}_T, z_j\right) = \frac{1}{4\pi^2} \int d^2\mathbf{K}_T e^{i\mathbf{K}_T\mathbf{x}_T} \left[\mathbf{u}_0^S\left(\mathbf{K}_T, z_j\right) + \mathbf{u}_V^S\left(\mathbf{K}_T, z_j\right)\right], \tag{7.14}$$

The incident field updating is realized by a marching algorithm along the forward propagation direction (z-direction) step-by-step (see Figure 7.1). The marching algorithm is implemented by an operator split method in the dual domain: background propagation in the wavenumber domain and interaction with perturbations in the space domain.

7.4 HYBRID ELASTIC ONE-WAY PROPAGATOR IN STRONGLY HETEROGENEOUS MEDIA WITH SHARP BOUNDARY

For weak heterogeneities, the perturbation method is a valid and convenient tool for elastic wave scattering and propagation. For strongly heterogeneous media with sharp boundaries, such as salt or basalt inclusions, the perturbation approach fails in most cases. To handle this specific case, we divide the model into different domains along the sharp boundary (Figure 7.2). In each domain, the wave field can be computed with the representation integral:

$$\mathbf{u}(\mathbf{x}) = \int \mathbf{Q}(\mathbf{x}') \cdot \mathbf{G}(\mathbf{x};\mathbf{x}') d\Omega(\mathbf{x}') + \int \left\{ [\hat{n} \cdot \boldsymbol{\sigma}(\mathbf{x}')] \cdot \mathbf{G}(\mathbf{x};\mathbf{x}') - \mathbf{u}(\mathbf{x}') \cdot [\hat{n} \cdot \boldsymbol{\Sigma}(\mathbf{x};\mathbf{x}')] \right\} dS(\mathbf{x}') \quad ,(7.15)$$
$$\mathbf{x},\ \mathbf{x}' \in \Omega; \qquad S = \partial\Omega$$

where $\mathbf{u}(\mathbf{x})$ is the displacement field at point $\mathbf{x}$ within the volume Ω enclosed by surface S, $G(\mathbf{x};\mathbf{x}')$ is Green's displacement tensor (dyadic) and $\Sigma(\mathbf{x};\mathbf{x}')$ is Green's stress tensor (triadic). $\hat{n}$ is the surface normal as towards to the exterior of Ω. $\mathbf{u}(\mathbf{x}')$ and $\sigma(\mathbf{x}')$ are the displacement and stress on the surface; $\mathbf{Q}(\mathbf{x}')$ is body forces or equivalent body forces due to scattering. The volume integral term yields the contribution due to the sources inside Ω, while the surface integral term, that is, Kirchhoff integral, accounts for the energy communication between different domains. The traditional way to calculate the scattered wave in each domain is to solve the integral equation along the boundary. However, it involves huge computations because the interactions between all the boundary elements are considered. Following the spirit of the thin-slab propagator, we solve the problem iteratively in a one-way fashion. The resultant operator is called the hybrid elastic one-way propagator.

Figure 7.2 schematically shows the realization of a typical hybrid propagator in a strong heterogeneous medium with a sharp boundary. As the velocity model is sliced into a thin slab, the sharp boundary is discretized into many boundary elements. The thin slab is separated into two domains: a high velocity one and a low velocity one with two boundary elements. Within each domain, the parameter variations (perturbations) are relatively weak. They are treated as volume scatterings and handled by thin-slab propagator. Besides the volume scatterings, each domain will admit internal reflections and transmissions from adjacent domains at the boundary elements. They together are called boundary scatterings. We assume that the boundary elements within one thin slab are decoupled from each other so that the reverberations between them are neglected. The displacement and traction fields of the boundary scatterings can be approximately calculated by applying a reflection/transmission operator to the wave incident on the boundary element. It corresponds to a tangent plane approximation for smoothly curved boundary (Voronorich, 1989). When an incident wave enters a thin slab, it will interact with the volume heterogeneities as well as the boundary element in the current slab. The representation integral will give the scattered wave which will be added to the incident wave at the exit of the thin slab. Based on the one-way propagation principle, the wavefields are updated iteratively step-by-step in the forward direction with no consideration of the backward scatterings.

In this subsection, we will describe three critical components of migration algorithms: thin-slab propagator for weak volume scatterings, background propagation, and reflection/transmission operator for sharp boundary scatterings.

7.4.1 Thin-slab propagator for weak volume scatterings

When several domains exist in a velocity model, the wave propagation in each domain will be handled separately with traditional thin-slab propagator. Different domains have different background velocities, so that the weak perturbations assumptions of thin-slab propagator can be guaranteed in each domain. The interaction with the weak heterogeneities will be calculated with the Green' tensor $\mathbf{G}_0^{P(i)}$ and $\mathbf{G}_0^{S(i)}$ for the domain i using the corresponding background velocities:

$$\mathbf{u}_V^{P(i)}\left(\mathbf{K}_T, z_j\right)=\int_{z_{j-1}}^{z_j} dz \int d^2\mathbf{x}_T \mathbf{Q}_0\left(\mathbf{x}_T, z\right)\cdot\mathbf{G}_0^{P(i)}\left(\mathbf{K}_T, z_i; \mathbf{x}_T, z\right), \qquad \left(\mathbf{x}_T, z\right)\in\Omega_i, \quad (7.16)$$

$$\mathbf{u}_V^{S(i)}\left(\mathbf{K}_T, z_j\right)=\int_{z_{j-1}}^{z_j} dz \int d^2\mathbf{x}_T \mathbf{Q}_0\left(\mathbf{x}_T, z\right)\cdot\mathbf{G}_0^{S(i)}\left(\mathbf{K}_T, z_i; \mathbf{x}_T, z\right), \qquad \left(\mathbf{x}_T, z\right)\in\Omega_i, \quad (7.17)$$

where Ω_i is domain i, $\mathbf{Q}_0\left(\mathbf{x}_T, z\right)$ is the equivalent body force which is defined in equation 7.9.

7.4.2 Background propagation

The free propagation (background propagation) in the hybrid propagator is slightly different from the traditional propagator as below:

$$\mathbf{u}_0^{P(i)}(\mathbf{K}_T, z)=e^{i\gamma_\alpha\left(z-z_{j-1}\right)}\int d^2\mathbf{x}_T e^{-i\mathbf{K}_T\mathbf{x}_T}\mathbf{u}_0^{P(i)}(\mathbf{x}_T, z_{j-1}), \qquad \left(\mathbf{x}_T, z_{j-1}\right)\in\Omega_i, \quad (7.18)$$

$$\mathbf{u}_0^{S(i)}(\mathbf{K}_T, z) = e^{i\gamma_\beta(z - z_{j-1})}\int d^2\mathbf{x}_T e^{-i\mathbf{K}_T\mathbf{x}_T}\mathbf{u}_0^{S(i)}(\mathbf{x}_T, z_{j-1}), \qquad (\mathbf{x}_T, z_{j-1}) \in \Omega_i, \tag{7.19}$$

where Ω_i is domain i.

7.4.3 Transmission/reflection operators on the boundary elements

Boundary scatterings are formulated differently from volume scatterings in the thin slab. To compute the boundary scattering, we make a tangent plane approximation (Voronovich, 1999) which assumes the boundary surface is smoothly curved so that the reflection/transmission coefficients defined for an infinite plane surface can be applied locally at each surface element. In this sense the theory is a high-frequency asymptotic solution. It is nearly accurate for smoothly varying interface but has limited use for rough surface.

We focus our attention to one boundary element which separates the medium into upper and lower spaces. Regardless of their real domain numbers, we set the index for the upper medium as 1 and the lower medium as 2. The outer normal of the upper and lower medium are

$$\hat{n}_1 = -\hat{n}, \tag{7.20}$$

and

$$\hat{n}_2 = \hat{n}, \tag{7.21}$$

where $\hat{n}$ is the normal vector of the boundary element (see Figure 7.3).

The incident waves of the upper and lower medium are given from the output of previous thin slab as $\mathbf{U}_{0,1}$ and $\mathbf{U}_{0,2}$ in wavenumber domain. For simplicity, the wave type is ignored if the same operation is applied to both P- and S-waves. These incident waves include the scatterings of the previous boundary elements and the contributions from underneath are ignored. To accurately calculate the energy partition at the boundary element, we transform both the wavenumber vector and the displacement of the incident waves at the upper and lower mediums from the Cartesian coordinate to the local boundary coordinate (with horizontal axis parallel to the tangent of the local boundary).

$$\tilde{\mathbf{U}}_{0,I} = M^f \mathbf{U}_{0,I}, \qquad I = 1,2 \tag{7.22}$$

$$\tilde{\mathbf{k}} = M^f \mathbf{k}, \tag{7.23}$$

where

$$M^f = \begin{bmatrix} \cos\theta & \sin\theta \\ -\sin\theta & \cos\theta \end{bmatrix}, \tag{7.24}$$

is the transform matrix from the Cartesian coordinate to local boundary coordinate in 2D case. θ is the transform angle from the original coordinate to the local boundary coordinate. See Figure 7.3. Note that θ varies with location. $\mathbf{U}_{0,I}$ and $\tilde{\mathbf{U}}_{0,I}$ are the incident waves in the Cartesian coordinate and in the local boundary coordinate, respectively. $\mathbf{k}$ and $\tilde{\mathbf{k}}$ are the wavenumber vectors in the Cartesian coordinate and in the local boundary coordinate, respectively.

In the local boundary coordinate, reflection/transmission coefficients are applied to the incident wave:

$$\begin{bmatrix} \tilde{\mathbf{U}}_1^P \\ \tilde{\mathbf{U}}_1^S \\ \tilde{\mathbf{U}}_2^P \\ \tilde{\mathbf{U}}_2^S \end{bmatrix} = \begin{bmatrix} R_{11}^{PP} & R_{11}^{SP} & T_{21}^{PP} & T_{21}^{SP} \\ R_{11}^{PS} & R_{11}^{SS} & T_{21}^{PS} & T_{21}^{SS} \\ T_{12}^{PP} & T_{12}^{SP} & R_{22}^{PP} & R_{22}^{SP} \\ T_{12}^{PS} & T_{12}^{SS} & R_{22}^{PS} & R_{22}^{SS} \end{bmatrix} \begin{bmatrix} \tilde{\mathbf{U}}_{0,1}^P \\ \tilde{\mathbf{U}}_{0,1}^S \\ \tilde{\mathbf{U}}_{0,2}^P \\ \tilde{\mathbf{U}}_{0,2}^S \end{bmatrix}, \tag{7.25}$$

where R and T are reflection and transmission coefficients calculated by Zoeppritz's equation (Aki and Richards, 1980). The coefficients are dependent on the horizontal slowness in the local boundary coordinate. The first and second subscripts of the coefficients are the medium indexes. The superscripts of the coefficients specify the wave types in the upper and lower medium, respectively. $\tilde{\mathbf{U}}_I, I = 1,2$ is the displacement of the boundary scattering which is the sum of the internal reflected wave and the transmitted wave from the other domain. For the sake of simplicity, the wave type is ignored in the next few equations.

The traction of the boundary scattering can be calculated from the displacement by the constitutive equation in wavenumber domain. So in isotropic media, the traction corresponding to the displacement $\tilde{\mathbf{U}}_I$ is

$$\tilde{\mathbf{T}}_I\left(\tilde{\hat{n}}_I\right) = i\left[\lambda_I \tilde{\hat{n}}_I\left(\tilde{\mathbf{k}} \cdot \tilde{\mathbf{U}}_I\right) + \mu_I \tilde{\hat{n}}_I \cdot \left(\tilde{\mathbf{k}}\tilde{\mathbf{U}}_I + \tilde{\mathbf{U}}_I\tilde{\mathbf{k}}\right)\right], \qquad I = 1,2 \tag{7.26}$$

where λ_I and μ_I are the Lame constants; $\tilde{\hat{n}}_I$ is the unit normal vector of the boundary in the local boundary coordinate, and it is equivalent to the unit vector of positive or negative z'-direction in the local coordinate

$$\tilde{\hat{n}}_1 = \hat{z}', \tag{7.27}$$

$$\tilde{\hat{n}}_2 = -\hat{z}'. \tag{7.28}$$

Wavenumber-domain displacement $\tilde{\mathbf{U}}_I$ and traction $\tilde{\mathbf{T}}_I$ are still global. They become localized in space when we transform them into space domain and pick the values right at the boundary location. In this way, we get displacement and traction at the boundary element, but defined in the local boundary coordinate. In the space domain, we transform them back to the Cartesian coordinate:

$$\mathbf{U}_I = M^b \tilde{\mathbf{U}}_I, \quad I = 1,2, \tag{7.29}$$

$$\mathbf{T}_I = M^b \tilde{\mathbf{T}}_I, \quad I = 1,2, \tag{7.30}$$

where

$$M^b = \begin{bmatrix} \cos\theta & -\sin\theta \\ \sin\theta & \cos\theta \end{bmatrix}, \tag{7.31}$$

is the transform matrix from the local boundary coordinate to the Cartesian coordinate. $\mathbf{U}_I$ and $\tilde{\mathbf{U}}_I$ are the space-domain displacements of boundary scattering in the Cartesian and local boundary coordinate, respectively. $\mathbf{T}_I$ and $\tilde{\mathbf{T}}_I$ are the space-domain tractions of the boundary scattering in the Cartesian and local boundary coordinate, respectively.

For a given boundary element in a thin slab, we have determined the total displacement and traction on the element by the reflection/transmission operator. The scattered waves due to the boundary element at the slab exit can be calculated by Kirchhoff integral in the horizontal wavenumber domain (Wu, 1989)

$$\mathbf{U}^{P}_{B,I}(\mathbf{K}_T,z_j)=\int_L[\mathbf{T}^{P}_{I}(\mathbf{x}_T,z,\hat{n}_I)\cdot\mathbf{G}^{P}_{I}(\mathbf{K}_T,z_j;\mathbf{x}_T,z)-\mathbf{U}^{P}_{I}(\mathbf{x}_T,z)\cdot\mathbf{\Gamma}^{P}_{I}(\mathbf{K}_T,z_j;\mathbf{x}_T,z,\hat{n}_I)]dS \tag{7.32}$$

$$\mathbf{U}^{S}_{B,I}(\mathbf{K}_T,z_j)=\int_L[\mathbf{T}^{S}_{I}(\mathbf{x}_T,z,\hat{n}_I)\cdot\mathbf{G}^{S}_{I}(\mathbf{K}_T,z_j;\mathbf{x}_T,z)-\mathbf{U}^{S}_{I}(\mathbf{x}_T,z)\cdot\mathbf{\Gamma}^{S}_{I}(\mathbf{K}_T,z_j;\mathbf{x}_T,z,\hat{n}_I)]dS \tag{7.33}$$

where L is the boundary segment which separates the upper and lower mediums. $\mathbf{G}_I$ and $\mathbf{\Gamma}_I$ are the background Green's tensor of displacement and traction (see Appendix). The scattered wave will be added to the domains on both sides of the boundary element as $\mathbf{u}_B^{(i)}\left(\mathbf{K}_T,z_j\right)$, where i is the domain number.

At the exit of each thin-slab, the total field is composed of three parts: the incident (free-propagated) wave $\mathbf{u}_0^{(i)}$, the scattered field by volume heterogeneities $\mathbf{u}_V^{(i)}$ and the boundary scattered field $\mathbf{u}_B^{(i)}$

$$\begin{aligned}\mathbf{u}^{P(i)}\left(\mathbf{x}_T,z_j\right)=\frac{1}{4\pi^2}\int d^2\mathbf{K}_T e^{i\mathbf{K}_T\mathbf{x}_T}\\ \left[\mathbf{u}_0^{P(i)}\left(\mathbf{K}_T,z_j\right)+\mathbf{u}_V^{P(i)}\left(\mathbf{K}_T,z_j\right)+\mathbf{u}_B^{P(i)}\left(\mathbf{K}_T,z_j\right)\right],\left(\mathbf{x}_T,z_j\right)\in\Omega_i\end{aligned} \tag{7.34}$$

$$\begin{aligned}\mathbf{u}^{S(i)}\left(\mathbf{x}_T,z_j\right)=\frac{1}{4\pi^2}\int d^2\mathbf{K}_T e^{i\mathbf{K}_T\mathbf{x}_T}\\ \left[\mathbf{u}_0^{S(i)}\left(\mathbf{K}_T,z_j\right)+\mathbf{u}_V^{S(i)}\left(\mathbf{K}_T,z_j\right)+\mathbf{u}_B^{S(i)}\left(\mathbf{K}_T,z_j\right)\right],\left(\mathbf{x}_T,z_j\right)\in\Omega_i\end{aligned} \tag{7.35}$$

where Ω_i is domain i.

7.5 NUMERICAL TESTS FOR THE HYBRID ELASTIC ONE-WAY PROPAGATOR

First we test the elastic one-way propagator using a salt model with a wedge shape embedded in a homogeneous media. Figure 7.4 illustrates the velocity model with elastic parameters. The source is a 15 Hz Ricker wavelet located at the center of the model. In this simple case, the tangent plane approximation is expected to work the best. Illustrated in the upper panel of Figure 7.5 are the horizontal and vertical displacements calculated by the elastic one-way propagator. Compared with the snapshots calculated from full-wave finite difference (FD) (the lower panel of Figure 7.5), the transmitted wavefront of the elastic one-way propagator matches with them very well. The energy partition at the interface is almost the same as full-wave FD. In addition, to demonstrate the flexibility of the propagator, we show different wave paths (including PPP, PPS, PSP and PSS) by switching on/off wave mode at the interface in Figure 7.6. In terms of efficiency, the full-wave FD takes 1 hour with grid interval of 5 m while the hybrid one-way propagator takes 5 minutes with grid interval of 10 m.

We continue to compute the wave propagation for an elliptical salt model shown in Figure 7.7. The model is comprised of a sedimentary background and a salt inclusion with an elliptical shape. The elastic parameters are also provided in Figure 7.7. An explosive source is initiated on the center of the model surface. The source is a 15 Hz Ricker wavelet. Shown in Figure 7.8 are the comparison of the snapshots generated by the hybrid one-way propagator and full-wave FD. Notice that the major phases are very clear, even though some diffraction noises appear at very large angles. Different wave paths are depicted in Figure 7.9 by switching on/off wave mode at the boundary of the salt.

Finally, we move on to a more complex model – a 2D velocity profile simulating the Subsalt model (Figure 7.10). The outline of the sharp boundary is shown in Figure 7.11a and its dip angle is shown in Figure 7.11b. On top of the model is a water layer. The hybrid propagator can properly handle the fluid/solid interface. The model is divided into three different domains (Figure 7.11c) based on the salt/sedimentary boundary. Each domain has its own background and perturbation parameters. We design an observation system and conduct a seismic experiment. The acquisition system was comprised of 301 shots from 7000 m to 37000 m with an interval of 100 m. Each shot was recorded by a line of receivers with double-spread configuration. The number of receivers was 561 and the maximal offset is 7000 m. Both sources and receivers are located on the water surface. The recorded data are pressure-only simulating a hydrophone response. The source is a 15 Hz Ricker wavelet and the total recording time is 12 s with a time interval of 0.01 s. The synthetic data were modeled using the Tesseral 2D application package with a FD approach. Shown in Figure 7.12 are sample records for shot numbers 100, 150, 200 and 250. In each shot, the area for computation is 25.6 km × 13.5 km. Shown in Figure 7.13 are snapshots for shot 71. The converted waves penetrating through the salt base still carry considerable energy, which offers great potential to improve the subsalt imaging. We migrate the seismic data with the hybrid one-way propagator and obtain the PP, PS, SP and SS images. Here we only show the PP image in Figure 7.14 because it has the highest signal-to-noise ratio. From the migration image, a large portion of subsalt reflectors can be clearly identified, except the section with very steep dips. There are some migration artifacts near the true images due to multiples and cross-talk. Preprocessing the seismic data can improve the quality of the migration image.

7.6 CONCLUSIONS AND DISCUSSIONS

We developed the theory and method of a hybrid elastic one-way operator which combines the elastic thin-slab propagator in weakly heterogeneous media and reflection/transmission operators at the sharp boundaries. Two approximations are made. One is the local Born approximation for weak heterogeneities. The other is the tangent plane approximation at the sharp boundaries. Overall, it works well for strong contrast media with a smoothly curved boundary, such as salt intrusions, but may not be suitable for random heterogeneities with strong perturbations. Both the accuracy and efficiency of the dual-domain, depth-marching propagator are validated by two simple numerical examples. In terms of the computational efficiency, the hybrid propagator is at least one order of magnitude faster than full-wave FD in 2D case. When applied to 3D velocity model, it may save more computational time. The application of the propagator to seismic imaging is demonstrated on the Subsalt model and the three subsalt reflectors are shown clearly in the resulting migration image. The propagator has the flexibility to switch on/off wave modes at the sharp boundary, so that it is capable to produce multiple subsalt images by selecting different converted-paths during migration. It may offer great potential to identify the true reflection from the artifacts and further enhance the true image, especially the ones with steep dip. But this will be the target of future work.

7.7 REFERENCES

Aki, K., and P. G. Richards, 1980, Quantitative seismology: Theory and methods. W. H. Freeman and Co.

Chang, W. F., and G. A. McMechan, 1987, Elastic reverse-time migration: Geophysics, 52, 1365-1375.

Chang, W. F., and G. A. McMechan, 1994, 3D elastic prestack, reverse-time depth migration: Geophysics, 59, 597-609.

Hou, A., and K. Marfurt, 2002, Multicomponent prestack depth migration by scalar wavefield extrapolation: Geophysics, 67, 1886–1894.

Purnell, G. W., 1992, Imaging beneath a high-velocity layer using converted wave. Geophysics, 57, 1444-1452.

Sun, R., and G. A. McMechan, 1986, Pre-stack reverse-time migration for elastic waves with application to synthetic offset vertical seismic profiles: Proceedings of the IEEE, 74, no. 3, 457-465.

Voronovich, A. G., 1999. Wave scattering from rough surface: Springer-Verlag, Berlin.

Wu, R. S., 1989, Representation integrals for elastic wave propagation containing either the displacement term or the stress term alone: Phys. Rev. Letters., 62, 497-500.

Wu, R. S., 1994, Wide-angle elastic wave one-way propagator in heterogeneous media and an elastic wave complex-screen method: J. Geophys. Res., 99, 751-766.

Wu, R. S., 1996, Synthetic seismograms in heterogeneous media by one-return approximation: Pure and Applied Geophysics, 148, 155-173.

Wu, R. S. and K. Aki, 1985, Scattering characteristics of elastic waves an elastic heterogeneity: Geophysics 50, 582-595.

Wu, R. S., H. Guan, and X. Y. Wu, 2001, Imaging steep sub-salt structure using converted wave paths: SEG annual meeting, Expanded Abstracts, SEG 71st Annual Meeting, 845-848.

Wu, R. S., and X. B. Xie, 1994, Multi-screen backpropagator for fast 3D elastic prestack migration: Mathematical Methods in Geophysical Imaging II SPIE 2301, 181-193.

Wu, R. S., X. B. Xie, and X. Y. Wu, 2007, One-way and one-return approximations for fast elastic wave modeling in complex media, in Wu R. S. and V. Maupin, eds., Advances in wave propagation in heterogeneous earth: Elsevier, 266–323.

Wu, R. S., R. Yan, X. B. Xie, and D. Walraven, 2010, Elastic converted-wave path migration for subsalt imaging: SEG annual meeting, Expanded Abstracts, SEG 80th Annual Meeting, 3176-3180.

Wu, X. Y., and R. S. Wu, 2005. AVO modeling using elastic thin-slab method: Geophysics, 71, No 5, C57-67.

Xie, X. B., and R. S. Wu, 1995, A complex-screen method for modeling elastic wave reflections: SEG annual meeting, Expanded Abstracts, SEG 65th Annual Meeting, 1269-1272.

Xie, X. B., and R. S. Wu, 2001, Modeling elastic wave forward propagation and reflection using the complex-screen method: J. Acoust. Soc. Am., 109, 2629-2635.

Xie, X. B. and R. S. Wu, 2005, Multicomponent prestack depth migration using elastic screen method: Geophysics, 70, S30-S37.

Zhe, J. and S. A. Greenhalgh, 1997, Prestack multicomponent migration: Geophysics, 62, 598–613.

7.8 APPENDIX 7A: Weyl integrals of the elastic Green's tensors

The background Green's displacement tensor in the horizontal wavenumber domain is

$$\begin{aligned} G\left(\mathbf{x}_T, z; \mathbf{x}'_T, z'\right) &= G^P\left(\mathbf{x}_T, z; \mathbf{x}'_T, z'\right) + G^S\left(\mathbf{x}_T, z; \mathbf{x}'_T, z'\right) \\ &= \frac{1}{4\pi^2}\int d^2\mathbf{K}_T e^{i\mathbf{K}_T x_T}\left[G^P\left(\mathbf{K}_T, z; \mathbf{x}'_T, z'\right) + G^S\left(\mathbf{K}_T, z; \mathbf{x}'_T, z'\right)\right] \end{aligned} ,\quad (7.A1)$$

where

$$G^P\left(\mathbf{K}_T, z; \mathbf{x}'_T, z'\right) = \frac{ik_\alpha^2}{2\rho_0\omega^2}\hat{k}_\alpha\hat{k}_\alpha\frac{1}{\gamma_\alpha}e^{-i\mathbf{K}_T x'_T + i\gamma_\alpha\left(z-z'\right)}, \quad (7.A2)$$

$$G^S\left(\mathbf{K}_T, z; \mathbf{x}'_T, z'\right) = \frac{ik_\beta^2}{2\rho_0\omega^2}\left(\mathbf{I} - \hat{k}_\beta\hat{k}_\beta\right)\frac{1}{\gamma_\beta}e^{-i\mathbf{K}_T x'_T + i\gamma_\beta\left(z-z'\right)}, \quad (7.A3)$$

are wavenumber-domain Green's function for P and S waves, in which $\mathbf{I}$ is the identity matrix, and

$$\mathbf{k}_{\alpha} = \left(\mathbf{K}_T, \gamma_{\alpha}\right), \tag{7.A4}$$

$$\mathbf{k}_{\beta} = \left(\mathbf{K}_T, \gamma_{\beta}\right), \tag{7.A5}$$

are the P and S wavenumber vectors respectively, with $\mathbf{K}_T$ as the horizontal wavenumber and γ_{α} and γ_{β} as vertical wavenumbers for P and S waves, respectively, defined by

$$\gamma_{\alpha} = \sqrt{k_{\alpha}^2 - \mathbf{K}_T^2}, \tag{7.A6}$$

$$\gamma_{\beta} = \sqrt{k_{\beta}^2 - \mathbf{K}_T^2}, \tag{7.A7}$$

where $k_{\alpha} = \omega/\alpha_0$ and $k_{\beta} = \omega/\beta_0$ with α_0 and β_0 as the P and S wave background velocities in the thin-slab, respectively. The unit direction vectors of P and S plane wave propagation are

$$\hat{k}_{\alpha} = \frac{\mathbf{k}_{\alpha}}{k_{\alpha}}, \tag{7.A8}$$

$$\hat{k}_{\beta} = \frac{\mathbf{k}_{\beta}}{k_{\beta}}, \tag{7.A9}$$

where the source location is $\left(\mathbf{x}'_T, z'\right)$ and the observation location is $\left(\mathbf{x}_T, z\right)$.

Correspondingly, the Weyl integral of the Green's traction tensor can be obtained

$$\Gamma\left(\mathbf{x}_T, z; \mathbf{x}'_T, z', \hat{n}\right) = \Gamma^P\left(\mathbf{x}_T, z; \mathbf{x}'_T, z', \hat{n}\right) + \Gamma^S\left(\mathbf{x}_T, z; \mathbf{x}'_T, z', \hat{n}\right)$$
$$= \frac{1}{4\pi^2}\int d^2\mathbf{K}_T e^{i\mathbf{K}_T x_T}\left[\Gamma^P\left(\mathbf{K}_T, z; \mathbf{x}'_T, z', \hat{n}\right) + \Gamma^S\left(\mathbf{K}_T, z; \mathbf{x}'_T, z', \hat{n}\right)\right], \tag{7.A10}$$

where

$$\Gamma^P\left(\mathbf{K}_T, z; \mathbf{x}'_T, z', \hat{n}\right)$$
$$= \frac{-k_\alpha^3}{2\rho_0\omega^2}\left[\lambda\hat{k}_\alpha\hat{n} + 2\mu\left(\hat{n}\cdot\hat{k}_\alpha\right)\hat{k}_\alpha\hat{k}_\alpha\right]\frac{1}{\gamma_\alpha}e^{-i\mathbf{K}_T x'_T + i\gamma_\alpha(z-z')}, \tag{7.A11}$$

$$\Gamma^S\left(\mathbf{K}_T, z; \mathbf{x}'_T, z', \hat{n}\right)$$
$$= \frac{-k_\beta^3}{2\rho_0\omega^2}\mu\left[\left(\hat{n}\cdot\hat{k}_\beta\right)\mathbf{I} + \hat{k}_\beta\hat{n} - 2\left(\hat{n}\cdot\hat{k}_\beta\right)\hat{k}_\beta\hat{k}_\beta\right]\frac{1}{\gamma_\beta}e^{-i\mathbf{K}_T x'_T + i\gamma_\beta(z-z')}, \tag{7.A12}$$

where $\hat{n}$ is the outer normal of the surface.

7.9 FIGURES AND TABLES

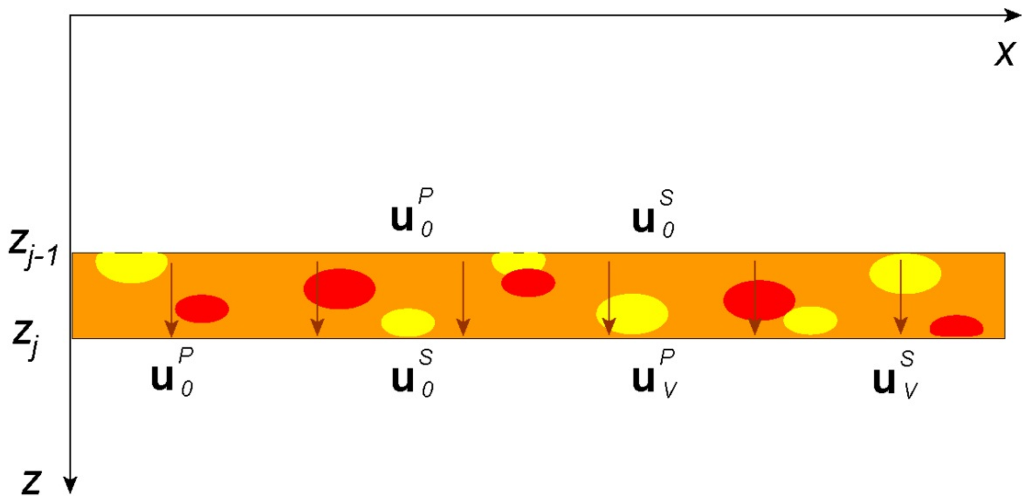

Figure 7.1 Schematic illustration of the thin-slab propagator.

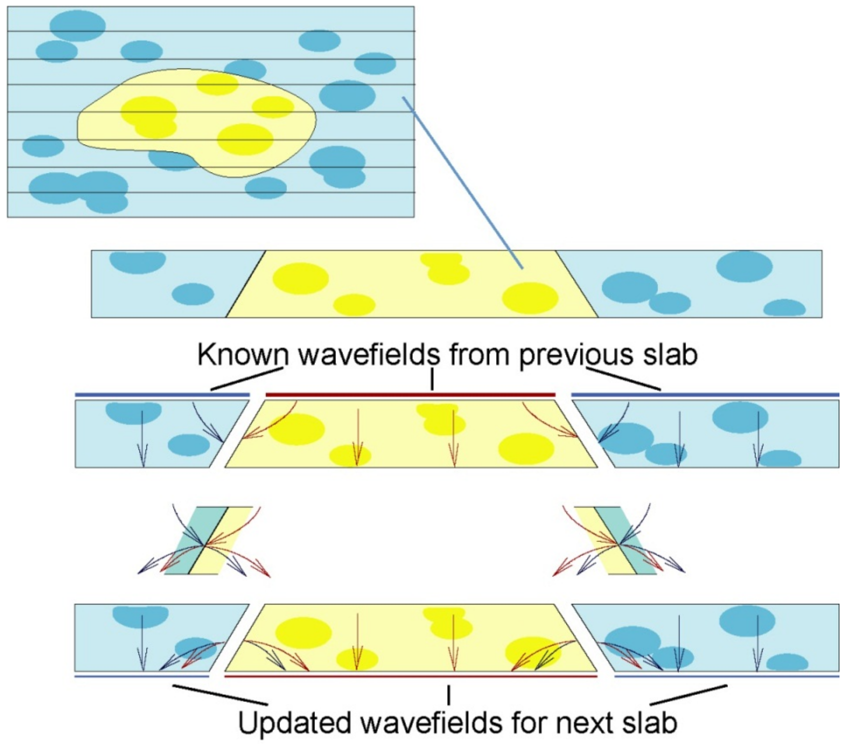

Figure 7.2 Schematic illustration of the hybrid elastic one-way propagator.

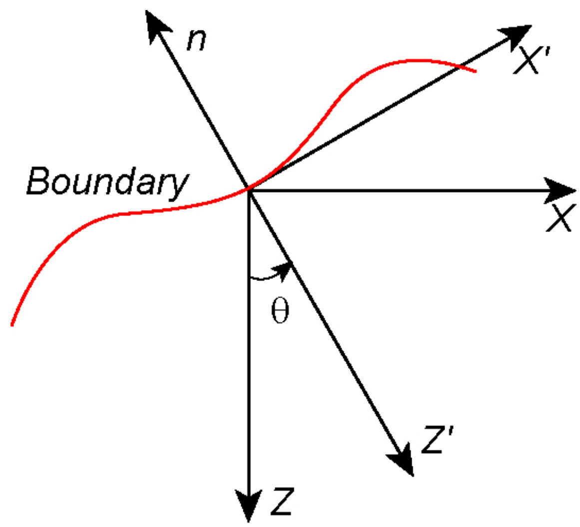

Figure 7.3 The coordinate transform from Cartesian coordinate to local boundary coordinate. $X-Z$ is the Cartesian coordinate and $X'-Z'$ is the local boundary coordinate. θ is the rotation angle from Cartesian coordinate to the local boundary coordinate. The red curve is the boundary and $\hat{n}$ is the normal vector to the boundary.

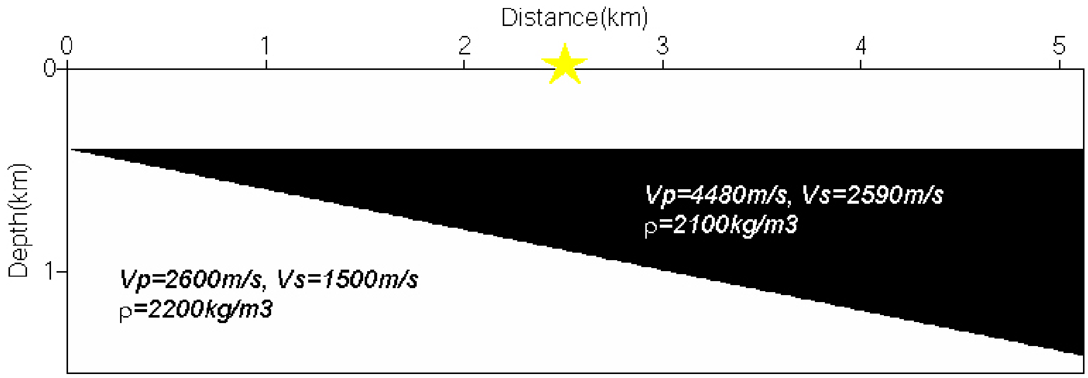

Figure 7.4 An elastic salt model. The elastic parameters and shot location are indicated in the figure.

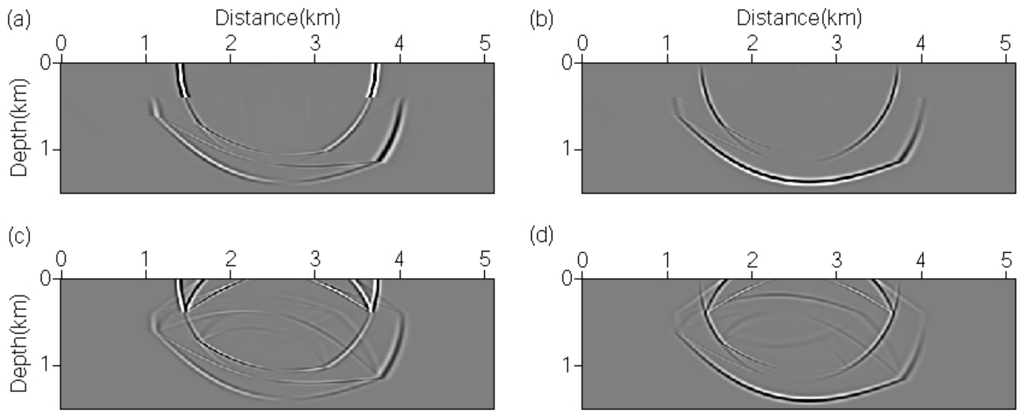

Figure 7.5 The snapshots generated in the wedge model by the hybrid elastic propagator (upper panel) and finite difference (lower panel). The horizontal components are shown on the left and the vertical components are shown on the right.

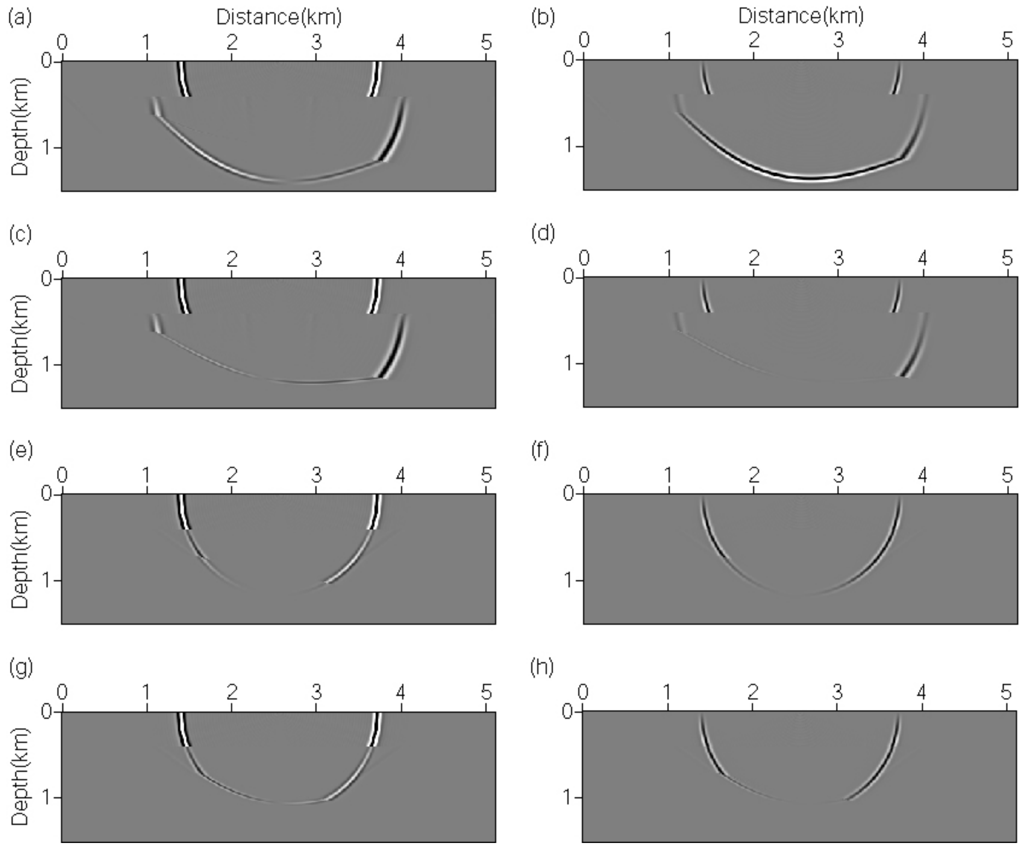

Figure 7.6 The snapshots related to different wave paths generated by hybrid elastic one-way propagator. (a) and (b) are horizontal and vertical component of wave path PPP. (c) and (d) are horizontal and vertical component of wave path PPS. (e) and (f) are horizontal and vertical component of wave path PSP. (g) and (h) are horizontal and vertical component of wave path PSS.

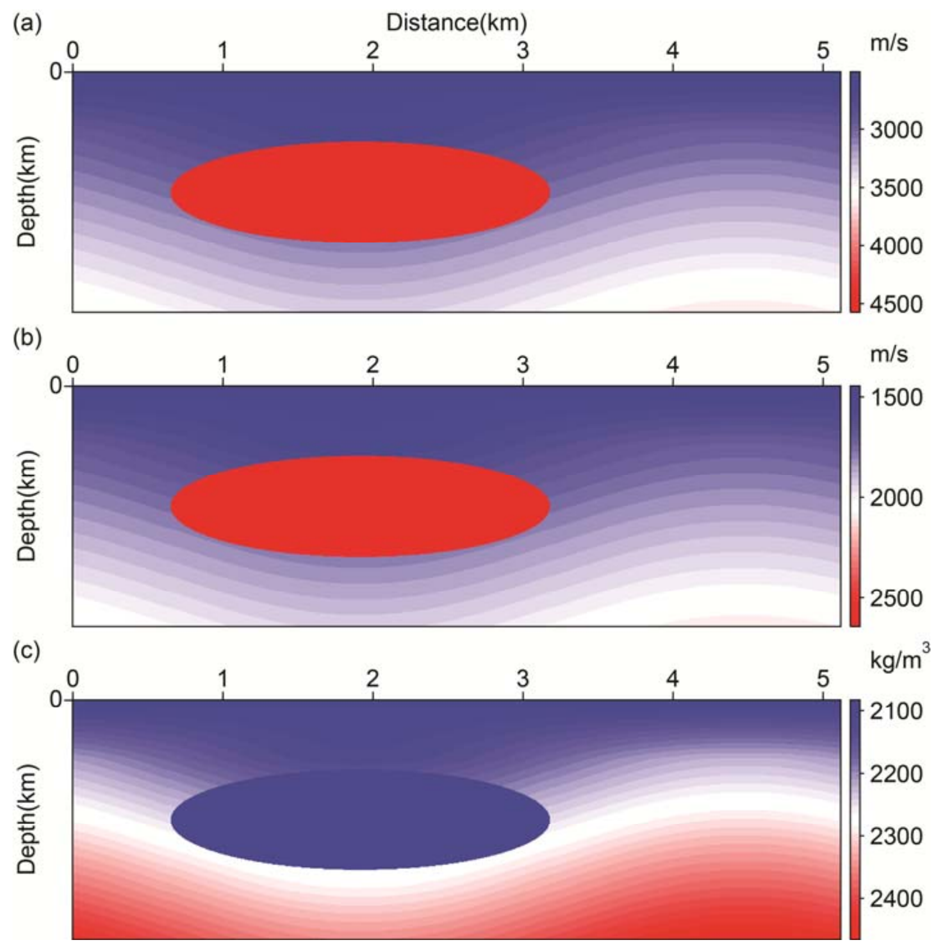

Figure 7.7 An elliptical salt model. (a) is the P-wave velocity. (b) is the S-wave velocity. (c) is the density.

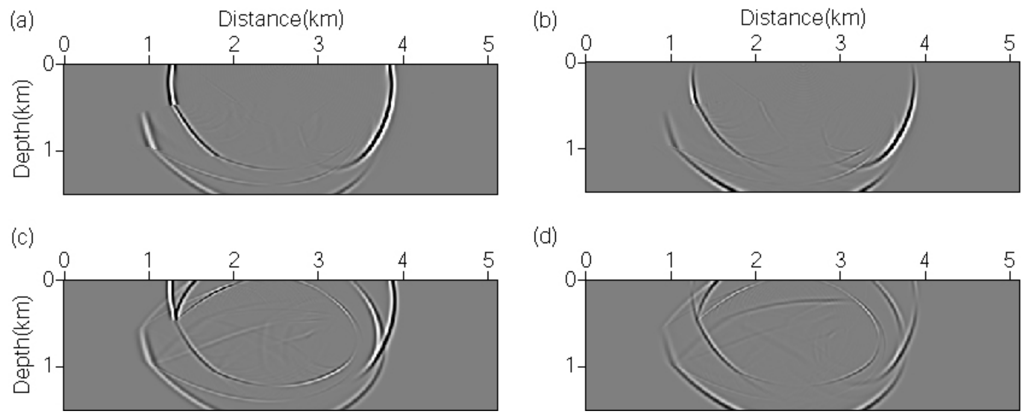

Figure 7.8 The snapshots generated in the elliptical model by hybrid elastic propagator (upper panel) and finite difference (lower panel). The horizontal components are shown on the left and the vertical components are shown on the right.

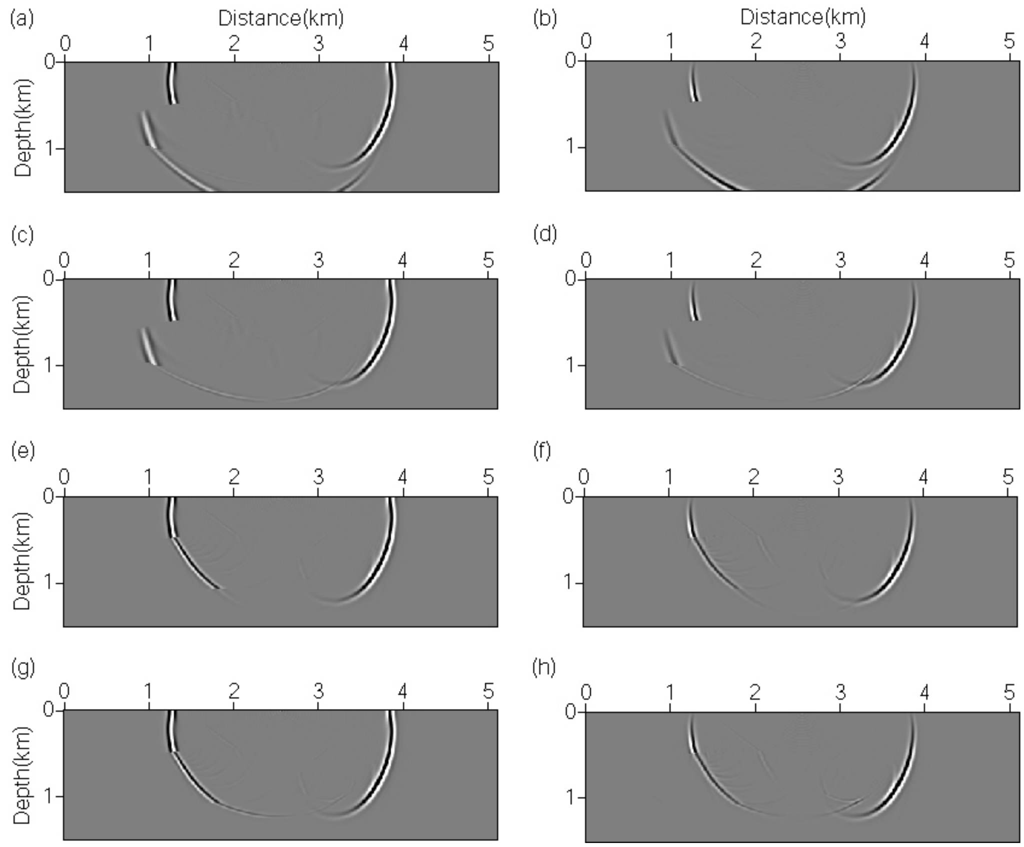

Figure 7.9 The snapshots related to different wave paths generated by hybrid elastic one-way propagator. (a) and (b) are horizontal and vertical component of wave path PPP. (c) and (d) are horizontal and vertical component of wave path PPS. (e) and (f) are horizontal and vertical component of wave path PSP. (g) and (h) are horizontal and vertical component of wave path PSS.

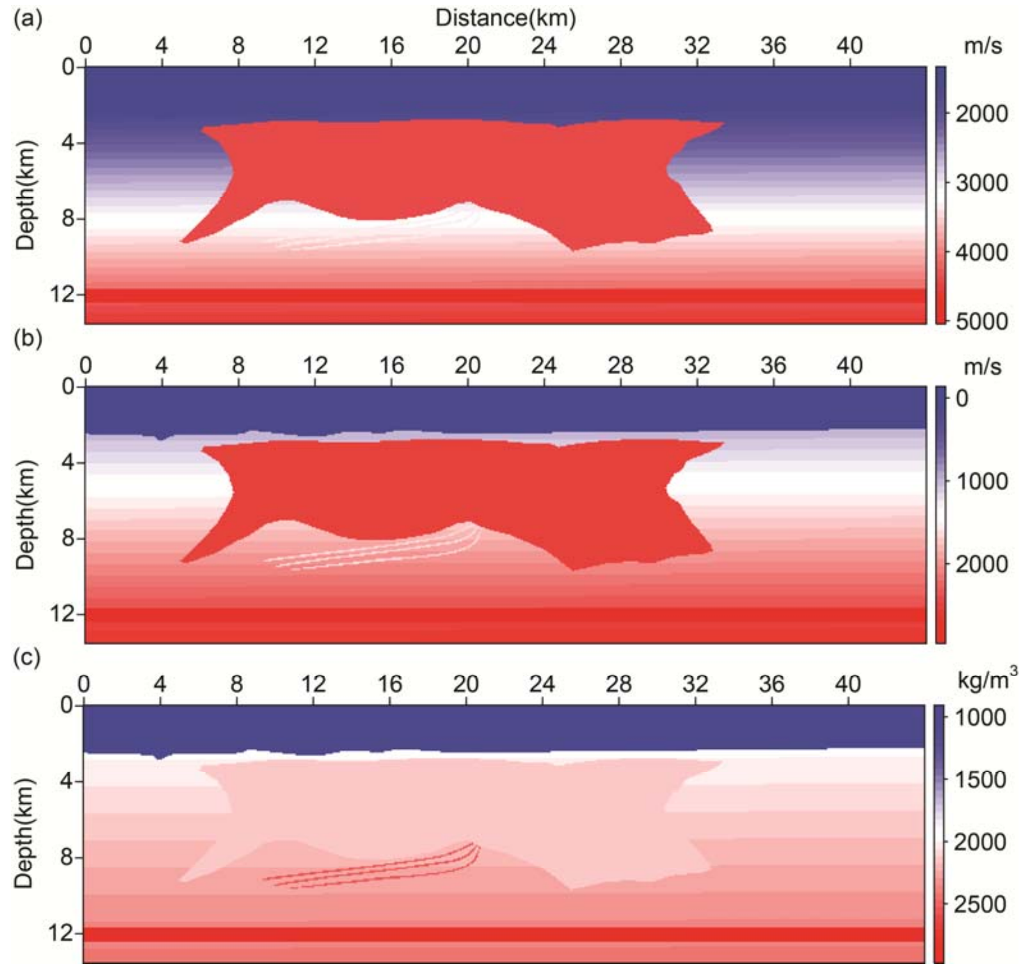

Figure 7.10 The simplified 2D Subsalt model: (a) P-wave velocity; (b) S-wave velocity and (c) density.

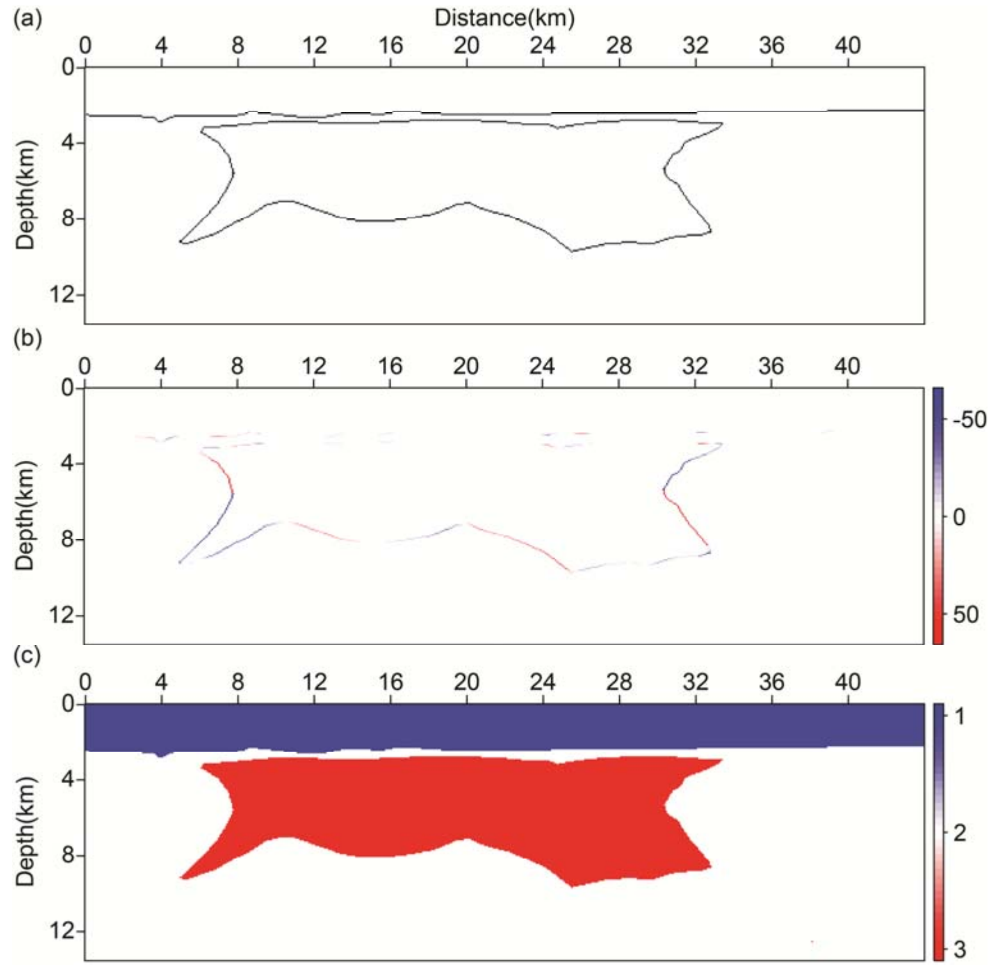

Figure 7.11 Model parameters of simplified 2D Subsalt related to hybrid one-way propagator: (a) the outline of sharp boundary; (b) the dip angle of the boundary; (c) three domains separated by the sharp boundary.

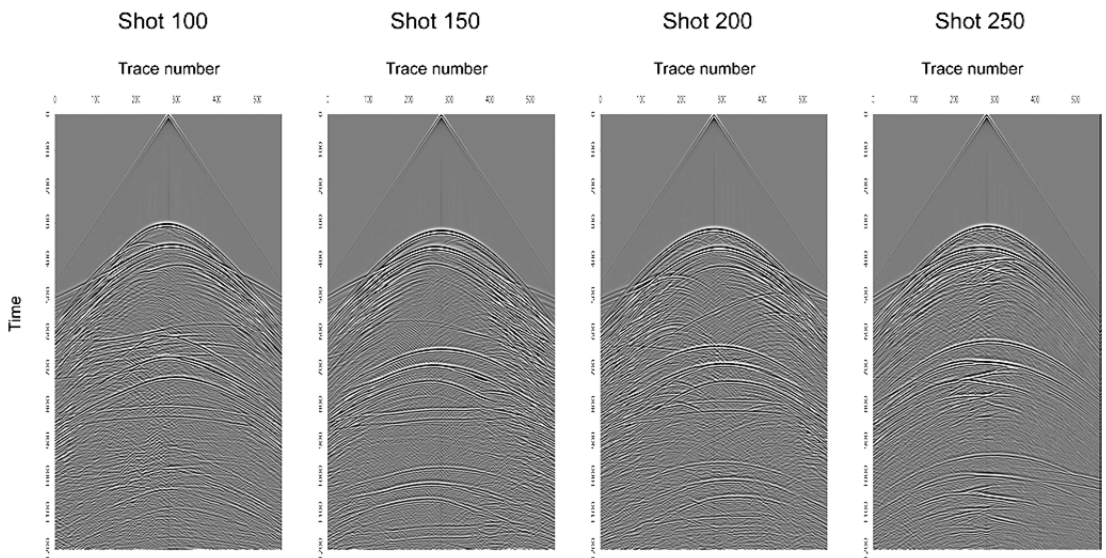

Figure 12. Synthetic records for subsalt model: Shown here are samples for shot numbers 100, 150, 200 and 250.

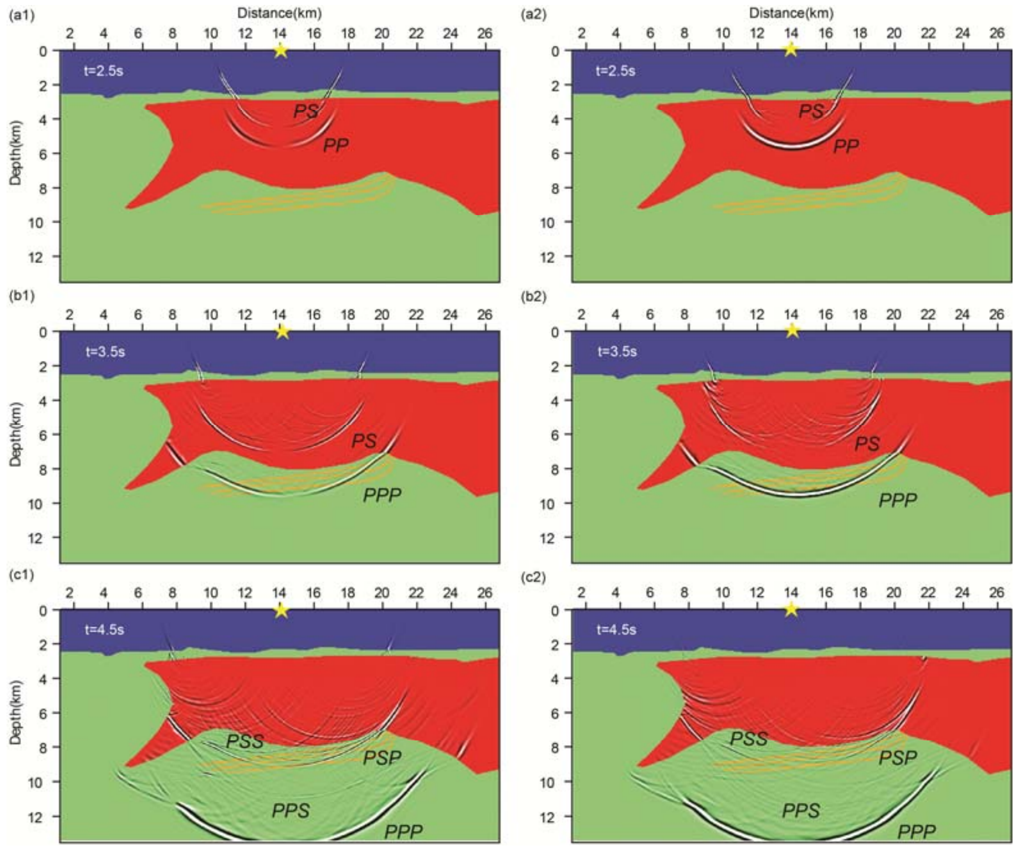

Figure 7.13 The snapshots of horizontal and vertical displacements overlapped on the Subsalt model at t=2.5s, 3.5s and 4.5s.

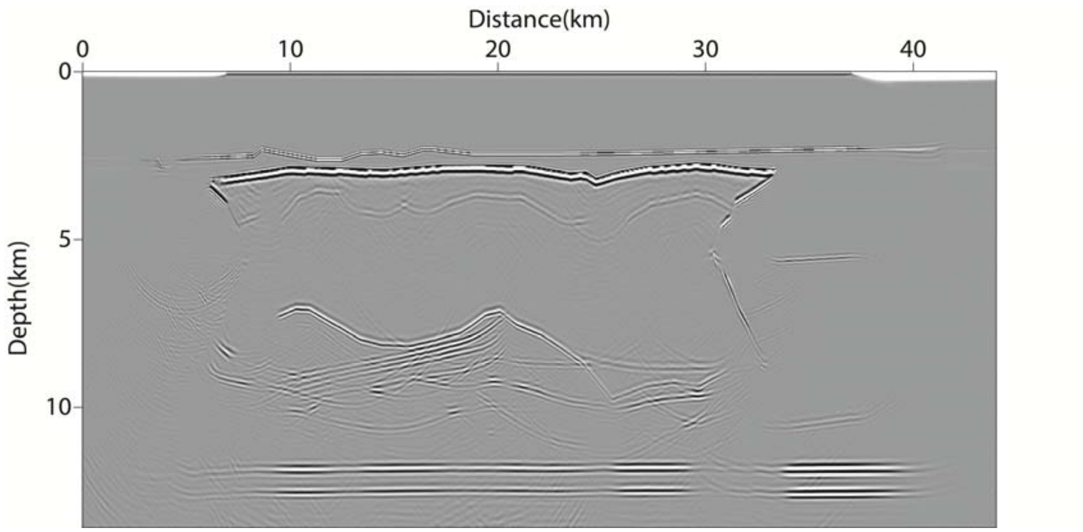

Figure 7.14 The PP image of 2D Subsalt model generated by elastic one-way propagator.

LIST OF ACRONYMS

ADCIG	Angle-domain Common Image Gather
ADR	Acquisition Dip Response
AVA	Amplitude Versus Angle
AVO	Amplitude Versus Offset
BMIG	Beam Migration
CDI	Common Dip Image
C-path	Converted-Path
FD	Finite Difference
FFT	Fast Fourier Transform
HVL	High Velocity Layer
KMIG	Kirchhoff Depth Migration
LIM	Local Image Matrix
LSM	Local Scattering Matrix
MVA	Migration Velocity Analysis
OWEM	One-way Wave-Equation Migration
PSF	Point Spreading Function
R/T	Reflection/Transmission
RTM	Reverse-Time Migration

LIST OF PUBLICATIONS

Journal paper

Rui Yan, Huimin Guan, Xiao-Bi Xie, Ru-Shan Wu, 2013, Acquisition aperture correction in angle-domain towards the true-reflection RTM, in preparation.

Rui Yan, Ru-Shan Wu, Xiao-Bi Xie, Dave Walraven, 2013, A hybrid elastic one-way propagator for strong-contrast media and its application to subsalt imaging, submitted to Geophysical prospecting.

Rui Yan and Xiao-Bi Xie, 2012, Angle-domain imaging condition for elastic RTM and its application to angle gathers extraction, Geophysics, Vol 77, No 5, S105-S115.

Conference Abstract

Rui Yan, Huimin Guan, Xiao-Bi Xie, Ru-Shan Wu, 2013, Acquisition aperture correction in angle-domain towards the true-reflection RTM, submitted to SEG Annual meeting.

Rui Yan, Ru-Shan Wu, Xiao-Bi Xie, Dave Walraven, 2013, A hybrid elastic one-way propagator for strong-contrast media and its application to subsalt imaging, submitted to SEG Annual meeting.

Rui Yan and Xiao-Bi Xie, 2012, AVA analysis based on RTM angle-domain common image gather, 82nd Annual International Meeting, SEG, Expanded Abstracts.

Rui Yan and Xiao-Bi Xie, 2011, Angle gather extraction for acoustic and elastic RTM, 81st Annual International Meeting, SEG, Expanded Abstracts, 3141-3146.

Rui Yan and Xiao-Bi Xie, 2010, A new angle-domain imaging condition for elastic RTM, 80th Annual International Meeting, SEG, Expanded Abstracts, 3181-3186.

Ru-Shan Wu, Rui Yan, Xiao-Bi Xie, and Dave Walraven, 2010, Elastic converted-wave path migration for subsalt imaging, 80th Annual International Meeting, SEG, Expanded Abstracts 29, 3176-3180.

Rui Yan and Xiao-Bi Xie, 2009, A new angle-domain imaging condition for prestack reverse-time migration, 79th Annual International Meeting, SEG, Expanded Abstracts, 2784-2788.

WTOPI annual report

Rui Yan, Huimin Guan, Xiao-Bi Xie and Ru-Shan Wu, 2013, Acquisition aperture correction in angle-domain towards the true-reflection RTM, No 24, 109-126.

Rui Yan, Ru-ShanWu, Xiao-Bi Xie, and Dave Walraven, 2013, A hybrid elastic one-way propagator for strong-constrast media and its application to subsalt imaging, No 24, 127-148.

Rui Yan, Chuck C. Mosher and Xiao-Bi Xie, 2012, AVA analysis based on RTM angle-domain common image gather, No 23, 115-134.

Rui Yan, Ru-Shan Wu, Xiao-Bi Xie, and Dave Walraven, 2012, An elastic one-way propagator and its application to migration, No 23, 169-194.

Rui Yan and Xiao-Bi Xie, 2011, Angle-gather extraction for acoustic and isotropic elastic RTM, No 21, 117-128.

Rui Yan and Xiao-Bi Xie, 2010, A new angle-domain imaging conditions for acoustic and elastic reverse time migration, No 19, 91-108.

Rui Yan and Xiao-Bi Xie, 2010, Angle domain information in reverse time migration and local AVA analysis: A preliminary investigation, No 19, 109-118.

Ru-Shan Wu, Rui Yan, Xiao-Bi Xie and David Walraven, 2010, Elastic converted-wave path migration for subsalt imaging, No 19, 119-128.

Rui Yan and Xiao-Bi Xie, 2009, A new angle-domain imaging condition for prestack reverse-time migration, No 16, 197-206.